Cavitation

CFD Analysis of Cavitation Dynamics in a Converging-Diverging Nozzle

Master Thesis by

Benoît COINTE

September 2018

Technische Universiteit Delft

Cavitation

CFD Analysis of Cavitation Dynamics in a Converging-Diverging Nozzle

by

Benoît COINTE

to obtain the degree of Master of Science
at the Delft University of Technology,

Student number:	4631552	
Project duration:	December 15, 2017 – September 1, 2018	
Thesis committee:	Prof.dr.ir. T.J.C. van Terwisga,	TU Delft, supervisor
	ir. S. Schenke,	TU Delft, daily supervisor
	Dr. ir. M. Pourquie	TU Delft
	ir. S . Jahangir	TU Delft
	ir. T . Melissaris	TU Delft
	ir. W. Hogendoorn	TU Delft

An electronic version of this thesis is available at `http://repository.tudelft.nl/`.

TU Delft

Contents

Abstract

Cavitation is the process of formation and disappearance of a vapour phase in a liquid once it is subjected to a decrease, followed by an increase, of pressure. In the maritime industry, appendices and propulsion systems of ships are subjected to large fluctuations of pressure and must hence face the appearance of such phenomena and the hindrance they cause. Indeed, cavitation erosion, caused by the collapse of vapour bubbles on the surfaces of a ship's appendices is one of the most remarkable and disastrous consequences of cavitating flows on performance and life of such devices. A particular area of interest is the mechanisms which trigger the shedding of partial cavities forming on walls, leading to the formation of bubble clusters called cavitation clouds.
A major difficulty for these investigations is the extreme complexity of cavitating flows, due to the unsteady dynamics of cavities and the large band of scales involved. A good comprehension of physics and experimental investigations are the first methods for the investigation of such phenomena. In 2017, Jahangir and al [15] experimentally investigated the cavitation dynamics in a converging-diverging nozzle for different flow conditions, determined by the inlet velocity u and static pressure p. Two types of shedding mechanisms, responsible for the formation of cloud vapour after the detachment of partial cavities of the wall, were found and investigated. The first mechanism, named re-entrant jet is a pressure driven mechanism which forms at the cavity closure region due to an adverse pressure gradient. The second one is shock wave driven and called the bubbly shock mechanism. A transition regime where both regimes coexist was also investigated.

These experiments were done in order to validate and develop numerical two phase flow models with the data obtained. Indeed, developing a robust model capable of modeling accurately typical shedding mechanisms at different cavitation numbers could be a great use for an in depth investigation of cavitation dynamics responsible of the cavitation erosion in the maritime industry. Thus, in this study, Computational Fluid Dynamics (CFD) is used extensively to develop a solver in order to reproduce the cavitation dynamics in a converging-diverging nozzle. The software package used is OpenFOAM.
First, a literature study is performed to gain insight into the mechanics of cavitation. The growth and shedding of partial cavities in a nozzle are individually discussed and the related physics are analyzed. The development of the numerical model is then discussed. The geometry of the experimental setup is reproduced on ANSYS and several meshes are created. The different possibilities to model the cavitating flow in a CFD environment are assessed, explaining the advantages and disadvantages of viscid versus inviscid flow solver, incompressible versus compressible modeling. Although a turbulent flow is expected in the experimental setup, the viscosity is considered negligible in this study and Euler model is implemented on OpenFOAM. A cavitation model is chosen and the numerical setup is introduced.

In order to validate the model which is created in this study, three test cases are implemented. The first one aims to reproduce the bubbly shock as the shedding mechanism and compare the numerical finding to the experimental finding. The second test case recreates the conditions for a re-entrant liquid jet to appear. Finally, the third test case investigates the transition regime. The comparison between numerical and experimental results are done first by studying the instantaneous flow topology before investigating the temporal evolution of the shedding process. X-t diagram is presented as the main tool to perform these analysis. This numerical study aims to reproduce these different shedding mechanisms for similar flow conditions. The geometry of the experimental setup is reproduced on Ansys and several meshes are constructed. A two phase flow model is implemented in the open source software OpenFOAM, using an inviscid model. Different test cases are performed and the different regimes are investigated and compared with the experimental findings. The first test case simulates the bubbly shock mechanism, which is the less known shedding process. Then, a test case for the re-entrant jet mechanism and one for the transition regime are performed.

Based on these three test cases, the evolution of the Strouhal number, characteristic of the shedding frequency as a function of the cavitation number, is investigated and used to verify and validate the solver. It is concluded that an inviscid, incompressible model is a suitable approach to describe cavitation dynamics in a venturi nozzle. All different shedding mechanisms are reproduced when implementing the same flow conditions of the experiments. However, the numerical results still lack precision, especially considering the re-entrant jet shedding frequency, which is lower in the numerical investigations. The implementation of the solver shows that an overestimation of the pressure loss in the venturi is the main reason for the difference observed in this study, leading to larger cavity length and lower shedding frequency. The general recommendation for future work is to find the source of this pressure overestimation, and further investigate the different mechanisms with the same solver in order to further develop and improve the numerical model to make the solver more efficient and stable, thus viable for all simulations at different flow conditions.

Benoît COINTE
Delft, September 2018

Preface

Comme ceux qui ne comprennent pas la nature des choses sont incapables de rien affirmer sur elles, mais les imaginent seulement et prennent l'imagination pour l'entendement, ils croient donc fermement qu'il y a de l'ordre dans les choses, ignorants qu'ils sont et de la nature des choses et de la leur propre. Lorsque les choses sont disposées de façon que la représentation par les sens nous permette de les imaginer facilement, nous disons qu'elles sont bien ordonnées. Dans le cas contraire nous disons qu'elles sont ou mal ordonnées ou confuses. Et comme les choses que nous pouvons imaginer facilement nous sont plus agréables que les autres, les hommes préfèrent donc l'ordre à la confusion, comme si, en dehors de l'imagination, l'ordre était quelque chose dans la nature.

– Spinoza, Ethique 1, Appendice

This master thesis report is the result of a research period in the Fluid Mechanics department and is part of the Master of Science in Marine Technology, track Science with specialisation in Ship Hydrodynamics at Delft University of Technology.
During these nine months, different cavitation regimes in a converging-diverging nozzle have been investigated through CFD computations and results have been compared to experimental findings for their validations. Readers who are especially interested in our results may refer to chapters 5 6 and 7 and those more interested in the bubbly shock mechanism may refer only to chapter 5.

This thesis has been a great opportunity to expand my knowledge in Computational Fluid Dynamics. I worked with great pleasure and could still go on for 9 additional months! I would like to express my thanks to Dr. Tom Van Terswiga and Sören Schenke for this master thesis position, the knowledge, the help and supervision they provided during that time. The topic was extremely dense and exciting. I must say I had quite the inspiration when I went to the fluid mechanics department looking for a master thesis.

I would also like to thank the whole committee, Matthieu, Saad, Themis, Tom, Sören and William, for their supervision and all the help provided. I learned a lot on different topics from each one of you, which made this research work complete and very interesting. A special word of thanks is dedicated to my friends at University, my roommates Eddy, Enrico, Ipek and Marcela which made the last 9 months go in the blink of an eye and my parents who have always been here and supported me in many ways.

Benoît COINTE
Delft, September 2018

List of Figures

List of Tables

Nomenclature

Roman

f	frequency of oscillation for a sheet cavity	$[m^2 \cdot s^{-2}]$
K	Pressure loss	$[-]$
k	Turbulence kinetic energy	$[m^2 \cdot s^{-2}]$
p	Local mixture pressure	$[kg \cdot m^{-1} \cdot s^{-2}]$
p_{max}	Maximum pressure	$[kg \cdot m^{-1} \cdot s^{-2}]$
p_{ref}	Reference pressure	$[kg \cdot m^{-1} \cdot s^{-2}]$
p_v	Vapor pressure	$[kg \cdot m^{-1} \cdot s^{-2}]$
p_0	Initial pressure at undisturbed condition	$[kg \cdot m^{-1} \cdot s^{-2}]$
p_{inlet}	Pressure value at the inlet of the Venturi	$[kg \cdot m^{-1} \cdot s^{-2}]$
p_{outlet}	Pressure value at the outlet of the Venturi	$[kg \cdot m^{-1} \cdot s^{-2}]$
Δp	Pressure difference	$[kg \cdot m^{-1} \cdot s^{-2}]$
Q	Flow rate	$[m^3 \cdot s^{-1}]$
R, R_b	Bubble radius	$[m]$
Re	Reynolds number	[-]
St_d	Strouhal number	[-]
t	Time	$[s]$
Δt	Time step size	$[s]$
T	Temperature	$[K]$
u	Velocity	$[m \cdot s^{-1}]$
u_0	Velocity reference	$[m \cdot s^{-1}]$

Greek

σ	Cavitation number	$[-]$
ρ	Mixture density	$[kg \cdot m^{-3}]$
ρ_l	Liquid density	$[kg \cdot m^{-3}]$
ρ_v	Vapor density	$[kg \cdot m^{-3}]$
ω	Specific dissipation rate of turbulent kinetic energy	$[s^{-1}]$
α	Void fraction	$[-]$
γ	Liquid fraction	$[-]$
μ	Dynamic viscosity	$[kg \cdot m^{-1} \cdot s^{-1}]$

μ	Kinematic viscosity of the mixture	$[m^2 \cdot s^{-1}]$

Abbreviations

CFD	Computational Fluid Dynamics
DNS	Direct Numerical Simulation
FVM	Finite Volume Method
LES	Large Eddy Simulation
PSD	Power Spectral Density
$RANS$	Reynolds Averaged Navier Stokes Equation
TST	Transient Scanning Technique

1 Introduction

The phenomenon of cavitation is not a recent discovery, as it was first observed by L. Euler in 1754 while developing water turbines. The word " cavitation" was then first introduced by R.E Froude and mentioned in 1895 by Barnaby and Thornycroft, who investigated the sea-trial failure of a British High speed warship HMS daring, due to the formation of vapour bubbles on the propeller blades. Nowadays, it can be observed in various engineering systems, ranging from hydraulic machinery to turbo-pumps for space applications. Cavitation may be the origin of several negative effects such as noise, vibrations, performance alterations, erosion or structural damage.
Hydrodynamic cavitation can be described by the presence of vapour filled regions in a liquid flow due to the pressure in the region being close to the vapour pressure. Crossing the liquid / vapour curve present in Figure 1.1 represents a reversible transformation under static, or equilibrium conditions, conditions. Cavitation thus appears similar to boiling, except the driving mechanism is not the increase of temperature, but a decrease in pressure.

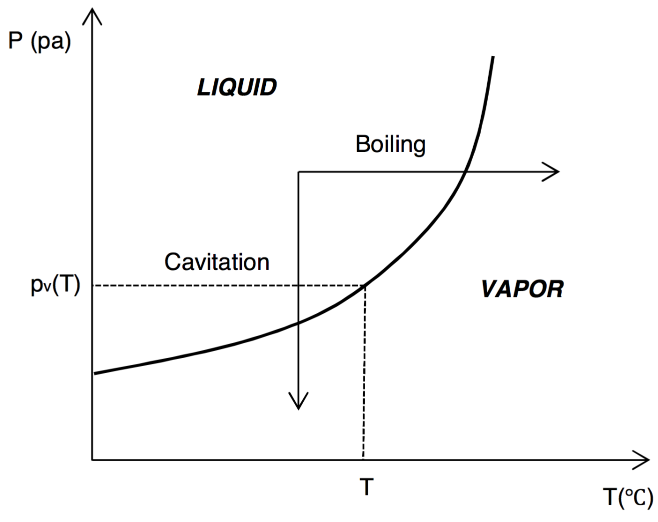

Figure 1.1: Phase diagram describing how cavitation occurs in a system by lowering pressure [21].

Investigating this phenomenon could be of great use for the prevention of the negative effects cited above. However, the physical experimentations can be very limited, in terms of geometric possibilities but also due to time and cost constraints. This is why the interest for numerical models, is growing. Indeed, CFD can be of great use for the studying of these cavitation effects. With the growth of computational power and the development of more sophisticated cavitation model, numerical tools have become a great asset for researchers. New models can be implemented and validated using experimental investigations, which represents a important potential gain of cost and time. Numerical cavitation models were successfully implemented over the years [40], mostly based on RANS and sometimes LES solvers.

Having a robust and reliable model capable of reproducing cavitation dynamics observed in experiments is thus of a great interest for companies.

1.1. Background

The development of cavitation in the liquid flow can take different patterns, depending on the profile shape, water quality, cavitation number, etc... Initially, it will strongly be dependent of the non-cavitating flow structure. According to their physical appearance , several typical types of cavitation have been classified :

- **Traveling bubbles cavitation**. Isolated bubbles are observed and are carried along by the main flow, as shown in Figure 6.12a. They are initiated from the weak points in the water, also named cavitation nuclei. Generally, these nuclei are microscopic devices filled of gas which are contained in the liquid. They collapse on downstream pressure recovery section.
- **Vortex cavitation**. Such cavitation develops at the vortex core with lower pressure than the vapour pressure. It is thus frequently observed at the tip of the hub of propellers. An example of this type of cavitation is shown in Figure 6.12b.
- **Attached cavities / sheet cavitation**. Cavitation appears as a form of cavity which is attached to the suction side of the foil. Partial cavitation is when the cavity only covers a part of the geometry whereas supercavitation fully covers the geometry. Partial cavitation is observed in Figure 6.12c.
- **Cloud cavitation**. Cloud cavitation is usually observed when an unsteady partial sheet cavity is shed due to different mechanisms that develops in some region of the flow. This kind of cavitation is defined by the appearance of a cloud of many small bubbles or vortices, as shown in Figure1.2d.

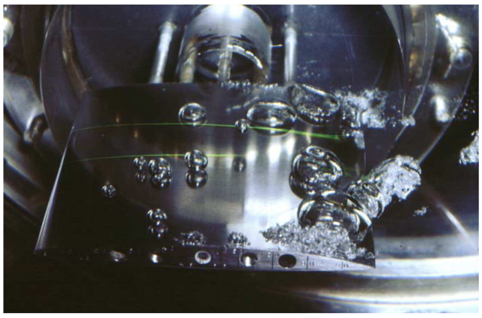

(a) Example of traveling bubble cavitation. Experience by Franc and Michel [10].

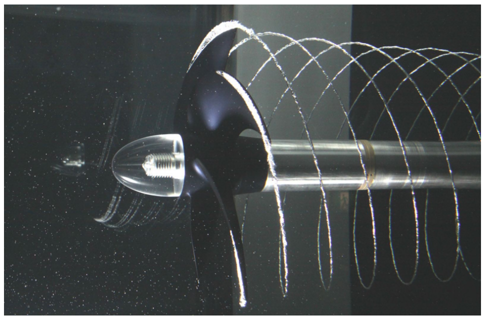

(b) Tip vortex cavitation. Credit Cavitation Research Laboratory/AMC.

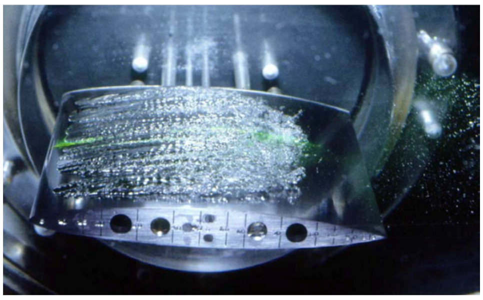

(c) Example of sheet cavitation.Experience by Franc and Michel [10].

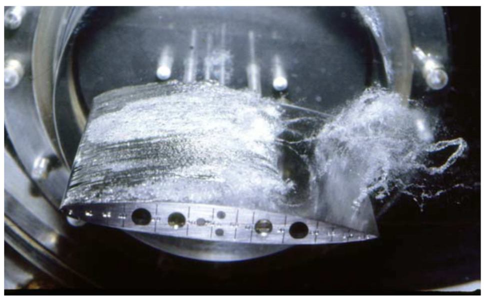

(d) Combined presence of sheet and cloud cavitation. Experience by Franc and Michel [10].

Figure 1.2: Typical visualisation of different cavitation types.

The present study will only concern partial cavities, forming in a venturi nozzle.This geometry type and the behavior of cavitation developing in it has been extensively investigated over the past 60 years because of the wide range of phenomena associated with their flow. Indeed, it appears that due to low static pressure regions situated at the throat, partial cavities are formed and develop along the nozzle. Moreover, it was observed that the stability of these partial cavities are closely related to the flow conditions. However, with a change in flow conditions, these stable cavities can experience auto-oscillation of cavity length, resulting in the shedding of the vapour clouds. This phenomenon is called cloud cavitation and carries away the vapor filled mixture which was responsible for the forming of the cavities. Cloud cavitation is one of the main responsible for cavitation erosion and cavitation noise, because it is carried along by the main flow downstream to region with higher pressure, causing a sudden condensation and collapse of the structures. Thus, investigating the dynamics of partial cavities is a primary concern to avoid such destructive effects.

Reproducing recent reference experiments performed by TU Delft researchers Jahangir and al [15] by numerical simulation, the different flow regimes will be characterised by their large scale cloud cavitation. Indeed, by modifying certain physical parameters inherent to the flow, such as global static pressure and flow velocity in the flow loop, different shedding mechanisms are observed. The first one is the re-entrant jet mechanism, which consists in the presence of a stagnation point at cavity closure resulting in a reversed liquid flow propagating upstream into the cavity term as the re-entrant liquid flow. This phenomenon is driven by the kinematics at cavity closure. Numerous studies such as [16] [22] [6] have found the presence of a re-entrant liquid flow to be the dominant mechanism responsible for this transition.
The second shedding mechanism is known as the bubbly shock effect and follows recent discovery of the presence of propagating void-fraction discontinuity or bubbly shock waves in certain flow that resulted in cavity pinch-off and its shedding [13]. On the contrary of the re-entrant jet mechanism which is a kinematic driven phenomenon, the bubbly shock is a shock wave driven phenomenon. To appear, more extreme condition must be applied to the flow (higher velocities, lower pressure).
Following these hypothesis, Jahangir and al [15] performed several experimentations in TU Delft faculty where cavitation dynamics were investigated in a venturi nozzle. From their results, it appears that two distinct cavitation mechanisms can be identified as a function of several parameters. A third regime was identified, called the transition regime where the flow is both driven by the re-entrant jet mechanism and bubbly shock flow.

1.2. Objective

The aim of this graduation project is to successfully implement a robust and validated numerical method for the prediction of the cavitation dynamics in a converging-diverging nozzle. Reproducing recent reference experiments performed by TU Delft researchers Jahangir and al [15], this model will have to match the experimental results obtained earlier. Thus, this work aims to reproduce the three different cavitation regimes identified during the experiments : Bubbly shock effect, re-entrant jet mechanism and transition regime. The main objective will be to match the shedding frequency, depending on the intensity of cavitation which triggers different shedding mechanisms. This study is consecutive of a global desire to increase the knowledge of the different cavitation dynamics and the different triggering mechanisms of their shedding.

The goal of this research can be summarised in the main research question :

Is it possible to to reproduce with a sufficient precision the main cavitation dynamics present in a venturi nozzle with a mass transfer model for our CFD computations. More precisely, is it possible to reproduce the characteristics of a compressible bubbly shock shedding mechanism with an incompressible solver ?

To answer this question, the following goals have been set and incorporated in the thesis :

- Literature review of the different shedding mechanisms, their cause of appearance and their different dynamics.
- Development of an inviscid and incompressible solver.
- Perform different simulations at different cavitation numbers to observe and identify the three different shedding regimes.

The model used for numerical simulation will be a two-phase flow model and will be implemented in the open source code OpenFOAM. The geometry and the meshing will be processed by the CAD software ICEM. The inviscid simulations will try to reproduce the pattern of the chart obtained in the previous experimental investigation. For all of them, a grid and time step sensitivity study will be performed. One simulation will take place at the Bubbly shock region, another at the re-entrant jet region. However, more simulation will be performed at the transition regime where both mechanisms co-exist. This will allow a more in-depth study of this region.

1.3. Plan of approach

First, a literature study is performed to gain insight into the mechanics of cavitation. The fundamentals of cavitation will be introduced [11] [9] and non-dimensional numbers allowing a more precise description of cavitation effects will be searched [15]. Then, an important part of the bibliographic review will be focusing on the dynamics of shedding mechanisms such as the re-entrant jet mechanism [37] or the bubbly shock propagation as a mechanism of shedding in separated cavitating flow [13] [12]. Additional papers about possible correlation between viscosity, turbulence and cavitation will also be looked upon [24]. The second part of this research process will focus on numerical simulation and computation fluid dynamics. Studies will be performed first on OpenFoam software [27], which uses finite volume method. Different cavitation model and their implementation on OpenFOAM will be reviewed [40]. Then, research will take place concerning the possible choices between RANS and LES methods [18] [28] [42] [1]. Other topics to be reviewed will concern the boundary conditions that needs to be implemented at the outlet and inlet of the geometry. Different possibilities seem to emerge and the best option has to be chosen.

Once the literature study is done, the geometry of the venturi used in the experimental investigation can be created numerically. The literature review performed earlier will determine which boundary conditions need to be implemented, since fully developed flow must be present at the entry of the converging nozzle while at the outlet, the flow velocity must be equal to zero and the pressure constant. Once the geometry is finished, the meshing process can start. The first meshes will contained around one million cell and first simple test case will be performed to verify and iterate the boundary conditions. The values of the experimental investigations will be selected so the previous investigation can serve as a benchmark. The boundary layer will not be refined due to cost constraints, notwithstanding the fact that turbulence in the wall plays a minor if not null role in the development of the shedding mechanism.

Then, the first simulations can take place. The cavitation dynamics study will be done for three simulation cases :

Case 1 : Bubbly shock mechanism

The bubbly shock mechanism is a shock driven phenomena, resulting from the condensation and collapse of the cavitation cloud. This means that our solver, based on an incompressible model, will probably have difficulties to reproduce a compressible shocks. Moreover, high gradients will also be present at the throat of the Venturi, making this test the most complex of this study. This simulation will take place at low cavitation number.

Case 2 : Re-entrant jet mechanism

The re-entrant jet is a common phenomenon which was extensively studied along the last years. Thus, this mechanism will be of a lesser importance compared to the bubbly shock mechanism; That is why it will be the second case to be treated. The same studies and process than the bubbly shock case will be applied.

Case 3 : Transition regime

Transition regime is both driven by the bubbly shock and re entrant jet mechanism. Thus both results of re entrant jet and bubbly shock will have to be compiled first in order to make a good study of this phenomenon.

1.4. Report structure

The outline of the report is as follows : While this chapter clarified the introduction and problem description, chapter 2 will introduce the basis of cavitation dynamics which are taking place in a venturi nozzle. The different relevant fluid parameters to describe accurately the cavitation dynamics for this study will also be presented which will as well a relevant fluid parameters which will be used to describe the cavitation dynamics. Finally, a presentation of the different experiments realised in the facilities of TU Delft will be introduced, as well as their main results.
Chapter 3 discusses in detail the different mathematical models which will be used for our CFD model of the cavitation dynamics. An analysis between different models such as RANS and inviscid model will be made, and different cavitation models will be introduced and explained.
Chapter 4 will present the computational setup, based on the experimental setup [15], made for the study of the different cavitation regime. The meshing process will be introduced and the implementation on OpenFOAM software will be discussed.
Then the next chapters will present the main results of the CFD computations performed during this study. Chapter 5 will introduce the bubbly shock mechanism, chapter 6 the re-entrant jet regime and chapter 7 the transition regime.
Chapter 8 will present the conclusions of this study based on the results of the three test cases. Future prospects will also be discussed.

2

Cavitation dynamics : Literature review and theoretical background

This chapter contains the theoretical background regarding cavitation phenomena, especially cavitation dynamics present in a venturi nozzle. In the first case, the geometry of the venturi nozzle and the development of partial cavities are introduced. The dynamics of cavitation sheets, which ranges from the development of sheet cavities to the shedding of cloud vapour inside a venturi is then discussed. Finally, the experiments performed previously by Hogendoorn [15] are described, as well as their results, which will serve as a benchmark for our results.

2.1. Cavitation dynamics in a venturi nozzle

2.1.1. Venturi nozzle

Hydrodynamic cavitation appears due to the flowing liquid, as a result of a decrease of pressure. It describes the process of vaporisation, bubble generation and bubble collapse, and can simply be generated by the passage of the liquid through a constriction such as a throttling valve, an orifice plate, etc. Here, numerical investigations will be performed on a venturi nozzle. It is one of the simplest devices for the observation of hydrodynamics cavitation and yet it enables to study cavitation in its full complexity : cavitation inception, sheet cavitation, transition from sheet to cloud cavitation, pressure pulses and shock waves induced by cavitation collapse.
The geometry is presented in Figure 2.1 :

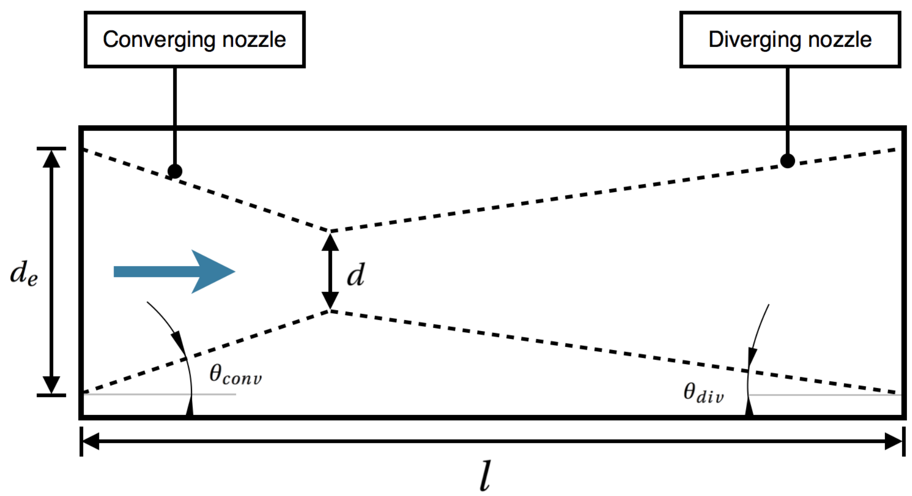

Figure 2.1: Schematic overview of a venturi with a flow velocity from the left to the right with its different parameters.

A venturi nozzle is composed of two parts. First, the flow enters a converging nozzle where the cross sectional area decreases until it reaches the throat of the venturi.
Due to the continuity equation $\nabla \cdot \mathbf{U} = 0$ with $\mathbf{U}$ the velocity vector, the progressive decrease of the cross sectional area will induce a sharp local velocity increase. This results in a large pressure drop within a globally steady flow, explained by the Bernoulli equation which states that for an inviscid, incompressible, irrotational and steady flow :

$$p + \rho U^2 = cste \tag{2.1}$$

The flow then enters the second part of the venturi which is the diverging nozzle. Here, the cross sectional area gradually increases, and velocity progressively decreases. The decrease of pressure due to the acceleration of the flow at the throat of venturi, and the nuclei present in the flow trigger the mechanism of cavitation. To describe the geometry of the venturi, several parameters must be introduced : The diameter of the throat d and of the extremities of the venturi d_e, the convergence and divergence angle, respectively $2\theta_{conv}$ and $2\theta_{div}$ and finally the total length of the Venturi l.

2.2. Cavitational shedding mechanisms dynamics

Once the cavity length is rather large, a cyclic behavior is observed in which the break-off of large cavity structures is seen. In this study, two different shedding mechanisms are introduced and are explained on the following section.But before investigating them, it is important to have analytical tools which can describe precisely the characteristics of the cavitation taking place. This is the aim of non dimensional numbers.

2.2.1. Relevant non-dimensional numbers

It appears that for different flow conditions depending on parameters such as pressure, flow velocity or the density, shedding mechanisms exhibit different mechanisms. In order to assess and quantify the most important parameters of the cavitation dynamics occurring in the venturi, non dimensional numbers must be introduced.

- **Cavitation number** σ.

  The first and most important parameters of cavitating flows is the cavitation number σ. This number is introduced to describe the intensity of the cavitation which is taking place in the flow and is described as :

  $$\sigma = \frac{p_{ref} - p_{sat}(T_{ref})}{\frac{1}{2}\rho_{liq}(p_{ref}, T_{ref}) u_{ref}^2} \tag{2.2}$$

  The cavitation number depends of reference conditions of the flow field. Different location of the reference values can be taken, depending on the application considered and the corresponding experimental data present. Considering the converging-diverging geometry nozzle, and the research of Hogendoorm [15], the global static pressure p of the system at the downstream side of the venturi is chosen. This implies that the cavitation intensity is increasing for decreasing the cavitation number. The start of cavitation phenomenon is called " cavitation inception" and defined by a critical cavitation number σ_i. One would expect that cavitation appear when the pressure drops to vapour pressure p_{sat}. In reality, deviations from this value are pretty common, as the real cavitation inception depends on different parameters such as fluid quality or initial gas content. On the other hand, " developed cavitation" will refer to a continuous situation of the steady or unsteady cavity, having significant effect on the flow dynamics.

- **Strouhal number S_t.**

  The Strouhal number S_t is also an important dimensionless parameter used to describe the different cavitation regime. In this study, it relates the oscillating frequency to the reference velocity and the reference flow dimension and thus will be used to describe the periodic cloud cavitation shedding and the repeatability of this process. This number is defined by the following equation :

$$S_{t_{d_t}} = \frac{f d_t}{u_0} \tag{2.3}$$

  Where f is the shedding frequency of the partial cavities observed in the Venturi for different cavitation regimes, based on the cavitation number. l is a reference length and u_{ref} a reference velocity. In this study, the reference length chosen is the venturi throat diameter.
  This number will be used to describe the periodic cloud cavitation shedding for a unsteady cavitating flow, based on the Venturi throat diameter d_t, u_0 the free stream velocity of the flow in the venturi throat. f[Hz] will be related to the shedding frequency of the cavitation cloud. Other definitions of the Strouhal number exists where the diameter d_t is for example replaced by the length of the cavity l. However, the definition presented in Equation 2.6 is based on the work of Hogendoorn [15] who uses it for the post processing of his results.

- **Liquid fraction Fraction γ**

  The liquid fraction γ is defined as :

$$\gamma = \frac{V_{liquid}}{V_{ref}} \tag{2.4}$$

  This parameter represents the liquid fraction contained in a reference volume V_{ref}. Once integrated over the whole domain, the total amount of liquid volume in the total volume of the flow domain can be found.
  The liquid fraction is related to the void fraction α by $\alpha = 1 - \gamma$.

- **Reynolds number Re**

  The Reynolds number Re defines the ratio of the inertial forces to the viscous forces and can be written as :

$$Re_{l_{ref}} = \frac{\rho u_0 l_{ref}}{\nu} \tag{2.5}$$

  In cavitating nozzle flows, the reference length is usually taken as the nozzle diameter. As the equation suggests, the Reynolds number increases with decreasing viscosity and it will be used for the selection of our CFD modeling.

- **Pressure loss**

  As explained earlier, a pressure loss Δp over the venturi is encountered due to wall friction loss. In reality, due to wall friction losses, a pressure loss Δp must also be added to the equations. This can be described by the pressure loss coefficient K given by :

$$K = \frac{\Delta p}{\frac{1}{2}\rho u_0^2} \tag{2.6}$$

Now that the important parameters relative to the cavitation dynamics have been introduced, the different shedding mechanisms are presented.

2.2.2. Re-entrant jet mechanism

Re-Entrant jet is the is the most classical shedding mechanism and has been extensively studied over the years. Its principle has been first described by Knapp, Daily and Hammitt (1970), giving an accurate description of the flow at the downstream end of the cavity. Due to a pressure gradient, closure region shown on figure 2.2 occurs due to the re-attachment of the external flow to the wall. Originally, the flow was moving above the cavity but it recirculates around the stagnation point. A liquid jet appears and moves upstream until it pinches off some parts of the cavity, detaching it from the wall.

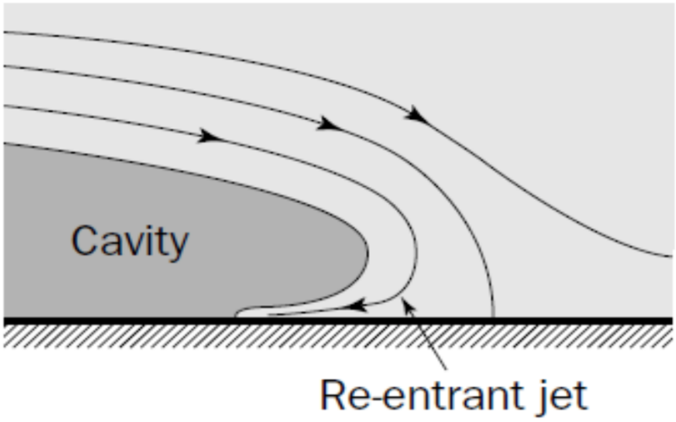

Figure 2.2: Schematic representation of the re-entrant jet flow in the closure region of an attached cavity, picture taken from Franc and Michel [5].

Two parameters are important for the re-entrant jet : the cavity thickness, with respect to the re-entrant jet thickness and the adverse pressure gradient. The adverse pressure gradient must be sufficiently strong to accelerate the flow against the downstream flow.
Re-Entrant jet is then a pressure driven phenomenon, and generally appear for soft flow conditions, at high cavitation number, synonymous of quite high pressure, low velocity.

2.2.3. Bubbly shock mechanism

Cloud cavitation can result in numerous large fluctuations of cavity volume, which causes important variations, for example in lift and drag forces. The pressure loads are also extremely high in this regime. That is why cloud cavitation is one of the phenomenon associated to the most agressive form of cavitation, with severe levels of noise and structural vibrations. Analytical studies of the dynamics of cavitation clouds can be found first to the work of van Wijngaarden [39] who attempted to model the behavior of a collapsing layer of bubbly fluid next to a solid wall. Another subject of collapsing clouds was introduced by Morch, Kedrinskii and Hanson [25] [26] and speculated that the collapse of a cloud of bubbles will involve the formation and propagation of a shock wave.

This bubbly shock mechanism is mentioned and studied experimentally in the PhD work of Ganesh in 2015 [12]. Using resolved X-ray densitometry in order to visualize the void fraction in the flow field, a propagating discontinuity is found. It is defined as shock wave driven phenomenon, as opposed to the re entrant jet mechanism which is defined as a pressure driven phenomenon.
Figure 2.3 depicts the physical phenomenon which is taking place at the Venturi for low cavitation number. As it was explained previously, the partial cavity situated in the diverging nozzle has an increased length due to the flow condition. Cavitation is also of higher intensity compared to the re-entrant jet phenomenon, meaning the liquid fraction will be lowered and the void fraction increased inside the cavity. Thus, some bubble organised in cloud cavitation will be advected to the flow, resulting in a collapse and the apparition of a shock wave.

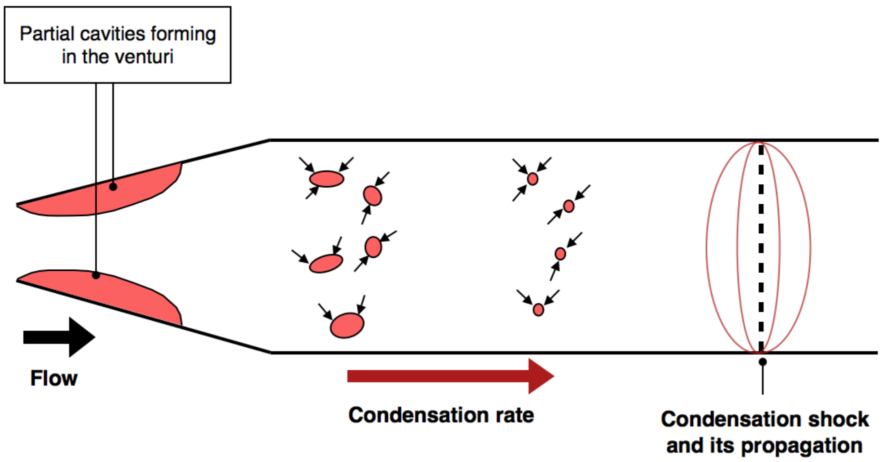

Figure 2.3: Schematic overview of the apparition of a shock wave inside a venturi at low cavitation number due to the collapse of the cloud cavitation.

The newly formed shock wave will propagate in every direction, and travel back the venturi, opposed to the flow direction. Figure 2.4 shows a schematic overview of the void fraction front which can be observed once the shock reaches the cavity. It spans the complete cavity height, moving at a certain velocity towards the wedge apex. The front reaches the apex of the wedge, causing its detachment and the shedding of a vapor cloud.
Thus, the shedding frequency can be based on the frequency of occurrence of such a shock wave.
It is important to note that the condensation shocks are distinguished from the shock waves which are emitted due to the collapse of cavity structures such as bubble or clouds. While the pressure rise of collapse-induced shocks is of short duration and high amplitude, condensation shocks associated to the retraction of a partial cavity act on longer time scales and involve phase changes.

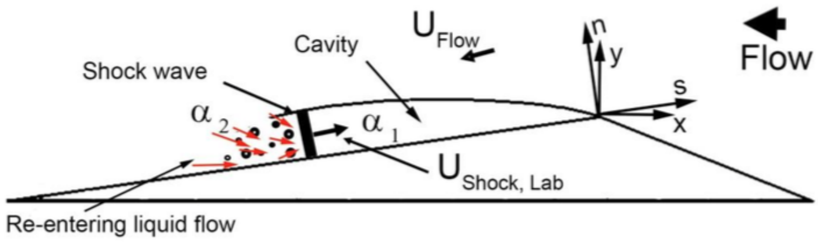

Figure 2.4: Shedding cycle in the presence of an obstacle, bubbly shock effect [12].

2.3. Experimental investigation of cavitation regime

The two shedding mechanisms were investigated by Saad and Hogendoorn [15] experimentally inside a Venturi nozzle at TU Delft facilities. An overview of the experimental apparatus is presented in Figure 2.5.

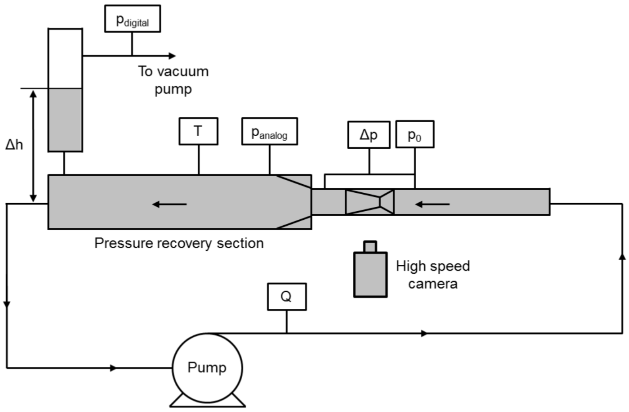

(a) Schematic overview of the experimental setup by Hogendoorn [15].

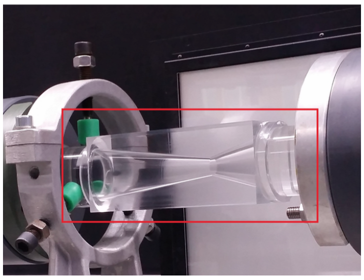

(b) Venturi Nozzle where cavitation is studied [15]

Figure 2.5: Overview of the experimental setup of Hogendoorn [15].

The setup consisted of a centrifugal pump, an axisymmetric Venturi, four pressure sensors, a temperature sensor, a flow meter, a high speed camera and a vacuum pump. Water flows in a closed loop system.

Because the flow is converged before the throat, an almost smooth velocity profile can be assumed at the Venturi throat, which implies the influence of the boundary layer on flow separation is almost negligible. It is important to note that the Reynolds number plays a role in the behavior of the flow in the Venturi : flow separation will be enhanced for increasing Reynolds number.

Measurements were performed according to a fixed protocol :

- Ambient pressure is determined for the determination of the inlet pressure p_0.
- A uniform water temperature is obtained by operating the setup a few minutes before the measurement series, in order to mix the water in the system.
- The global static pressure of the system is set to a fixed and prescribed value.
- For a fixed, prescribed global static pressure, measurements are performed at different flow velocities. This is done once the flow velocity and global static pressure are stabilized.

The method used to capture the dynamics of cavity is called shadowgraphy. The measurement target is placed in between the light source and the highspeed camera. The target is illuminated by the light source from the back side in the direction of the camera sensor. Flow rate is measured with a flowmeter.
The sensor values are saved by means of a LabView program and the highspeed camera is triggered at the same time at which the sensor values are saved. For different flow conditions, several regimes were investigated. The results are presented in the following section and will serve of reference for the CFD results presented in Chapter 5, 6 and 7.

2.3.1. Re-entrant jet mechanism

The video frames of a re-entrant jet development can be observed in figure 2.6. The cavitation number σ was set to $\sigma = 1.00$.

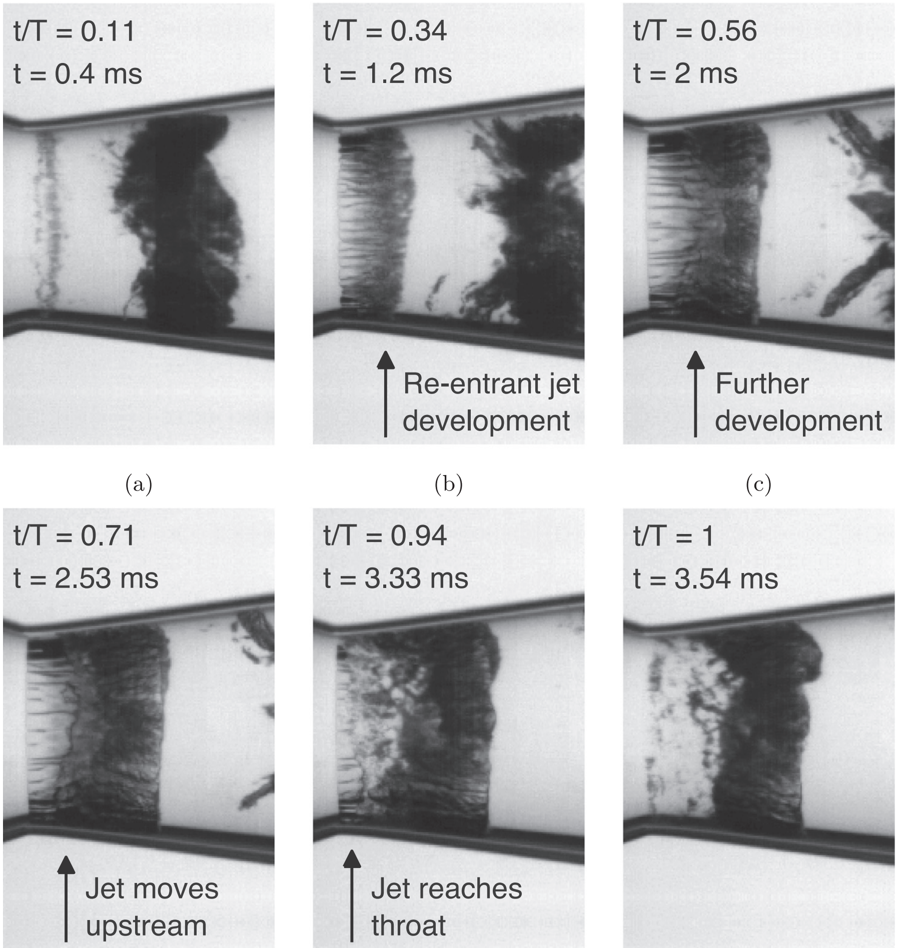

(d) (e) (f)

Figure 2.6: Video frames of re-entrant jet development obtained experimentally by Hogendoorn [15].

The jet front can be observed in figure d as it can be recognized by the chaotic interface. Then, the propagation of the jet front towards the Venturi throat is depicted from d to h. In the end, the detachment of the cavity caused by the re-entrant jet can be observed in i.
The re-entrant jet mechanism is observed for high cavitation number and exhibits a high shedding frequency coupled with a small cavity length.

2.3.2. Bubbly shock mechanism

For lower cavitation number, another mechanism than the re-entrant jet appears. Indeed, a bubbly shock mechanism, as shown in figure 5.4 can be observed. In this case, σ was set to $\sigma = 0.40(u_0 = 13.7m/s, p = 40kPa)$:

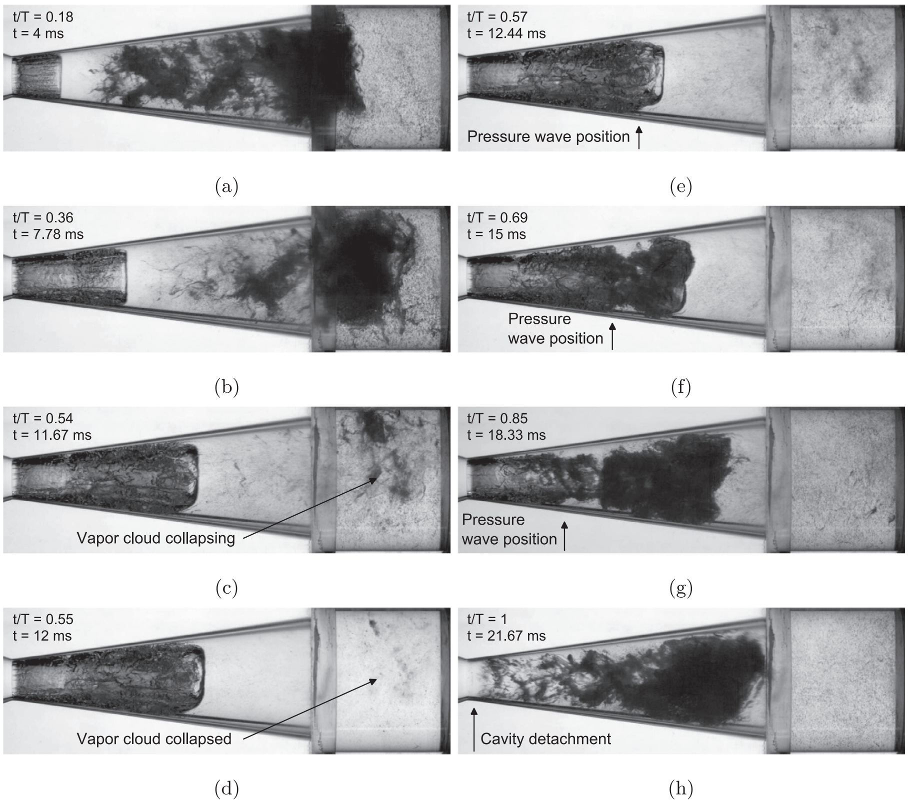

Figure 2.7: Video frames of bubbly shock development obtained experimentally by Hogendoorn [15].

The complete collapse of the cavity is observed in Figure 5.4 c and 5.4 d. This collapse causes a pressure wave, emitted in both direction. The left running pressure wave is underlined by the arrow in 5.4 e -m. It goes against the flow until it reaches the Venturi throat. Then the cavity detaches as follows from Figure 5.4.

2.4. Results and conclusion

Both re-entrant jet and bubbly shock mechanisms were observed during the experimentations. They appear for different flow conditions. While the shedding process is dominated by re-entrant jet mechanism at high cavitation number, a low cavitation number is necessary to investigate the bubbly shock mechanism.

Figure 2.8 was constructed in order to visualise the different domains of the shedding mechanisms.

Several experiments were performed at different cavitation number, and the shedding frequency was obtained for every cases and transformed into Strouhal number. As explained earlier, the Strouhal number is considered to be a dimensionless frequency, but also as a timescale of the cavity shedding process. Indeed, the inverse of the shedding frequency gives the integral time scale, corresponding to the process of cavity development to the time detachment.

Based in Figure 2.8, three different trends can be observed. First, two different cavitation mechanisms can be identified as function of the cavitation number. For $\sigma > 0.95$ cloud cavitation shedding is governed by the re-entrant jet mechanism, whereas for $\sigma < 0.8$ cloud cavitation shedding is governed by the bubbly shock mechanism. Then, inbetween these two regions, a transition regime appears, where both mechanisms co exist and can be observed.

The following hypothesis are formulated, based on the experimental work of Hogendoorn [15] and Ganesh [12] :

- Two different mechanisms can be identified as function of the cavitation sigma and are resumed.
- The results obtained by Hogendoorn [15] and displayed on figure 2.8 show that for $\sigma > 0.95$ cloud cavitation shedding is governed by the re-entrant jet. For $\sigma < 0.8$, cloud cavitation shedding is governed by the bubbly shock mechanism. Both mechanisms pre-exist in the inbetween cavitation region.

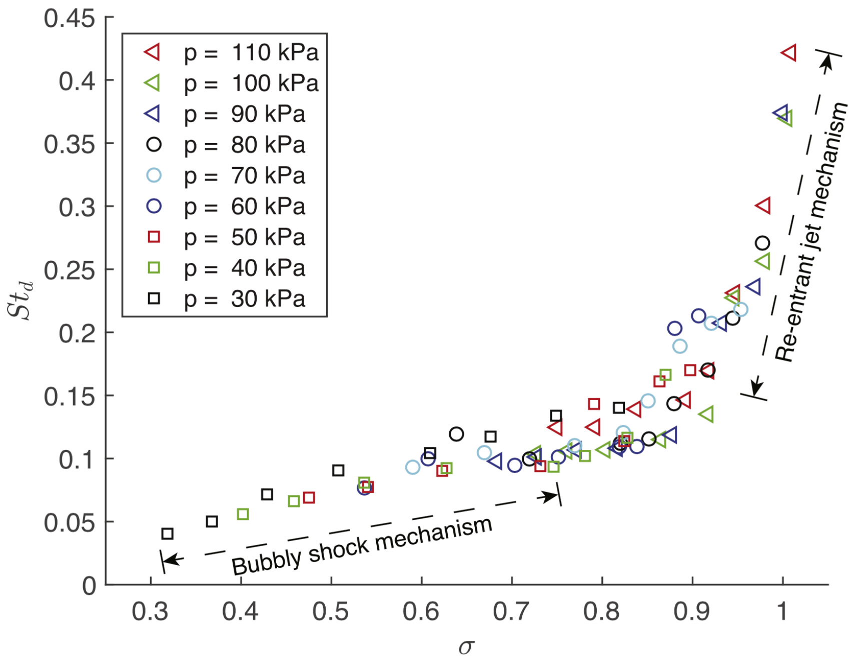

Figure 2.8: Conclusion of the experiments performed by William Hogendoorn [15].Dimensionless frequency of the cavitation shedding cycle as a function of the cavitation number.

3

Modeling cavitation with CFD : Numerical approach

First we guess it. Then we compute the consequences of the guess to see what would be implied if the law we guess is right. Then we compare the result of the computation to nature, with experiment or experience, compare it directly with observation, to see if it works. If it disagrees with experiment it is wrong. In that simple statement is the key to science. It does not make any difference how beautiful your guess is. It does not make any difference how smart you are, who made the guess, or what your name is - if it disagrees with the experiment it is wrong. That is all there is to it.

– Richard Feynman

A cavitating flow is a complex multiphase flow. It involves multiple effects such as phase change, compressibility, viscosity or turbulent fluctuations. Building a computational method to study all these effects as accurately as possible can become very challenging. Indeed, a wide range of length and time scales are affected by the complex mechanisms present in the Venturi which govern the unsteady cavitation dynamics such as the re-entrant jet and the cavitation dynamics.
In this chapter, the modelling of cavitation with CFD is introduced. First an overview of the equations which need to be solved are presented.

3.1. Governing equations

The framework of the modeling is the standard homogeneous model which provides the simplest technique for analyzing two-phase flows. The liquid/vapor mixture is treated as a pseudofluid which obeys the usual equations of single-phase flow :

3.1.1. Mass continuity equation

The first equation which needs to be resolved in order to model the cavitation dynamics in the Venturi nozzle is the mass continuity equation. It is derived from the physical principle of mass conservation; stating that, i an arbitrary material volume V, the rate of change of mass is equal to the flow which goes through the boundary of volume V. This can be written, in its local form as :

$$\frac{\partial \rho}{\partial t} + \frac{\partial \rho u_i}{\partial x_i} = 0, \tag{3.1}$$

u_i being the velocity vector, x_i the spatial vector, and ρ the density of the fluid.

3.1.2. Momentum equation

The momentum equation is derived from Newton's second law, which states that the rate of change of momentum is equal to the sum of the forces on the fluid element.

$$\frac{\partial \rho u_i}{\partial t} + \frac{\partial \rho u_i u_j}{\partial x_j} = -\frac{\partial p}{\partial x_i} + \frac{\partial}{\partial x_j}(\mu \frac{\partial u_i}{\partial x_j}), \tag{3.2}$$

- $\frac{\partial \rho u_i}{\partial t}$ is the local acceleration of the fluid .
- $\frac{\partial \rho u_i u_j}{\partial x_j}$ is the convective acceleration of the fluid .
- $\frac{\partial p}{\partial x_i}$ is the pressure gradient present in the flow.
- $\frac{\partial}{\partial x_j}(\mu \frac{\partial u_i}{\partial x_j})$ are the viscous forces.

μ is the dynamic viscosity and t the time at location x, y and z.

3.1.3. Boundary conditions

A constraint must be applied in the normal direction for solid interfaces. This boundary condition reflects the fact that at a solid interface no net flow normal to the surface can be present.

$$u_{n_{solid}} = u_{n_{fluid}} \tag{3.3}$$

In this case, the solid is a rigid wall, with $u_{n_{solid}} = 0$.

For the tangential velocity, three possible boundary conditions can be applied depending on the hypothesis made : The no-slip, slip and free slip condition. The no slip condition states that the tangential velocity of the fluid is equal to the tangential velocity of the solid. The slip condition, a velocity difference between the solid and the fluid is applied, whereas the free slip condition states that the tangential fluid velocity is not influenced by the presence of the solid.

$$u_{t_{solid}} = c \cdot u_{t_{fluid}} \tag{3.4}$$

3.2. Computational Fluid Dynamics

The modelisation of the Navier-Stokes equations are discussed. RANS equations and turbulence models classified in function of their efficiency for this study are presented in Appendix A.

3.2.1. Inviscid model

Viscosity can be characterized as the macroscopic effect of the momentum transport taking place in the molecular level in a fluid domain . For a given fluid, viscosity is measured with the coefficient dynamic viscosity μ or with the kinematic viscosity $\nu = \frac{\mu}{\rho}$. Its influence has been investigated by Sezal [35].

For the single bubble dynamics, viscosity plays a role only in the final stage of the collapse for a small bubble radius, which would necessitate an important spatial resolution [35]. Concerning the flow dynamics, in the applications considered, experimental and computational studies demonstrated that there is no separation of the boundary layer. Moreover, for the unsteady cavitation dynamics study, the cloud shedding process and the collapse mechanism responsible for the bubbly shock mechanism are all driven by inertia effects. Indeed, during the experimental studies [15], the Reynolds number was oscillating between 10^3 - 10^5. Therefore, viscosity can be consider as negligible.

That is why, for this study, the computations are to be performed for an inviscid solver. It is also known that most of the turbulence model underestimate the shedding process, especially for the re-entrant jet mechanism because of an overestimation of the turbulent viscosity.

Thus, in this study slip condition can the be applied and no refinement of the grid at the boundary layer will be necessary.

In conclusion, in this study **an inviscid solver is implemented because of the negligible effects of the turbulence and the important decrease in computational cost**.

3.3. Cavitation modeling

3.3.1. Basic equation

Cavitation modeling can be very complex, due to the unsteady dynamics of the cavities and the large band of scales involved. Two main categories exist to model the cavitation dynamics.

- **Interface tracking approach [7]**. This method is based on the free surface flow hypothesis. Here, the cavity region is assumed to have a constant pressure, which is equal to the vapor pressure of the existing liquid existing situated at the cavity interface. Thus, the simulations are only done for the liquid phase, the cavity shape being iterated until pressure equals the vapor pressure at the cavity.
- **The multiphase flow approach [33]**. For this method, the cavitating flow is considered as a homogenous mixture of both liquid and vapour. Two methods can be used for the modeling of the momentum transfer between the two phases : the void fraction transport equation model or the equation of state law.

In this study, the homogeneous flow models is used. The liquid and vapor phases are assumed to exist as a homogeneous two-phase mixture in a single fluid.

Thus, the mixture density ρ is composed of both vapour and liquid and can be decomposed in

$$\rho = \alpha\rho_v + (1-\alpha)\rho_l, \tag{3.5}$$

$$\rho = (1-\gamma)\rho_v + \gamma\rho_l, \tag{3.6}$$

γ being the liquid fraction and α being the void fraction, both defined in chapter 2. ρ_l the density of liquid and ρ_v the density of the vapour present in the flow.

Moreover, a liquid volume fraction transport for the mixture is introduced :

$$\frac{\partial \alpha_l}{\partial t} + \frac{\partial \alpha_l u_j}{\partial x_j} = \dot{m}^+ + \dot{m}^-, \tag{3.7}$$

With

$$\dot{m}^+ = Cf_1(\alpha)f_2(\alpha) \quad and \quad \dot{m}^- = Cf_1(\alpha)f_2(\alpha) \tag{3.8}$$

In the previous equations introduced above, is the velocity of the pseudofluid, α the void fraction ρ its density. Slip between liquid and vapor will be ignored, which means a unique velocity will be considered for the two phase mixture.
$\dot{m}^+$ and $\dot{m}^-$ are mass transfer source terms, appearing because of the growth and thus the evaporation and the collapse, thus the condensation, of the mixture phase.

3.3.2. Cavitation models

Several cavitation models which vary by the formulations of the condensation terms $\dot{m}^+$ and evaporation terms $\dot{m}^-$. They are presented in Table B.1 in the Appendix.
A modified Merke model is chosen for this study, based on the work of Schenke and Terwisga [31]. The source term is divided by mixture density ρ, such as the mass transfer contribution to density change rate $d\rho/dt$ only depends on liquid volume γ and pressure difference $p - p_v$ once the modified Merkle source term is introduced into mass continuity equation.

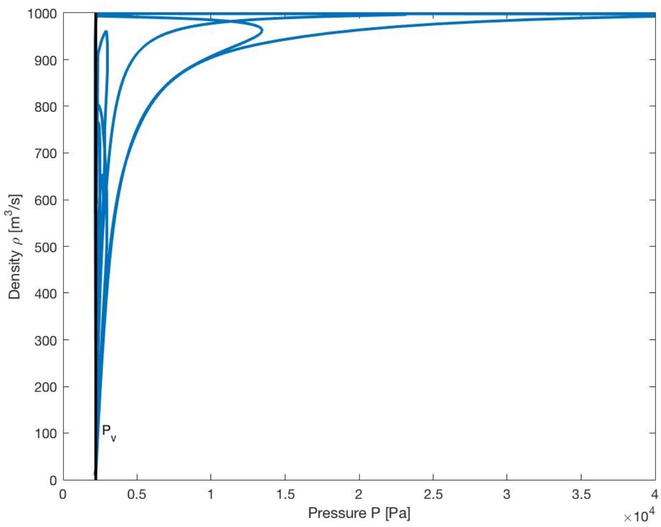

Figure 3.1: $\rho - p$ trajectory at an observation point obtained from the modified Merkle model for a time step $\Delta t = 1 \cdot 10^{-6}$. Cc = 200 kgs/m^5.

The different constants in the Merkle modified model were implemented and tested by plotting the $\rho - p$ trajectories. An example is depicted in Figure 3.1. A good transition from the liquid phase to the vapor phase is provided as the pressure decreases. Indeed, for $p < p_v$, p_v being represented by a black line, the water is in its vapor phase, meaning the density is approximately $\rho_v = 0.012 kg/m^3$, as indicated in Table 5.3. for $p > p_v$, the water should be in its liquid phase, and the transition from vapor to liquid as fast as possible. Figure 3.1 shows that the transition is fast enough. Different paths from vapor to liquid can be observed, represented by the blue lines.
The modified Merkle model exhibits a physical behaviour, with the pressure remaining close to vapor pressure in the mixture regime except for the final stage of local condensation. No significant influence of time step size on the shape of the trajectories is observed.

4

Problem description

Now that the different physical phenomenons responsible for the shedding mechanisms and their numerical modeling have been introduced, this chapter presents the numerical setup for the different study cases which are performed in this thesis. First, the experimental setup used by Hogendoorn [15] [17] is presented. This will serve as a referential for the construction of the computational domain, which is presented next. Then,the meshing process and the different grid constructed are presented. Finally, the implementation of the numerical problem in OpenFOAM is discussed.

4.1. Experimental setup

The different cavitation dynamics were captured in the experimental setup presented in Figure 4.1 and 4.2. Figure 4.1 presents an overview of the experimental geometry : flow enters a pipe section with a length of 2.0 m and diameter 50 mm. This correspond to 40 time the diameter in order to a have a fully developed turbulent flow entering the test section. Then, the flow enters a converging nozzle of 51.31 mm, with a convergence angle of 36 °. A close-up of the converging-diverging nozzle is presented in Figure 4.2. Starting height is 50 mm to finish at 16.66 mm at the contraction throat, provoking cavitation. Then, a diverging nozzle of 118.61 mm with a divergence angle of 16 ° is mounted at the beginning of the throat in order to avoid any flow separation while having a fairy rapid pressure recovery. A close up of the Venturi is shown in Figure 4.2. A downstream feeding line of 1.4 m is used where cavitation gradually disappear. A gradual transition from this tube to the pressure recovery section is introduced in order to avoid flow separation and minimize flow losses. It has a length of 0.25m and a diffuser angle of 5.7° [41]. After the transition, pressure in the flow is recovered in a pressure recovery section, with a increased diameter of 0.1 m, for an overall length of 1.92m.

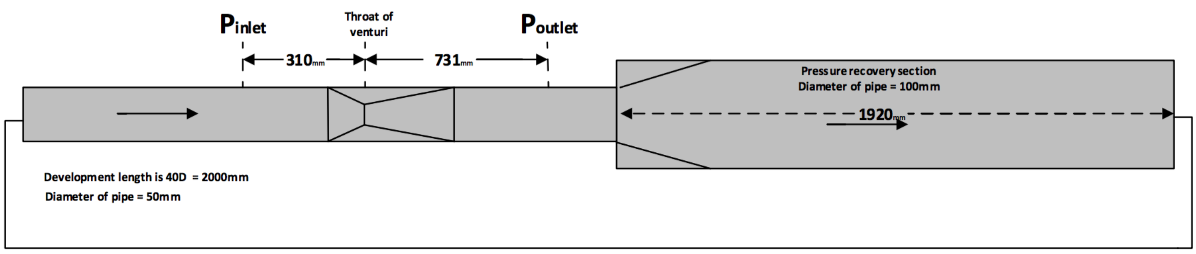

Figure 4.1: Schematic overview of the experimental geometry and relevant dimensions of the experimental setup used by Hogendoorn [15] [17]. Black arrow represents the direction of the flow.

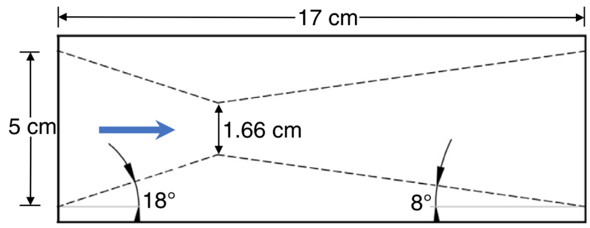

Figure 4.2: Geometry and relevant dimensions of the converging-diverging section used for the experiments of Hogendoorn [15] [17]. Blue arrow represents the direction of the flow.

4.2. Computational setup

4.2.1. Computational domain

The computation domain, depicted in Figure 4.3, reproduces the nominal experimental setup. The construction or not of the feeding line and of the downstream diffuser was discussed. Indeed, the upstream feeding line was present in the experimental setup in order to have a fully turbulent flow coming in the nozzle. Since it was decided to used an inviscid model, there is no more need for a turbulent flow. Nonetheless, it was decided to build it the same ways as the experimental setup. The amount of additional grid cells is not significant.

The geometry created on Ansys CFD is presented in Figure 4.3 and 4.4. First, a feeding line with a length of 2 m ahead of the venturi nozzle is created. The length is left inchanged compared to the experimental setup presented in Figure 4.1. As explained above, this is done in order to match as precisely as possible the experimentations.
The origin of the coordinate system coincides with the location of the throat of the Venturi nozzle at mid-span. The x-, y- and z-directions denote the streamwise, transverse and spanwise directions respectively.

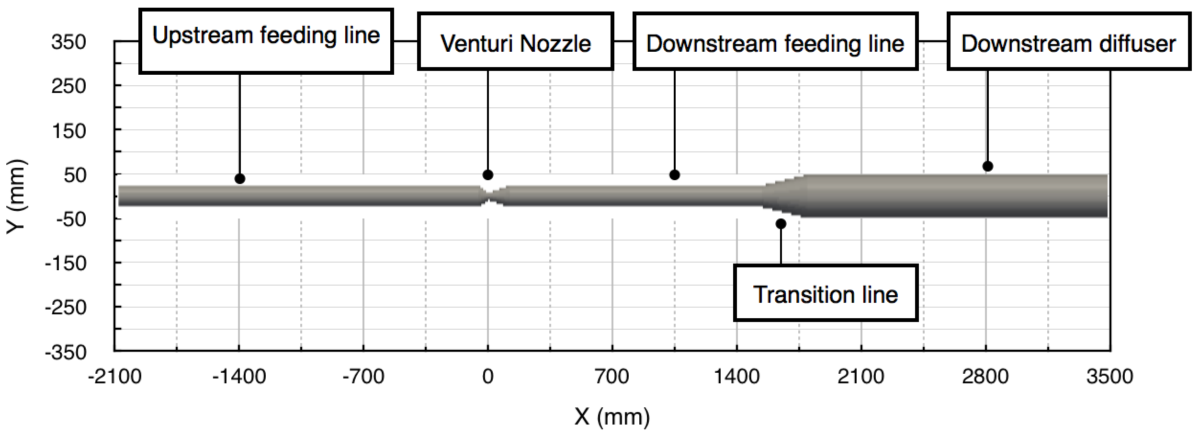

Figure 4.3: Side view (x-y plane) of the entire numerical domain, including the duct up and downstream of the test section and the large diffuser near the outlet boundary.

The venturi nozzle, presented in Figure 4.4 has the exact same proportions as the experimental setup. The converging nozzle has a length of 51.31 mm with a contraction angle of 18 °. The throat of the venturi has a diameter of 25 mm and the diverging nozzle a length of 118.61 mm, with a divergence angle of 16 °.

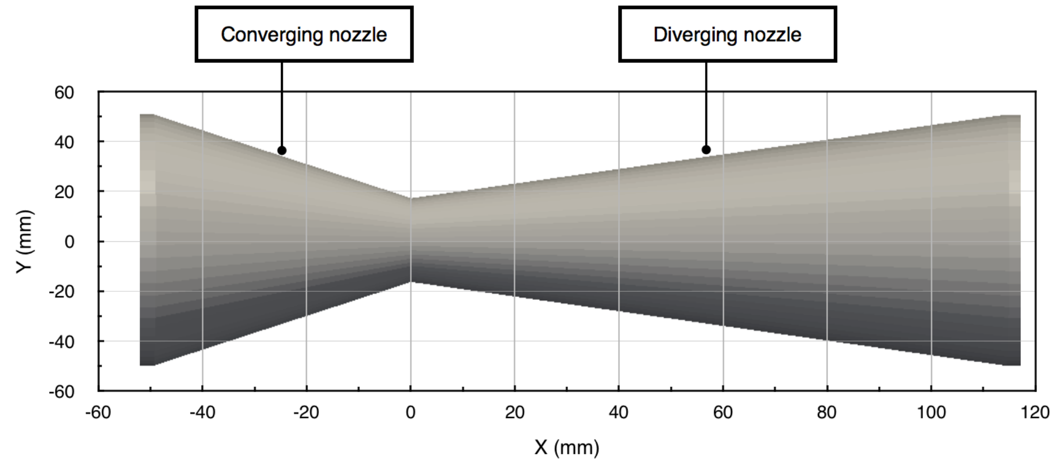

Figure 4.4: Side view (x-y plane) of the venturi, with the diverging and converging nozzle.

A downstream feeding line, presented in Figure 4.5 is added with the same measurement as the experiments. The transition line and downstream diffuser is also reproduced.

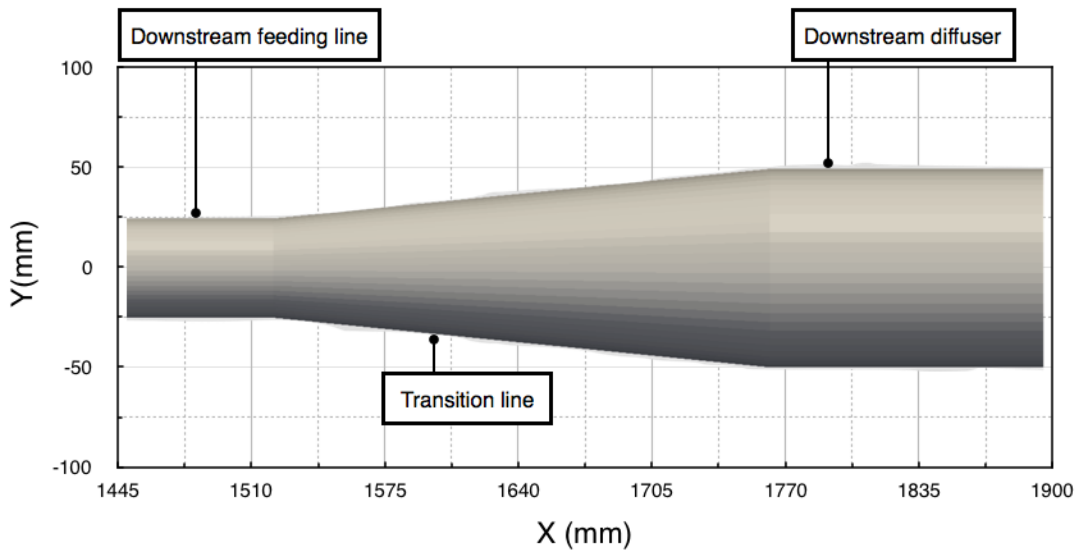

Figure 4.5: Side view (x-y plane) of the downstream feeding line, transition line and downstream diffuser.

This geometry is important to avoid any fluctuations of pressure at the outlet of the numerical setup.

4.2.2. Grid

The meshing of the geometry is done with ANSYS software.
The grid at the venturi is presented in Figure 4.6.

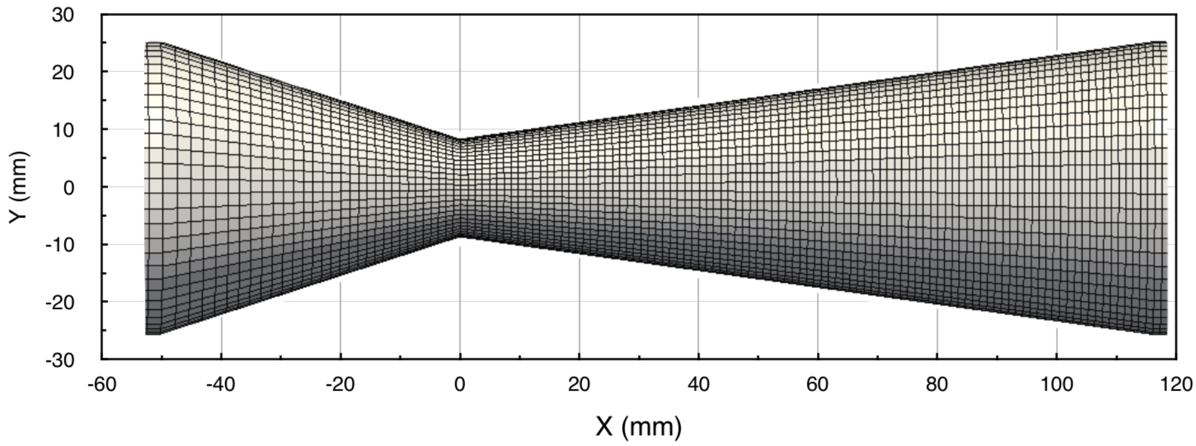

Figure 4.6: Numerical mesh of the converging-diverging nozzle, side view.

The mesh is made very fine at the diverging nozzle, where the cavitation dynamics are studied. 120 grids are constructed in it, and the length between the grids is made constant.
For the converging nozzle, a progressive refinement of the grid is performed, in order to have have a smooth transition between the upstream feeding line and the diverging nozzle. The distance between the grid at the end of the converging nozzle matches with the constant distance between the grids in the diverging nozzle.

A cross sectional view of the throat is shown in Figure 4.7. Since the geometry is only composed of pipes and nozzle, it was decided to use o-grids. There is no refinement at the wall, because the computations will be for an inviscid flow. Thus there are no need to refine in the vicinity of the boundary layer.

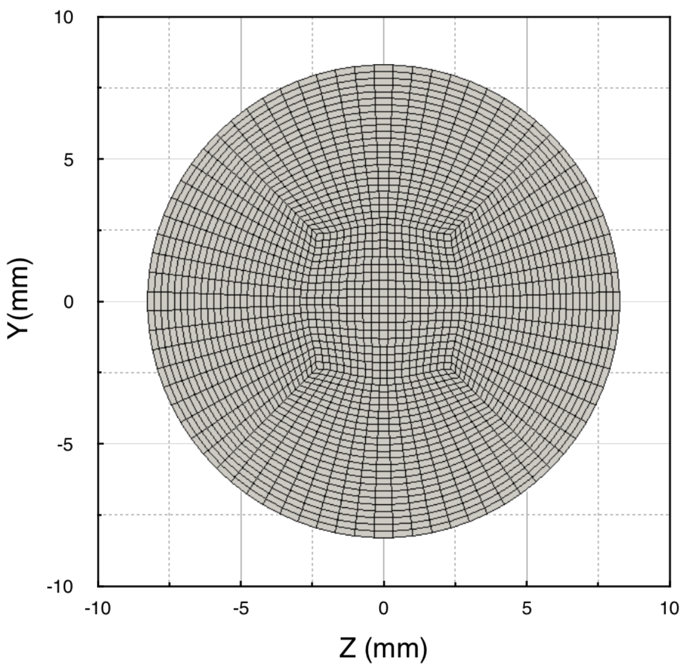

Figure 4.7: Numerical mesh of the geometry, cross sectional view of the throat.

The mesh is made very coarse in the downstream diffuser and at the beginning of the upstream feeding line. Indeed, these areas don't present any interest and are expected to have smooth flow conditions.

The progressive refinement of the upstream and downstream feeding line is shown in Figure 4.8. In order to have a transition as smooth as possible, the grid is refined all along the upstream feeding line so it matches the grid at the beginning of the converging nozzle. Concerning the downstream feeding line, some cavitational effects can appear at its beginning. Thus, the refinement is made even more precise and is longer than the downstream feeding line. The distance between the grid is kept constant for a few cm until it is progressively coarsened.

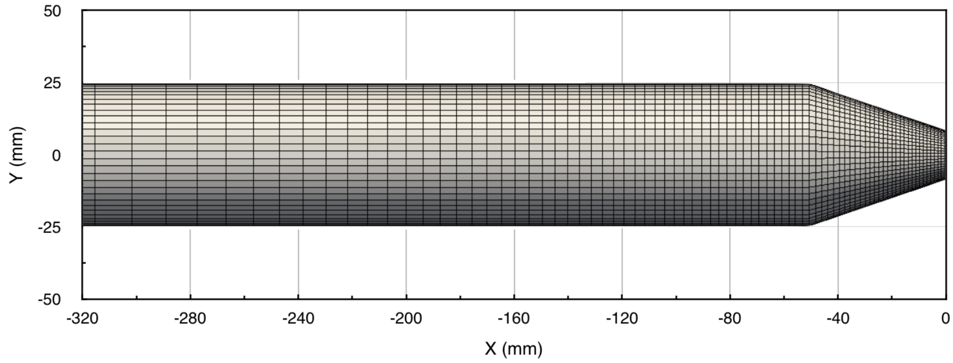

(a) Upstream feeding line progressive refinement

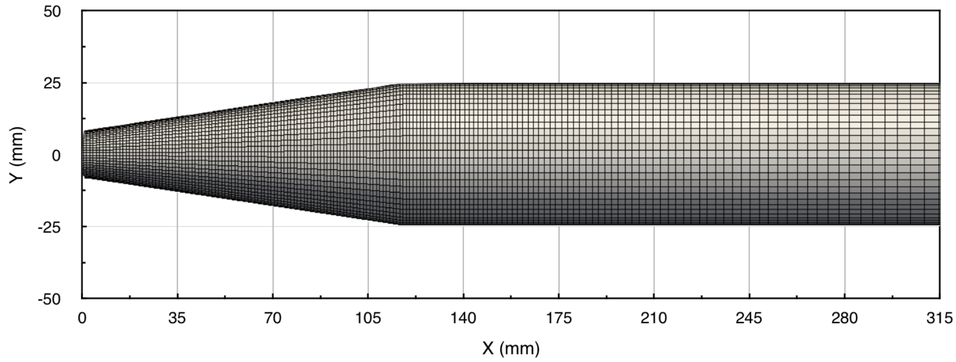

(b) Downstream feeding line progressive refinement

Figure 4.8: Refinement of the mesh at the end of the upstream feeding line (left) and at the beginning of the downstream feeding line (right).

For this study, five grids, denoted as lvl_0, lvl_1, lvl_2, lvl_3 and $lvl_4$are created. Table 4.1 detail the number of cells for each grid in the whole geometry and in the nozzle.

Table 4.1: Parameters of the numerical grids employed.

Grid Level	hi/h	Number of cells (Total)	Number of cells (Diverging nozzle)
lvl_0	1.71	188672	63072
lvl_1	1.46	304317	102340
lvl_2	1.26	468195	148992
lvl_3	1.11	691600	215820
lvl_4	1	939550	302500

The grids are aimed to be geometrically similar. Thus a constant coefficient is applied in order to coarsen the mesh. lvl_4 is the most refined grid whereas lvl_0 is the coarsest one. h_i/h is used to characterise the progressive refinement of the mesh (see Rosetti [30]).
The grid parameter is $h = (1/N_{cells})^{1/3}$. Figure 4.9 shows the different refined grid lvl_1, lvl_2, lvl_3 and lvl_4 with a cross sectional view of the converging nozzle at its beginning. The lvl_0 grid can be observed in figure 4.7

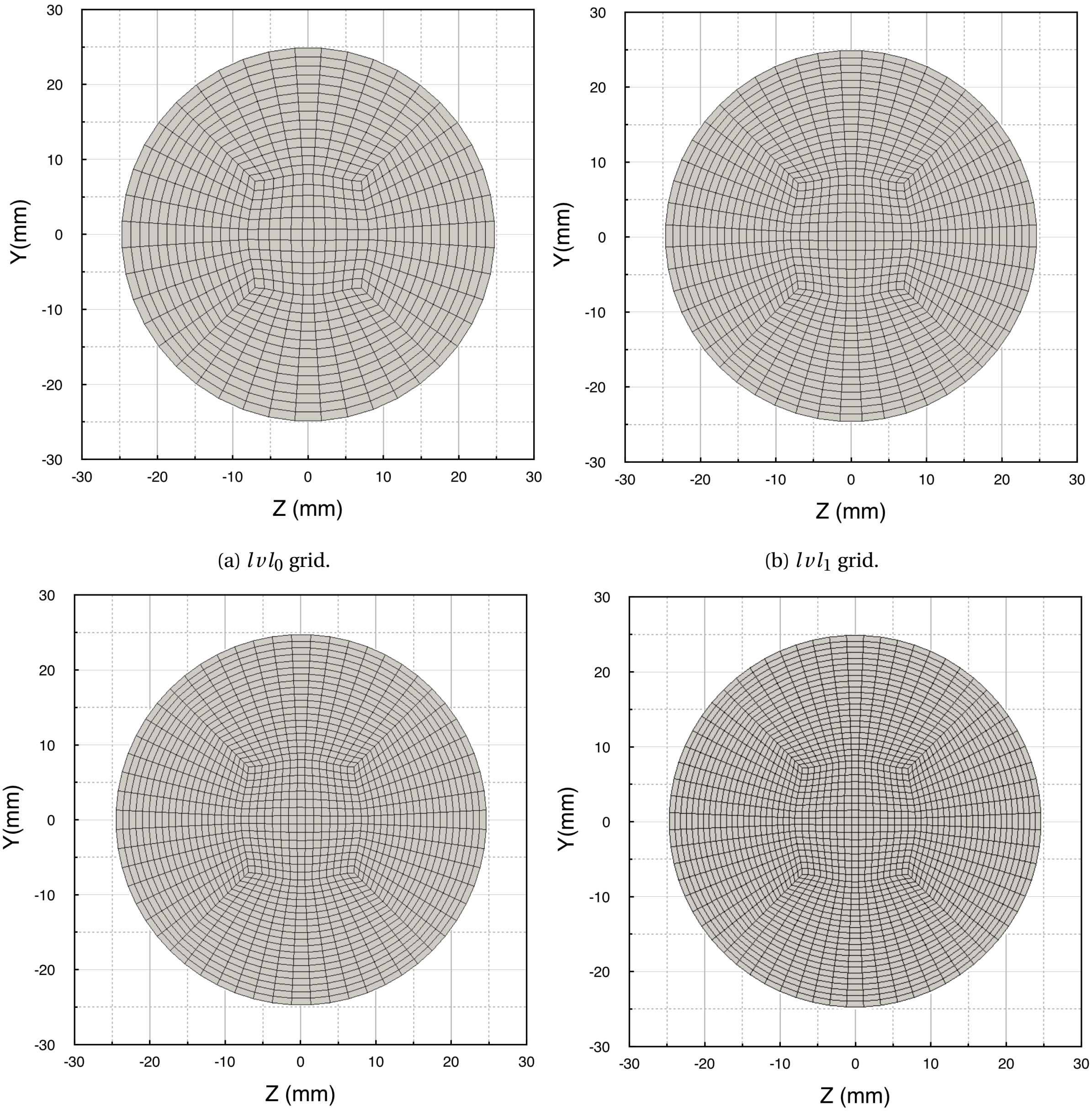

(a) lvl_0 grid. (b) lvl_1 grid.

(c) lvl_2 grid. (d) lvl_3 grid.

Figure 4.9: Cross sectional view of the throat of the venturi, progressive refinement of the grid.

O-grid have all the same geometry for every part of the numerical setup. No refinement at the wall can be observed, due to the use of an inviscid solver.

4.3. Implementation on OpenFOAM

4.3.1. Discretization

OpenFOAM is an opensource code used to discretize and resolve the Navier-Stokes equations. In this solver, the finite volume method (FVM) is used for the discretization of the different equations.

4.3.2. Implementation of the solver

The chosen solver is a modified interPhaseChangeFoam where the computations performed are for an inviscid flow.
The solver loop is shown on figure 4.10

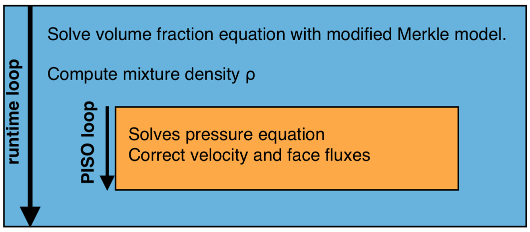

Figure 4.10: Flowchart of the solver used for the computations of this study for one iteration.

Initial and boundary conditions For every computations, the velocity u at the inlet and the pressure at the outlet of the downstream diffuser $p_{outlet,d}$ are fixed, based on the experimental conditions [15].
Since an inviscid model is used in this study, a slip condition for the velocity u at the wall is implemented.
The temperature T, liquid and vapour density ρ_l and ρ_v are obtained from the experimental data [15].
For every cavitating computation, a wetted flow simulation where no cavitation occurs is first performed in order to have a more realistic initial condition where the cavitation model is switched on. The modified Merkle model is implemented once the wetted simulation has converged.

4.3.3. Probing of the geometry

In the experimental setup, optical access to the region of the Venturi is provided with a high speed camera where the flow is captured. Two transducers are also placed in the experimental set-up. One in the upstream feeding line, one in the downstream feeding line. Positions 1 and 2 in Figure 4.1 indicate the location of static pressure transducers P1 and P2. For the numerical study, the velocity u, pressure p, liquid fraction γ and density ρ are also probed in different parts of the geometry.

Measure of the pressure inlet and outlet First, Figure 4.11 shows the pressure inlet and outlet where Hogendoorn [15] measured the pressure in order to calculate the pressure loss K. The same procedure is applied for this computation.

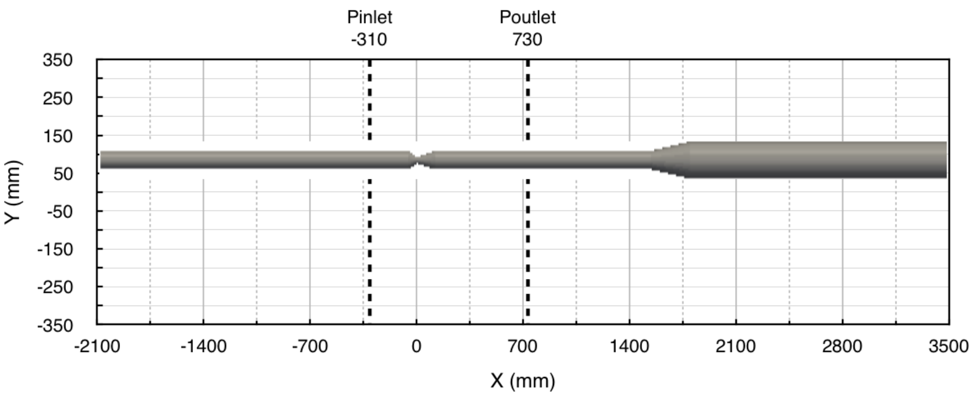

Figure 4.11: Side view (x-y plane) of the venturi, with the diverging and converging nozzle.

Measure at the diverging nozzle With a python script, a circular plane consisting of 120 circles equally reparted along the diverging nozzle is created. In these planes, 10 different points are selected where the different values will be taken. This results in the probing of $120 \cdot 10 = 1200$points. Thus, for every circle, each values can be averaged based on the 10 points reparted along the circle.
The distance between the probing plane and the wall is made constant for all the study cases, and is equal to $n_p = 2$mm

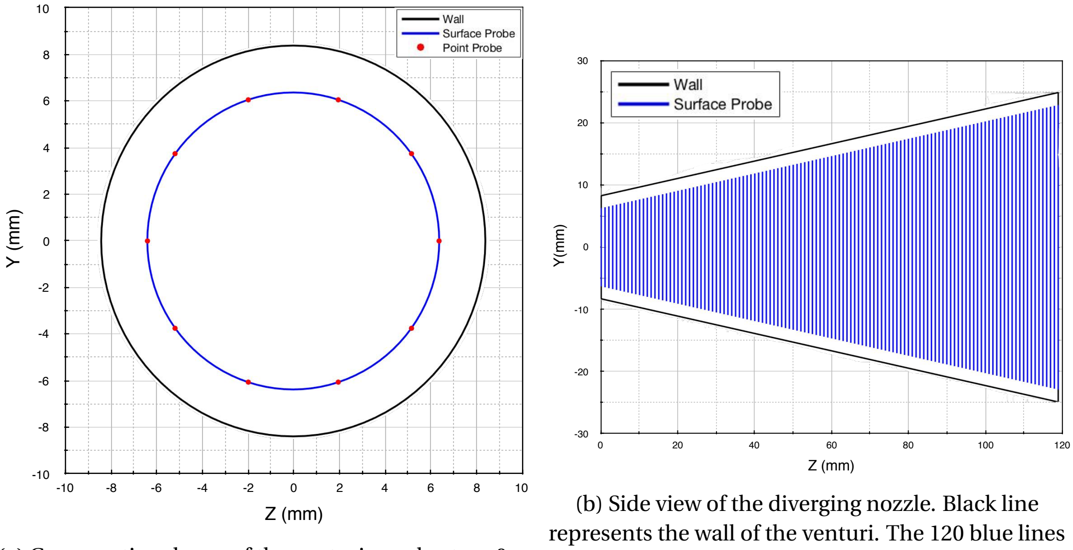

(a) Cross sectional area of the venturi nozzle at x = 0m. The black part represents the wall, the blue line the circle where 10 points (red dots) are selected and use for probing

(b) Side view of the diverging nozzle. Black line represents the wall of the venturi. The 120 blue lines represent equidistant circles where the probing is done

Figure 4.12: Probing points at the diverging nozzle for the construction of the X-t diagram.

4.4. Test cases implemented

The bubbly shock mechanism, re-entrant jet mechanism and transition regime are investigated in this study. Thus, a total of three test cases is implemented in order to visualise these different shedding mechanisms. Table 4.2 introduces the different test cases which are performed in this thesis and the number corresponding to the order of numerical study.

Table 4.2: Test cases studied.

Test Case	Regime studied
1	Bubbly shock mechanism
2	Re entrant jet mechanism
3	Transition regime

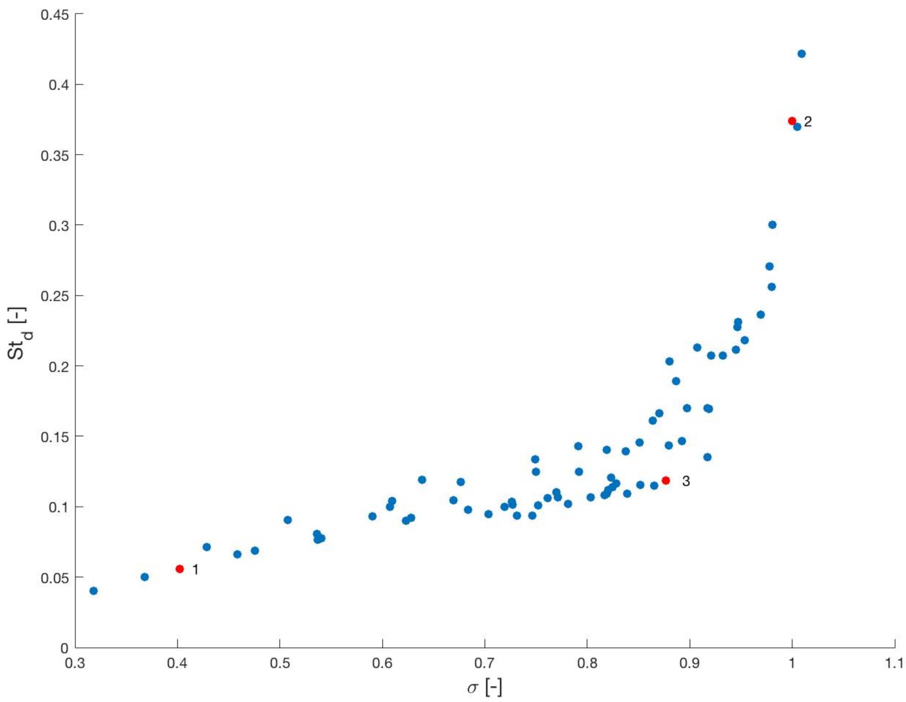

Figure 4.13: Cavitation number as function of the Strouhal number obtained experimentally [15].

Figure 4.13 summarises on the diagram obtained by Hogendoorn [15] where the different test cases were plotted. The bubbly shock test case (red dot 1) is found to be at the left extremity of the diagram, corresponding to low cavitation number ($\sigma = 0.40$) and low Strouhal number, whereas the re-entrant jet test case (red dot 2) is found at the other extremity, corresponding to high cavitation number ($\sigma = 1$). The transition regime (red dot 3) is found between the two test cases, at $\sigma = 0.89$.

4.5. Convergence study

4.5.1. Transient Scanning Technique (TST)

In order to verify the statistical convergence of our computations, the technique called ' Transient Scanning Technique, or TST based on the work of Brouwer [3] [2] is used. This technique is based on the behavior of the random uncertainty of the mean. Start-up en end effects can be identified and removed from the signal, and the random uncertainty of the mean can be accurately estimated .

The cumulative u_1 is calculated at every time T, using a signal resulting from the computations, with the following equation :

$$u_1 = \sqrt{\frac{1}{T}\int_0^T (1-\frac{\tau}{T})C_{xx,biased}(\tau)d\tau} \tag{4.1}$$

Where $C_{xx,biased}(\tau)$ is the biased estimator autocovariance, given in [3].

4.5.2. Grid and time step refinement study

A grid and time step refinement study estimates the discretization error in the computation. This method for such a study is described for Eą and Hoekstra [8]. It states that calculations are done for a grid and time step series, with decreasing time step and cell size. Then, a power function can be fitted to the results in a least square senses.
The general equation is given by :

$$\epsilon_\phi \simeq \phi_i - \phi_0 = \alpha_1 h^{p_x} + \alpha_2 h^{p_t} \tag{4.2}$$

ϕ being the parameter considered for this refinement study and estimated by a function based on the typical size of power p_x and on the typical time step size of power p_t. This method only works for geometrically similar mesh, which is the case in this study.
The verification and validation tool developed by refresco and available at http://www.refresco.org/verification-validation/utilitiesvv-tools/ is used.

5

Bubbly shock mechanism

This chapter further examines the results of the CFD computations implemented to visualize the bubbly shock mechanism and predict the three dimensional characteristics of the unsteady cavitation dynamics. The simulation setup is in line with Hogendoorns' experiments [15]. After the validation and verification of the computations performed, the results are intepreted. First the instantaneous flow topology is to be discussed, before presenting the X-t diagram, which gives access to the temporal evolution of the shedding process. Finally, a comparison between experimental results and results from CFD computations is done.

5.1. Simulation set-up

5.1.1. Boundary conditions

In order to implement the right boundary conditions to simulate a bubbly shock mechanism, the Strouhal-Cavitation number diagram presented in Chapter 2 is used as a reference for the computations.
The reference point taken for this study case is presented in Figure 4.13. In order to simulate the bubbly shock mechanism, a low cavitation number is implemented.
Hoogendoorn [15] specified the operating point of the measurement by measuring the outlet pressure at the end of the downstream diffuser $p_{outlet,d}$ and inlet velocity u. The liquid Density and vapor density were obtained with Antoine's equation and by measuring the temperature in the experimental facilities. Table 5.1 presents the parameters of the experiments performed to study the case showed in Figure 4.13. In the experiments, $p_{outlet,d}$ = 40 kPa, giving a cavitation number of $\sigma = (p_{outlet,d} - p_{vap}/(\rho u_0^2/2) = 0.40$.

Table 5.1: Boundary conditions and flow properties for the bubbly shock mechanism simulation.

Parameters	Value
Fluid	Water
Temperature T [$°C$]	19.1
Outlet pressure $p_{outlet,d}$ [kPa]	40
Inlet velocity u [$m.s^{-1}$]	1.48
Liquid density ρ_l [$kg.m^3$]	999.18
Vapor density ρ_v [$kg.m^3$]	0.0124
Saturation pressure p_v [Pa]	2206
Cavitation number σ []	0.40

5.1.2. The simulations conducted

Table 5.2 summarises the simulations conducted, showing the time step Δt, interval used for statistical sampling and the physical time.

Table 5.2: Overview of simulations conducted for the Bubbly Shock Case.

Grid level	Time step Δt (s)	Sampling interval (s)	Physical run time (s)
lvl_0	1×10^{-6}	1×10^{-6}	0.5
	2×10^{-6}	2×10^{-6}	0.5
	4×10^{-6}	4×10^{-6}	0.5
lvl_1	1×10^{-6}	1×10^{-6}	0.5
	2×10^{-6}	2×10^{-6}	0.5
	4×10^{-6}	4×10^{-6}	0.5
lvl_2	1×10^{-6}	1×10^{-6}	0.5
	2×10^{-6}	2×10^{-6}	0.5
	3×10^{-6}	3×10^{-6}	0.5
	4×10^{-6}	4×10^{-6}	0.85
lvl_3	1×10^{-6}	1×10^{-6}	0.5

Four different grids, denoted as lvl_0, lvl_1, lvl_2 and lvl_3, presented in Chapter 4 are used for this computation. For every case, the sampling interval of velocity, density, pressure and liquid fraction is equal to the time step Δt.

5.2. Verification

5.2.1. Statistical convergence

Transient Scanning Technique presented in Chapter 4 is implemented for this study case.

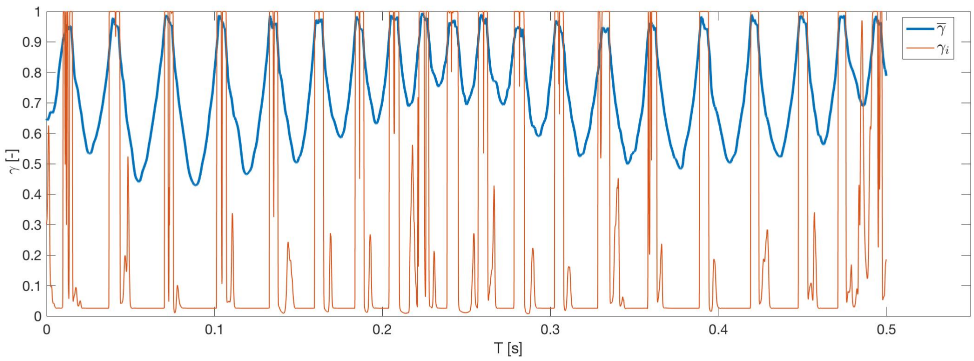

Figure 5.1: Signals used for the statistical convergence study : Average liquid fraction $\overline{\gamma}$ (blue) and liquid fraction at a discrete location γ_i (red). Values obtained for the lvl_3 grid at time step $\Delta t = 1 \cdot 10^{-6}$s.

Two signals are chosen for this convergence study and are shown in Figure 5.1 : the average liquid fraction value in the diverging nozzle $\overline{\gamma}$, a global signal and the liquid fraction in a discrete location of the wall of the venturi γ_i.Both directly linked to the shedding frequency of the partial cavities. A total time of 0.5 s is taken for the analysis of every computations.

Figure 5.1 shows values taken for the test case which uses the lvl_3 grid at time step $\Delta t = 1 \cdot 10^{-6}$. Values of $\overline{\gamma}$ oscillates between 1 and 0.5, which means there is a pretty high cavitation intensity for this test case.

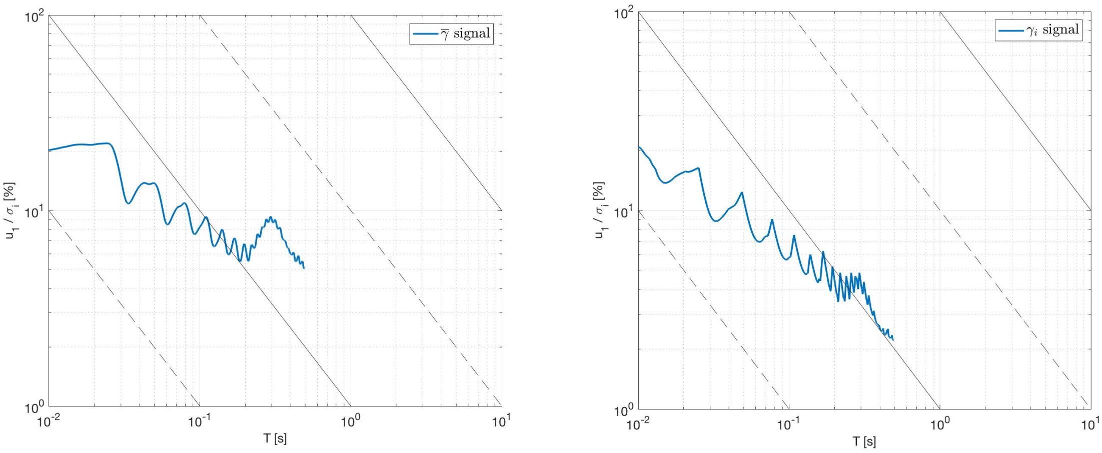

(a) TST-B for $\overline{\gamma}$.

(b) TST-B for γ_i.

Figure 5.2: Numerical uncertainty of the mean over time computed from TST-B for $\overline{\gamma}$ (a) and γ_i (b). Values obtained for the lvl_3 grid at time step $\Delta t = 1 \cdot 10^{-6}$ s.

Figure 5.2 shows that both TST-B have a large range where u_1/σ_i decays with the inverse of T, following the slope $1/T$. No hockey stick are present of the two plots meaning no start up effects are present for these computations. Numerical uncertainty reaches 5% for $\overline{\gamma}$ and around 2.5% for γ_i, which is acceptable for the this test case. A jump can be observed in Figure 5.2a around 0.3 second, the numerical uncertainty of the mean increasing from 6% to 9% before decreasing and aligning with the slope $1/T$. This follows a " contraction " of the shedding frequency and the average liquid value $\overline{\gamma}$ observable in Figure 5.1 and is explained in this chapter later on.

5.2.2. Flow properties and pressure loss

Once the computation is performed and the statistical convergence is achieved, a first comparison between the experiments and the CFD results can be made.

Table 5.3: Flow properties up and downstream of the venturi ; Comparison between numerical results on grid lvl_2 and the experimental reference of Hogendoorn [15].

$P_{inlet,exp}$ (Pa)	$P_{inlet,sim}$ (Pa)	$P_{outlet,exp}$ (Pa)	$P_{outlet,sim}$ (Pa)	K_{exp} (-)	K_{sim} (-)
110384	135363	25702	39424	0.9011	1.0209

Table 5.3 presents the pressure computed and sampled at the inlet and outlet of the venturi and the experimental reference. With this, the comparison between the flow properties of the computations and the experiments is done. This study is made to ensure the reliability of the simulations compared to the experiments. Experimental and numerical pressure loss are plotted in Figure 8.1 in Chapter 8.

Simulations predict a constant overpressure at the inlet compared to the reference experiment, raising the pressure difference between inflow and outflow and increasing the driving forces.

If the simulated pressure drop can be considered close to the pressure drop obtained experimentally, a higher one is obtained with CFD computations. Pressure loss calculated is constant along the different computations performed. This overestimation of pressure loss is common and present in a large number of studies.

Two factors can be presented to explain the higher pressure drop in the simulation. Vapour structures can cause a blockage effect, leading to additional pressure losses. In the present case, vapour structures often reaches the end of the diverging nozzle and cavitation can be observed in the pipe after it. Thus, the mean amount of vapour produced in the computations seems to be larger compared with the experiments, whichexplains the higher pressure drop in the simulations. Another explanation can be the higher pressure measured on the upstream flow, which has a large influence on the overall pressure drop. Results presented in Table 5.3 show indeed that it is the inlet pressure which is the most overestimated when compared to the outlet pressure.

5.3. Instantaneous flow topology

Figure 5.4 presents instantaneous simulation results. For a visualisation of the numerical results, different isosurfaces of the liquid fraction were plotted and are presented in Table 5.4.

Table 5.4: Isosurfaces of liquid fraction γ plotted in function of opacity for the instantaneous simulation results.

Isosurfaces γ	Opacity
0.8	0.1
0.6	0. 3
0.4	0.5
0.2	0.7
0	0.9

An area of low liquid fraction and high void fraction is represented by darker shades. This coloring is done in order to match the X-ray densitometry measurements performed by Hogendoorn [15] in order to make the most accurate comparisons possible between CFD computations and the experimental results presented in figure.

For illustration of the shedding process, fourteen representative time instants were selected in Figure 5.4 (a-n), exhibiting the growth and the progressive shedding of the cavity due to the bubbly shock mechanism.

Figure 5.4 (a) presents the beginning of the formation of the cavity inside the diverging nozzle. It appears at the throat of the venturi and the sheet is already developed at the beginning of the diverging nozzle. Furthermore, cavitating vortices are also situated in the rest of the nozzle. Their lighter shades indicate they are cloud cavitation structures. From $t = t_0$ to $t = t_0 + 11$ms, the cavity continues to grow and develop inside the nozzle, as shown in Figure 5.4(a)-(d). The growth seems constant over time. Moreover, cavitating vortices continue to be advected by the flow and begin to leave the nozzle.

In Figure 5.4(e), at $t = t_0 + 13$ms, all the cavitation structures which were present after the cavity have disappeared and the cavity has stopped growing. The cavitating vortices seem to have collapsed, giving birth to a propagating shock in every direction. The shock front encounters the cavity at $t = t_0 + 13$ ms as shown in Figure 5.4(e).

Figure 5.4(f)-(g) shows the situation just after the shock front hit the partial cavity. The end of the cavity is disturbed, and lighter shades appear.

Figure 5.4(f)-(l) shows the passage of the shock in the Venturi and the progressive shedding of the cavity. The shock front cause the cavity to shed and transform into cloud cavitation, where horseshoe-type structures can be observed, for example at $t = t_0 + 29$ms in Figure 5.4(k). These patches of cavitation are connected by streamwise-oriented vortices. It appears that the more the shock front approaches the apex, the higher its traveling speed.

Finally, in Figure 5.4(m), the cavity is detached from the apex and the separated cloud is convected further downstream. It is to be noted that the simulation exhibits large cavitating vortices structures which seem to wrap around the cloud, and are oriented in the streamwise direction.

The maximum cavity length can be determined at this instant. It is not rare that the cavity has a length superior to that of the diverging nozzle. Figure 5.3 shows this maximum cavity length by dezooming Figure 5.4(m).

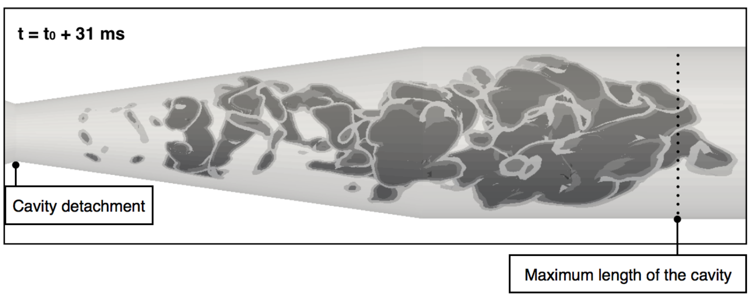

Figure 5.3: Side view of the venturi at the time instant of the cavity detachment. Determination of the maximum cavity length.

A new sheet cavity starts to develop in Figure 5.4(n) while the separated clouds continue to be advected. Here, the whole shedding process lasted around 31 ms, which gives a frequency of approximately 32 Hz. These illustration of a typical shedding cycle dominated by the bubbly shock can be compared to the experimental results presented in chapter 2 in Figure D.1. Both simulation and experiments were done for the same conditions, with $\sigma = 0.40$ ($u_0 = 13.7$m/s and $p_{outlet,d} = 40$kPa). The length of the partial cavities are approximately the same and the simulations exhibit the same amount of large-scale cavitation compared to the experiments.

The shedding process can also be visualised by taking a mid plane slice. For this purpose, Figure 5.5 shows a series of six consecutive time instants in the form of the instantaneous liquid fraction γ, horizontal velocity U_x and pressure p in the diverging nozzle. All these values were taken in a mid-plane slice. In order to relate the fields of velocity and pressure to the occurrence of cavitation, isocontours of γ were included in (b) and (c).
At the first instant $t = t_0$, the attached sheet cavities reaches its maximum length and almost enter the upstream feeding line. The liquid fraction attains value of 0.2. Within the sheet, two parts can be distinguished for the local velocity. It seems a pre-detachment is present at the beginning of the cavity. On the left of this pre-detachment, the velocity is similar to the velocity of the flow whereas after the pre-detached frontier, the horizontal velocity U_x (which can be associated with the streamwise velocity as the y-component of the velocity is negligible) is small and directed downstream. Concerning the pressure, the value is close to to the vapor pressure of 2200 Pa. Shortly after, at $t = t_0 + 6$ms, a shock front forms at the upstream part of the cavity, parallel to the curve of the diverging nozzle.
From $t = t_0 + 6$ms to $t = t_0 + 12$ms, the shock front propagates counter to the flow. This causes the cavity to decrease in length, and a front appear. The cavity at the left of the front is characterised by low liquid fraction value whereas directly after it, the liquid fraction drastically increase to be equal to 1, meaning there is no more cavitation. This discontinuity is more obvious when observing U_x. Across the shock, the velocity is negative, on the opposite of the flow, and the static pressure increases.
A shear layer can be observed being form between the free stream and the upstream-directed flow behind the shock and exhibits Kelvin-Helmholtz instability, visible for the velocity pictures at $t = t_0 + 12$ ms and $t = t_0 + 16$ms. It is to be noted that the shock front does not appear uniformly across the Venturi. For example, at $t = t - 0 + 12ms$, this seems more advance at the bottom when compared to the top, where the cavity length is more important. New cavity structures form behind the shock front, consequential of the progressive detachment of the cavities and the low-pressure vortex cores. They roll up into a cloud, as observed for example at $t = t_0 + 22$ms.
Complete detachment of the cavity appears at $t = t_0 + 18$ms, and cloud cavitation propagate downstream, being advected by the flow. A new shedding cycle can then begin, with the apparition of a new sheet cavity at $t = t_0 + 22$ms.

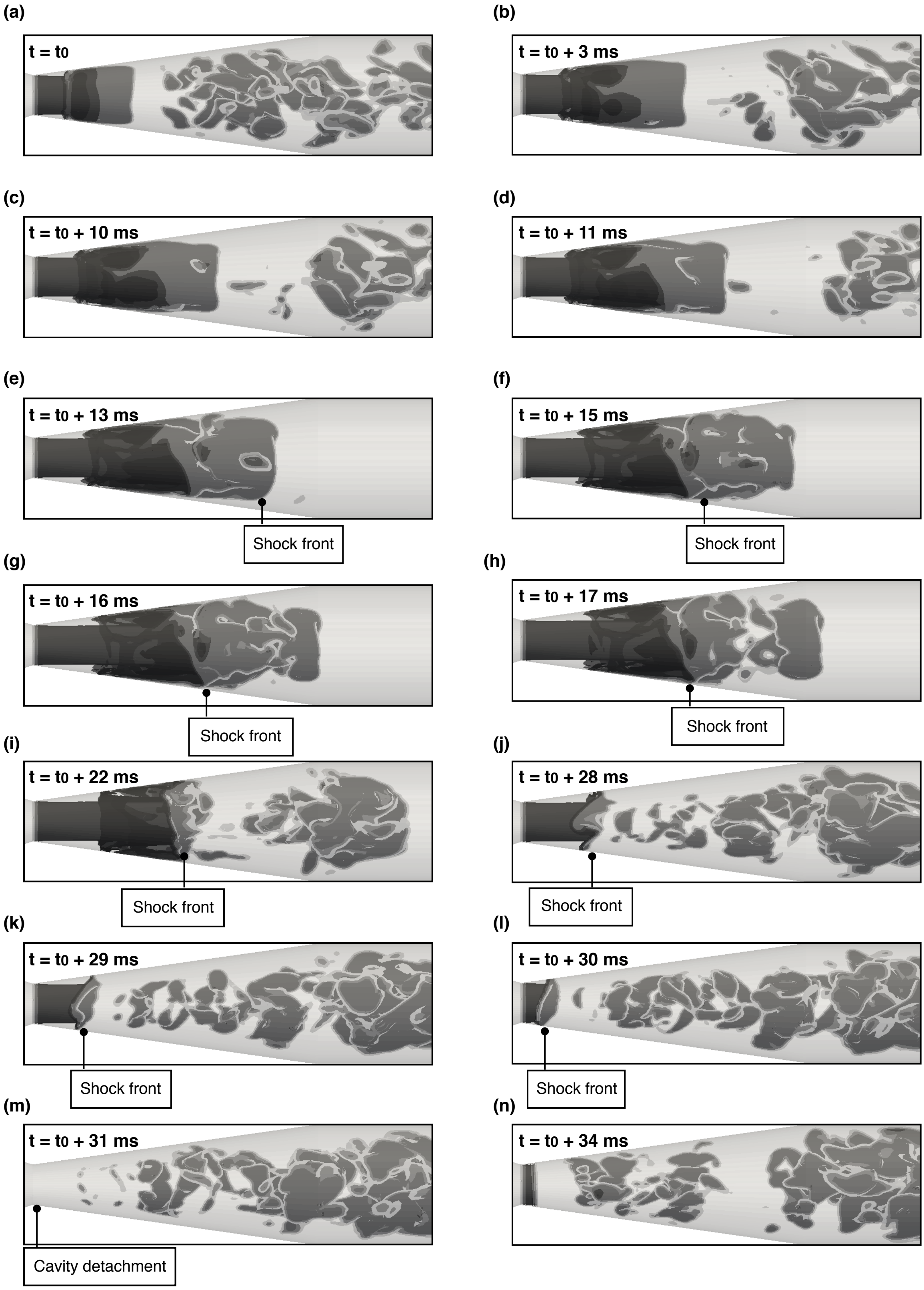

Figure 5.4: Illustration of a typical shedding cycle dominated by the bubbly shock mechanism (side view). Numerical results show vapour structures with different isosurfaces at different opacity. Simulation on the lvl_2 grid for $\Delta t = 1 \cdot 10^{-6}$ s.

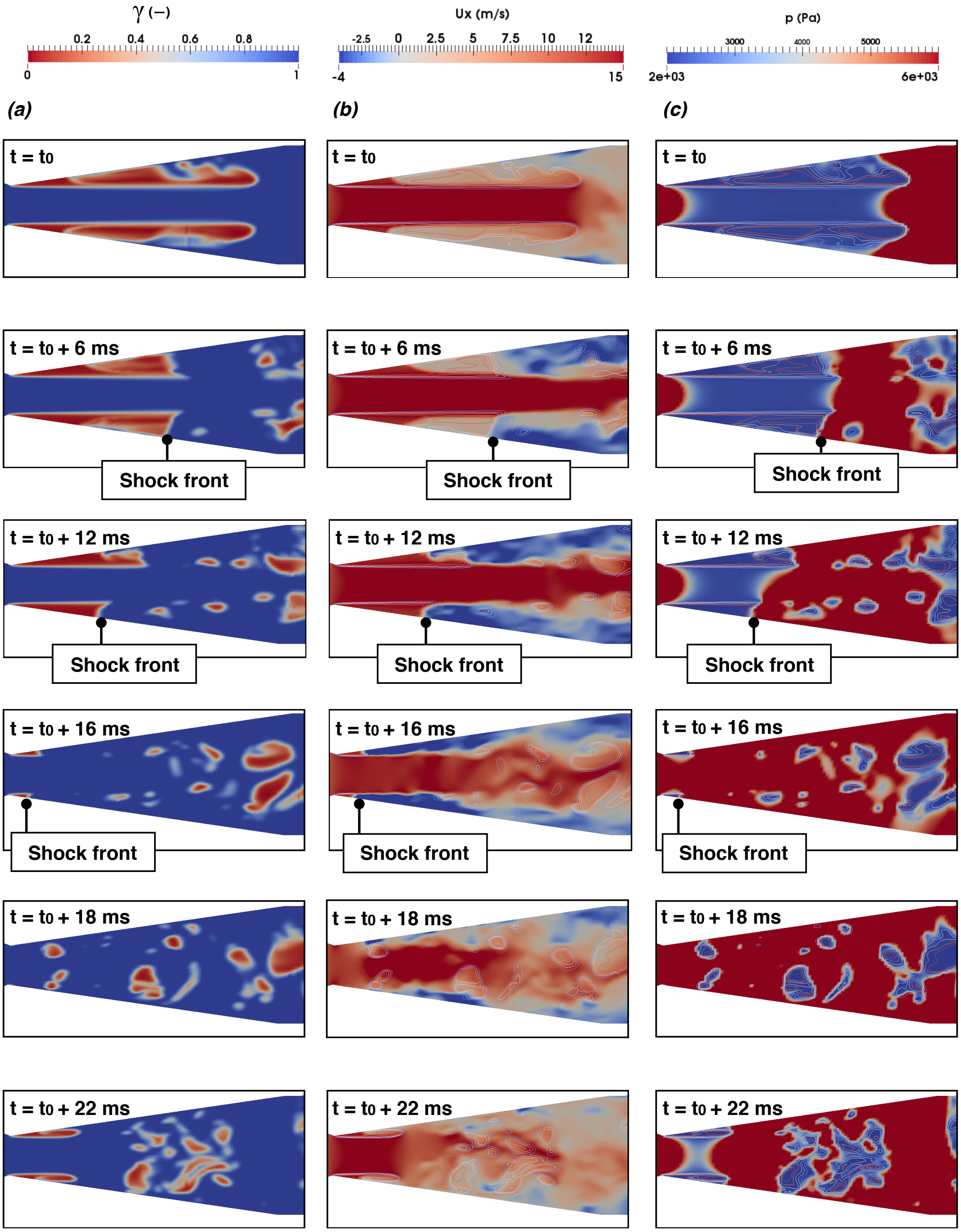

Figure 5.5: Instantaneous flow field captured in a mid-plane slice during a shock dominated shedding cycle for six consecutive time instants. Numerical prediction on the grid. Comparison between (a) liquid fraction γ, streamwise velocity U, and (c) pressure p.

5.4. Temporal evolution of the shedding process

5.4.1. X-T diagram

The shedding process could be visualised by capturing the instantaneous flow field at certain time, but only for one shedding cycle and parameters such as the shedding frequency, length of cavity or the propagation speed of the shock front could not be accurately predicted. To further analyse across multiple cycles of shedding process, the temporal evolution of the spanwise-averaged flow on a plane at a normal distance parallel to the Venturi can be recorded. The sampling of the values was explained in Chapter 4. Choosing a parallel cylinder at $n_p = 2mm$ from the wall, Figure 5.6 shows the obtained variation in time for the liquid fraction γ, plotted along the X direction for a total time of 0.5 s.

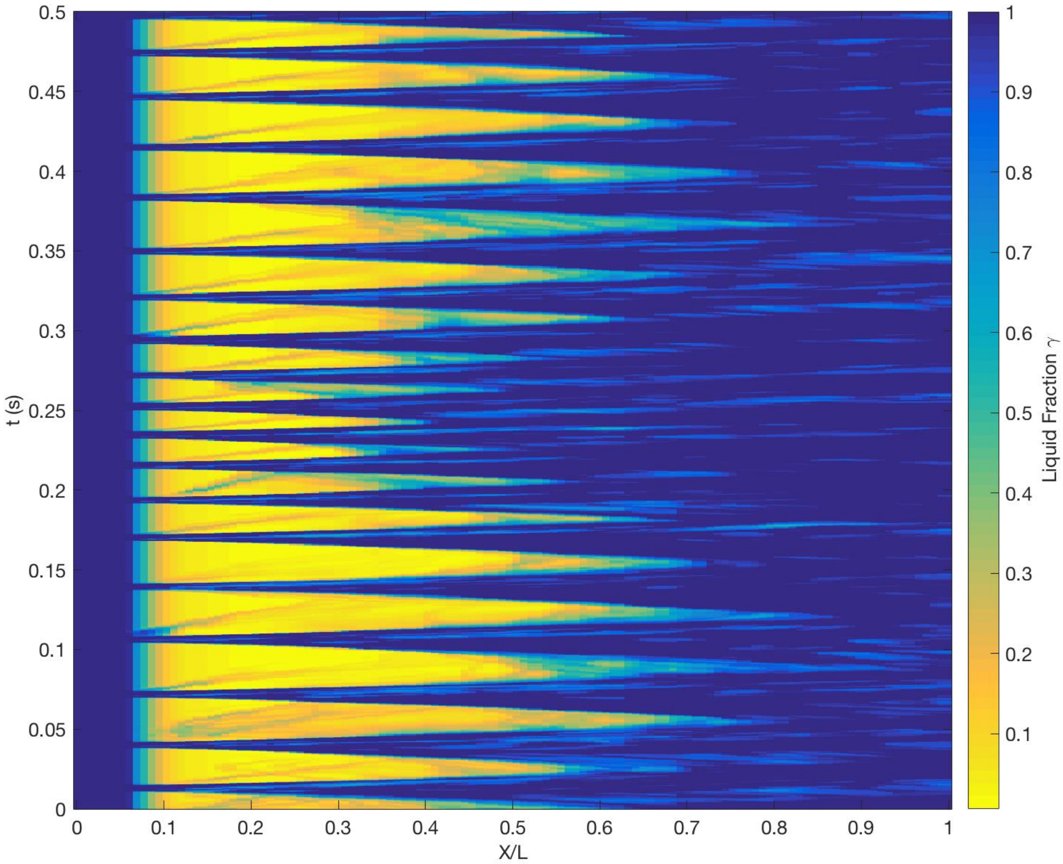

Figure 5.6: Time evolution of the shedding process over a period of 0.5 s; numerical prediction on the lvl_2 grid. Spanwise-averaged quantities are extracted from a parallel plane at a normal distance of n = 2 mm and plotted along the diverging nozzle. Further is $\sigma = 0.40$ ($u_0 = 13.7 m/s$ and $p_{outlet,d} = 40$kPa). Sampling frequency $F_s = 1000 kHz$).

Individual shedding cycles can be identified distinctly by the yellow triangular shapes of Figure 5.6 and can be compared with the results of Budich et al [4] and Ganesh [13] [12] . No cavitation sheets are present between 0 and 0.08 in the X/L direction, because the plane of $n_p = 2mm$ is to distant from the wall to observe cavitation at the throat. The first instant of the shedding cycle is represented by the growing portion of the yellow shapes, meaning the cavity expand through the nozzle. For most cycles, typical liquid fraction in the attached sheet are below 30 %. During the growth of the cavity, and in the cavity apex, liquid fraction increases.

After reaching a maximum length, shedding occurs as shown in Figure 5.6. Due to the collapse process, the triangular shape decreases in length until reaching the wedge apex, where the cavity is detached and a new cycle can begin. Behind the shock, the liquid fraction γ increases drastically and often reaches the value of 1, meaning there is only liquid water.
It is observed that if the shapes which defines the shedding cycle are similar, they are not identical, meaning each shedding cycle is different. Indeed, the maximum length reached by the cavity before the condensation shocks is different along all triangular shapes, and some shedding process occur faster than other.

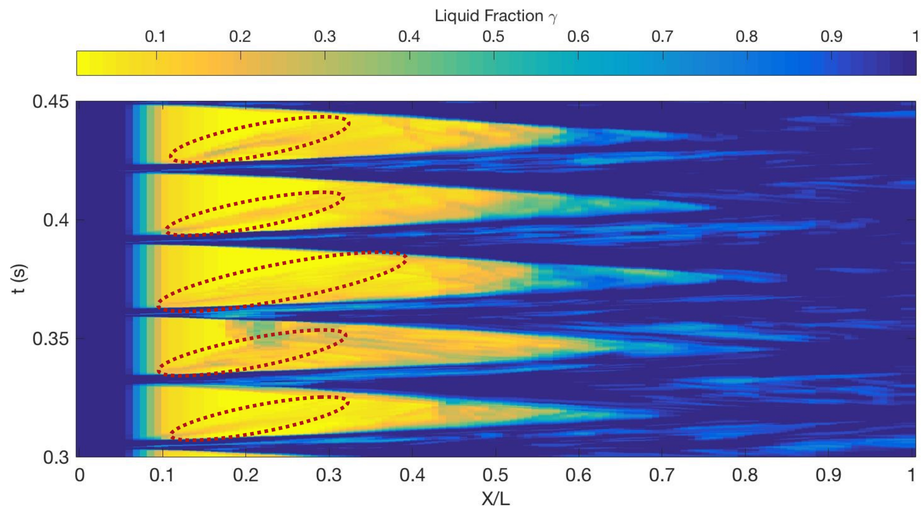

(a) Pre detachment observed on the X-t diagram.

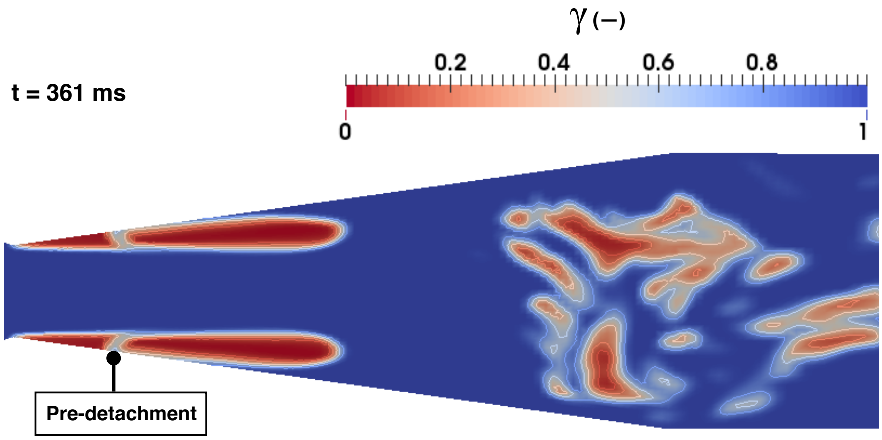

(b) Pre-detachment observed on the mid span slice.

Figure 5.7: Visualisation of a pre-detachment of the sheet cavity in the X-T diagram (a) and in mid-slice plane (b). Both pictures were the results of the simulation with the lvl_2 grid for a time step of $\Delta t = 1 \cdot 10^{-6} s$.

Figure 7.2 shows a close up view of the X-t diagram constructed in Figure 5.6. Inside all triangular shapes, an area of increased liquid fraction can be found, separating the the triangles. This can be assimilated to a pre detachment of the partial cavities and which occurs at the same point of the venturi for every shedding process. This pre detachment ravel at the same time that the cavity is growing, before the bubble collapse. The physical explanation for this phenomenon could not be explain. The main hypothesis was that a preliminary bubble collapse occurred during the cavity growth, creating a shock front at a part of the Venturi, but not strong enough to travel back to the apex causing the shedding of the cavity.

Cavity length The cavity length l was determined in Hogendoorn's work [15] by measuring the cavity length at the instant of the detachment of the cavity to the apex, as shown in Figure 5.8. This could be determined thanks to the X-T diagram, as shown in Figure 5.8a. The position of the cavity was measured at the end of the triangular shape, which is synonymous of the detachment of the apex.

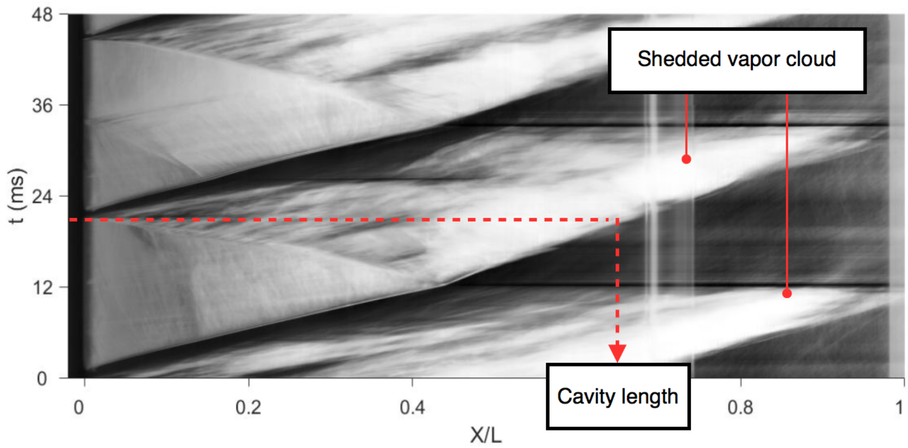

(a) Time evolution of the shedding process taken from Hogendoorn's results [15].

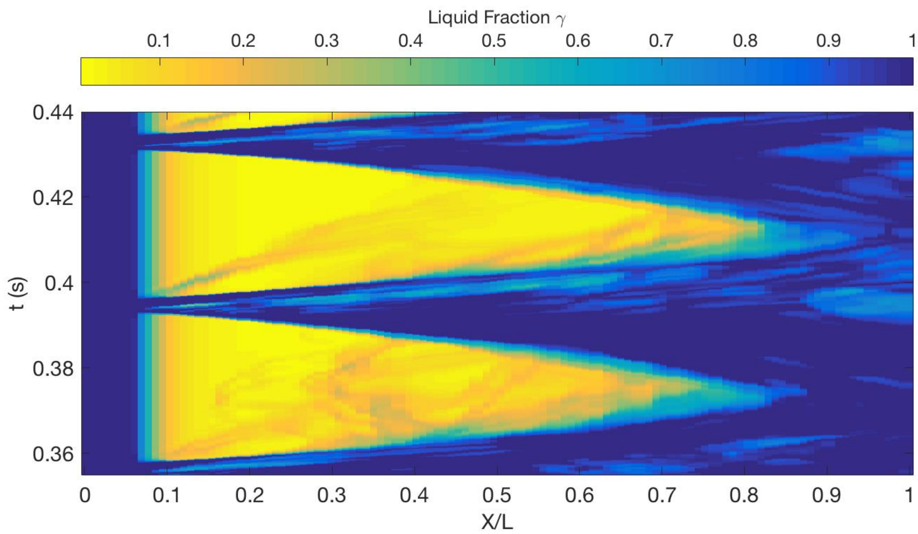

(b) Time evolution of the shedding process taken from Figure 5.6.

Figure 5.8: Time evolution of the shedding process taken from the X-t diagram represented in Figure 5.6 and taken from Hogendoorn [15].

Unfortunately, Figure 5.8b shows that this method of cavity length determination is impossible with the X-t diagram constructed in this study. Indeed, the X-t diagram is based on average values on a plane situated at 2mm from the walls of the venturi. This averaging and method of probing "erase" the vapor cloud which appears after the front shock. Only the triangular shape is visible on the contrary of the X-t diagram shown in Figure 5.8a where part of the vapor cloud is visible, making the determination of the cavity length possible. This is due to the method of construction of the X-t diagram, made with shadowgraphy.
Thus, the cavity length can not be determined with the X-t diagram plotted in this study. This can be done with Paraview, based on the pictures shown in Figure 5.4, but the results are not precise enough.

Velocity of the growing cavity, propagation speed of the shock X-t diagram can be used for the determination of the velocity of the growing cavity before the bubble collapse and the apparition of the shockwave, and also for the determination of the shock front velocity.

Figure 5.9 shows three triangular shapes more in detail, and were taken from Figure 5.6. Here, it is observed that the cavity growth is indicated by a positive linear slope. The velocity of the growing cavity is obtained by calculating the inverse of the slope, meaning that the cavity growth velocity is constant. On the contrary, the negative slope which corresponds to the shock wave propagation and the shedding of the cavity is not linear, but seems to have a second order polynomial fit. This matches the observations of Hogendoorn [15].

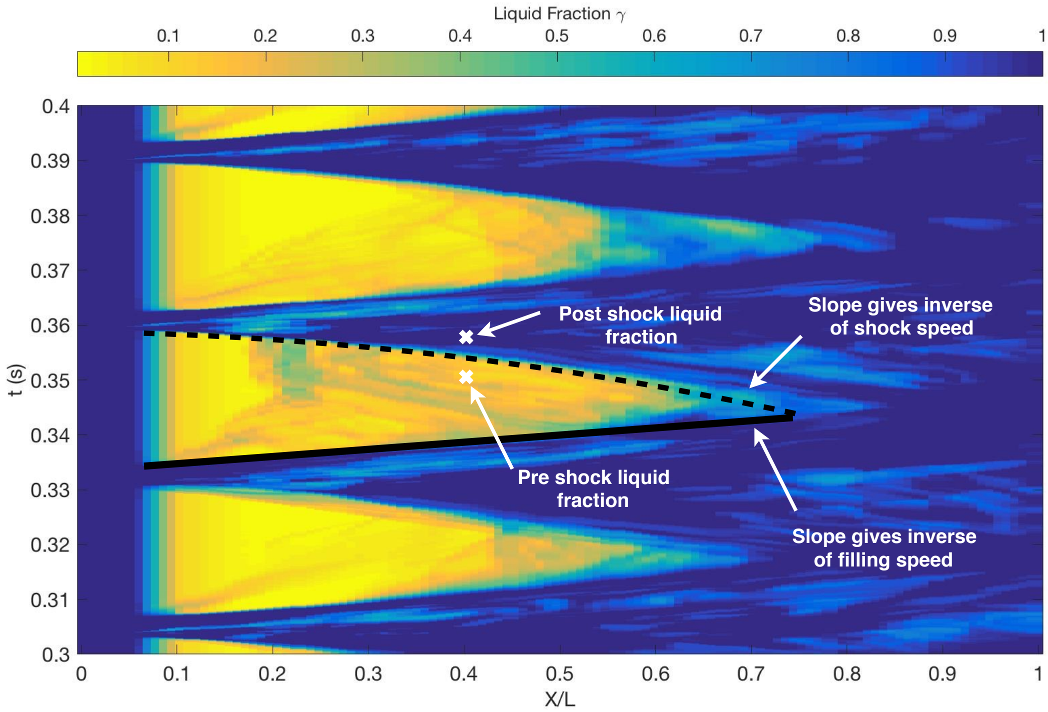

Figure 5.9: Time evolution of the shedding process over a period of 0.15 s taken from the X-t diagram represented in Figure 5.6.

Figure 5.10 shows the time evolution of seven shedding processes by plotting the liquid fraction γ (left picture) and the perpendicular velocity $u_{\perp}$ over time and along the diverging nozzle.

In order to determine the mean velocity growth of the cavities, a linear regression is applied for every triangular shapes. A mean velocity $\bar{u}_{growth} = 6.4$ m/s is found, with little differences between each shedding processes.

If the cavity growth has a constant velocity, this is not the case of the flow reversal responsible of the shedding of the cavity. Indeed, an acceleration of the condensation shock towards the apex is observed. This is caused by the fact that the liquid fraction in the sheet close to the apex decreases during the decrease of the cavity length, as seen from Figure 5.10 and 5.9.

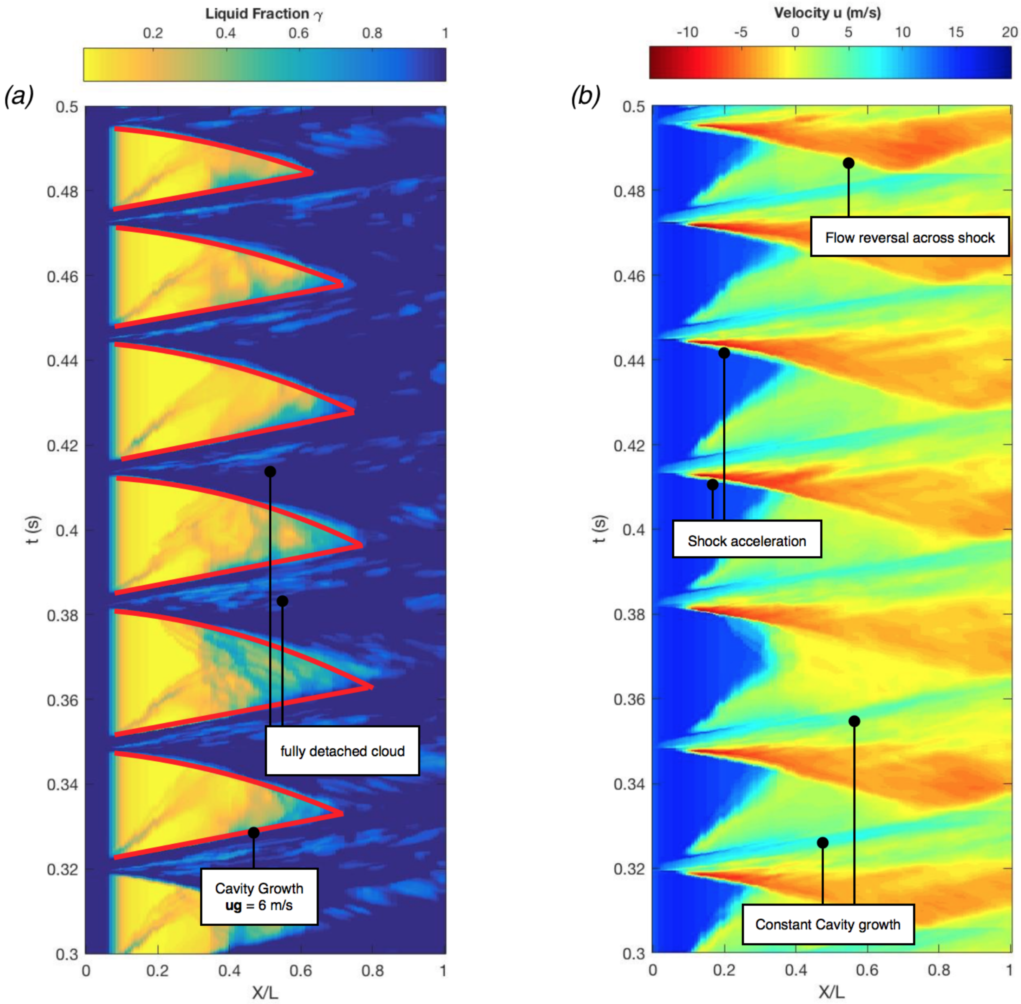

Figure 5.10: Time evolution of the shedding process over a period of 0.5 s; numerical prediction on the lvl_2 grid. Spanwise-averaged quantities are extracted from a parallel plane at a normal distance of n = 2 mm and plotted along the diverging nozzle. (a) is the liquid fraction, (b) is the velocity. Further is $\sigma = 0.40$ ($u_0 = 13.7$ m/s and $p_{outlet} = 40$ kPa). Sampling frequency $F_s = 1000kHz$).

This acceleration can be explained by the equation for the front propagation velocity relative to the upstream fluid u_{shock} in a bubbly flow. Demonstration of the following equation can be found in Appendix.

$$u^2_{shock} = \left(\frac{\gamma_2 + \frac{\rho_v}{\rho_l - \rho_v}}{\gamma_1(\rho_l - \rho_v) + \rho_v} \cdot \frac{1}{\gamma_1 - \gamma_2}(p_2 - p_1)\right) \tag{5.1}$$

which can be simplified, by neglecting the vapor density ρ_v into

$$u^2_{shock} = \frac{p_2 - p_1}{\rho_l} \frac{\gamma_2}{\gamma_1(\gamma_2 - \gamma_1)} \tag{5.2}$$

States upstream and downstream of the shock are denoted by subscripts 1 and 2. If the pressure drop $p_2 - p_1$ is assumed to be constant across the front, u_{shock} is expected to increase when γ_1 approaches the value of 0. As it can be seen in Figure 5.10, the velocity of the front which is situated upstream of the front is approximately constant, which means that the absolute velocity of the condensation front u_{shock} also increases.

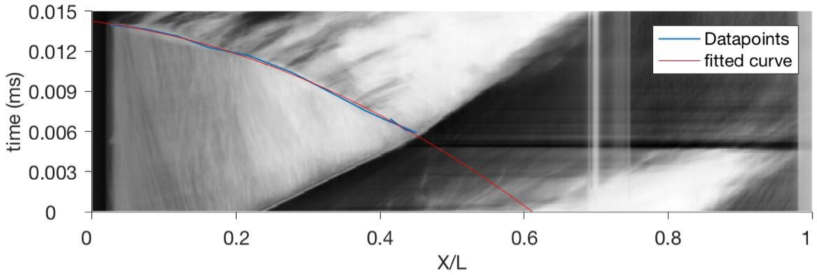

(a) Polynomial regression for the X-t diagram of Hogendoorn [15].

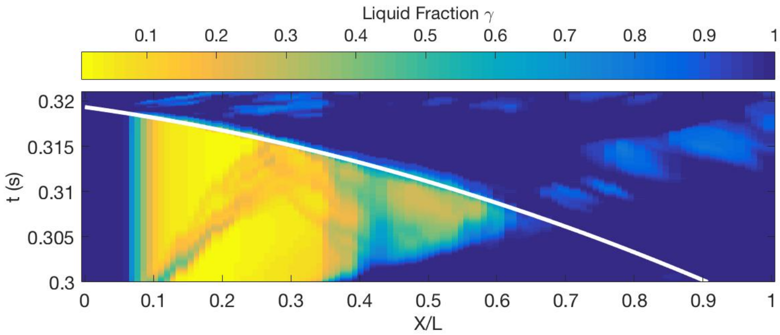

(b) Polynomial regression for the X-t diagram taken from Figure 5.6.

Figure 5.11: Polynomial regression performed for a shedding process, comparison between experiments [15] and simulations

A polynomial regression of order 2 is performed for the X-t diagram of Hogendoorn [15] in Figure 5.11a and for the X-t diagram computed in this study in Figure 5.11b in order to compare the condensation front u_{shock}. The regression lines which demonstrates the acceleration of the flow plotted in Figure 5.4.1 show the same behaviour.

5.5. Condensation shock phenomenon

5.5.1. Bubbly shock and pressure shock

The shedding process of the bubbly shock mechanism is based on the condensation and collapse of the cavities, which induces a pressure pulse propagating uniformly in all directions. The collapse of the cavities seem to be observed when visualising a shedding cycle in Figure 5.4 and 5.5.

Thus, pressure signals at different locations were plotted for a duration of T = 0.5 s where 20 shedding cycles are present. One of the signal was probed at the inlet of the Venturi whereas the other one was plotted at a random location in the venturi.

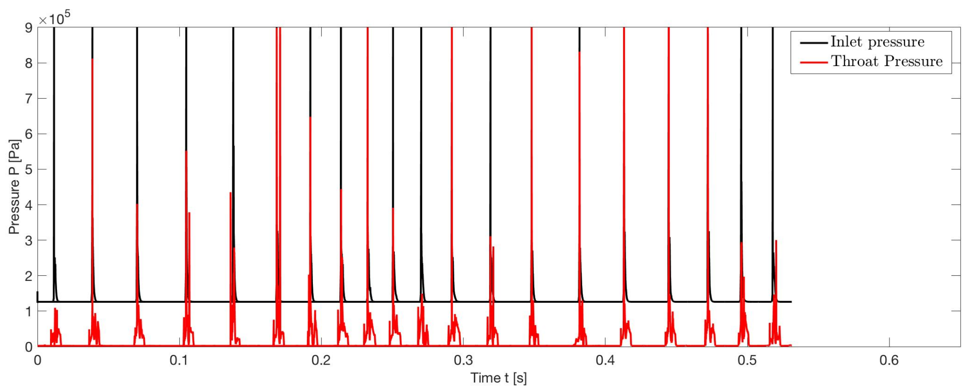

Figure 5.12: Comparison of pressure signals recorded at inlet of the venturi (red) and in the diverging nozzle (black) during a time T = 0.5s. Signals taken from the simulation with lvl_2 grid and recorded at every time time step $\Delta_t = 1 \cdot 10^{-6} s$.

Results are presented in Figure 5.12. Both pressure signals have different peaks over time. All peaks from both signals occur at the same time, which is logical because the model used for this CFD computation is incompressible, meaning there cannot be a wave of pressure propagating at sound speed. The pressure wave is instantaneous.

In Figure 5.13, X-t diagram is plotted both for the liquid fraction (left) but also for the pressure (right) in order to visualise when do the pressure peak occur. On both figures, the triangular shapes can be well observed. The shape has the liquid fraction which varies between $0 < \gamma < 0.4$ and the pressure which is equal to the vapor pressure. Sometimes a slight increase in pressure can be observed at the beginning of the shedding process, when the cavity length is at its maximum. But the pressure peaks which were shown in Figure 5.12 appear at the end of the shedding process, when the cavity is fully detached. Thus, this pressure peaks seem to be numerical artifact which don't have any physical meaning. Still, since these peaks occur at the end of each shedding process, they can be useful to determine the average shedding frequency of this study case and thus will be used later on for a spectral analysis.

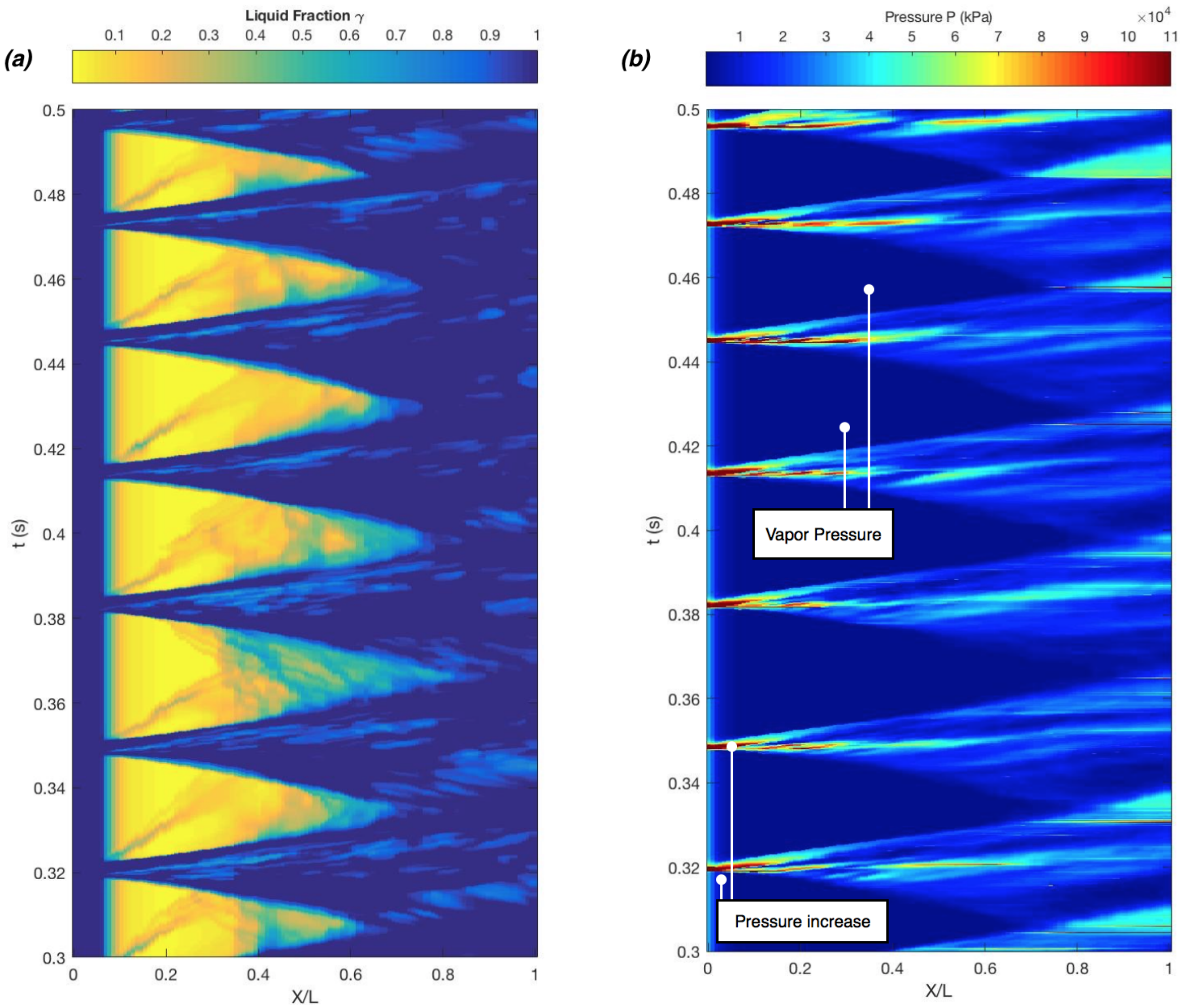

Figure 5.13: Time evolution of the shedding process over a period of 0.5 s; numerical prediction on the lvl_2 grid. Spanwise-averaged quantities are extracted from a parallel plane at a normal distance of n = 2 mm and plotted along the diverging nozzle. (a) is the liquid fraction, (b) is the pressure. Further is $\sigma = 0.40$ ($u_0 = 13.7 m/s$ and $p_{outlet,d}$ = 40 kPa). Sampling frequency $F_s = 1000 kHz$).

5.5.2. Rankine-Hugoniot jump condition [4]

The propagation condensation front can be analysed with the help of Rankine-Hugoniot Jump condition, introduced by Budich et al [4]. These relations can be obtained with the conservation law. For one dimensional flow, the law can be written as :

$$\frac{\delta}{\delta t}\mathbf{U} + \frac{\delta}{\delta x}\mathbf{F}(\mathbf{U}) = 0 \tag{5.3}$$

with the state vector **U** and flux **F**. To support the existence of discontinuities which is caused by the shock front during the shedding process, the Rankine-Hugoniot relations must be satisfied :

$$[\mathbf{F}(\mathbf{U})]_{L,R} = s \cdot [\mathbf{U}]_{L,R} \tag{5.4}$$

s represents the propagation velocity of the discontinuity and $[\cdot]_{L,R} = (\cdot)_L - (\cdot)_R$ with the subscript L denoting the left flow states (pre-shock) and the subscript R denoting the right flow states (post shock). By neglecting bubble dynamics, surface tension and the viscosity, the system can be modeled by the Euler equations with the vectors of conserved quantities and flux given by

$$\begin{bmatrix} \rho u \\ \rho u^2 + p \end{bmatrix}_{L,R} = s \cdot \begin{bmatrix} \rho \\ \rho u \end{bmatrix}_{L,R} \tag{5.5}$$

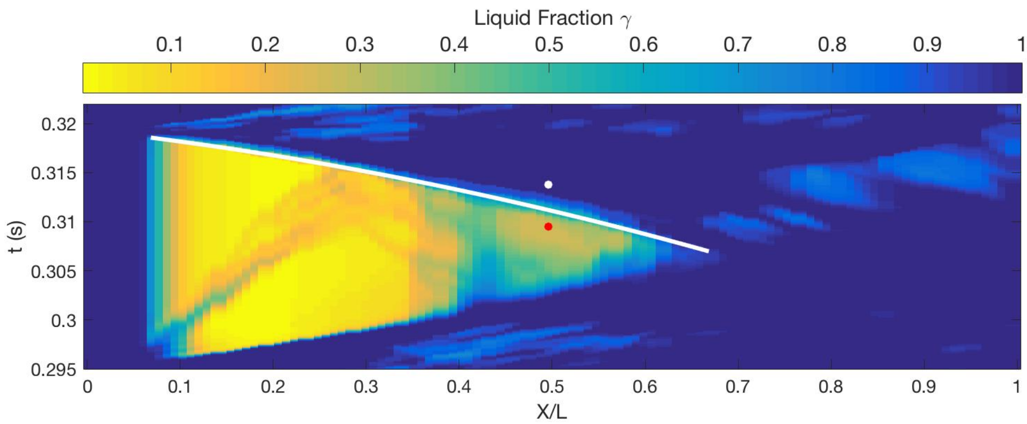

Figure 5.14: Time evolution of the shedding process; numerical prediction on the lvl_2 grid. Spanwise-averaged quantities are extracted from a parallel plane at a normal distance of n = 2 mm and plotted along the diverging nozzle. (a) is the liquid fraction, (b) is the pressure ; Further is $\sigma = 0.40$ ($u_0 = 13.7$ m/s and $p_{outlet,d} = 40$ kPa). Polynomial regression applied for the shock front velocity (white line) .

Table 5.5: Representatively chosen pre- and postshock flow states for Rankine-Hugoniot analysis, extracted from the time instant depicted on Figure. Comparison between quantities in the mid-span slice and the spanwise average

		ρ (kg.m^{-3})	$u_\perp$(m.s^{-1})	p (kPa)	γ (-)
Mid-span slice	preshock	13.01	0.95995	4139	0.01301
	postshock	998.4	-4.763	4139	1
Spanwise average	preshock	269.6	0.6125	2247	0.2703
	postshock	998.4	-4.002	12975	1

Quantities are extracted at discrete locations and for different time instants. One of this case is presented In Figure 5.14. The red dot corresponds to the preshock quantities extracted whereas the white dot corresponds to the postshock quantities extracted. The propagation velocity of the discontinuity s is computed using the first two Rankine-Hugoniot relations, and is compared to the propagation velocity s found by applying a polynomial regression as explained in 5.12. It is found that the discontinuites indeed satisfy the Rankine-Hugoniot jump conditions.

Indeed, a velocity of $s_{midspan}$ = 4.8m/s is found for the mid span slice value and a velocity $s_{averaged}$ = 5.7 m/s for the spanwise average values. The velocity s determined from the polynomial regression was found to be equal to s = 4.9 m/s.

In general, for points taken at different places of the X-t diagram, the difference between the velocity s and the velocity $s_{midspan}$ is in general less than 5 %. The different between the velocity s and the velocity $s_{averaged}$ is around 15 %.Thus, extracting quantities using spanwise average values lead to larger descrepancies for the computation of the Rankine-Hugoniot jump conditions. This can be explained by Figure 5.15. Indeed, the jump applications are only applicable at discrete locations. This won't be the case for spanwise average values. In Figure 5.15, shock fronts of the two different cavities are not at the same place. Thus, the extracted quantities on a same circle won't be the same, and the averaging will increase the errors.

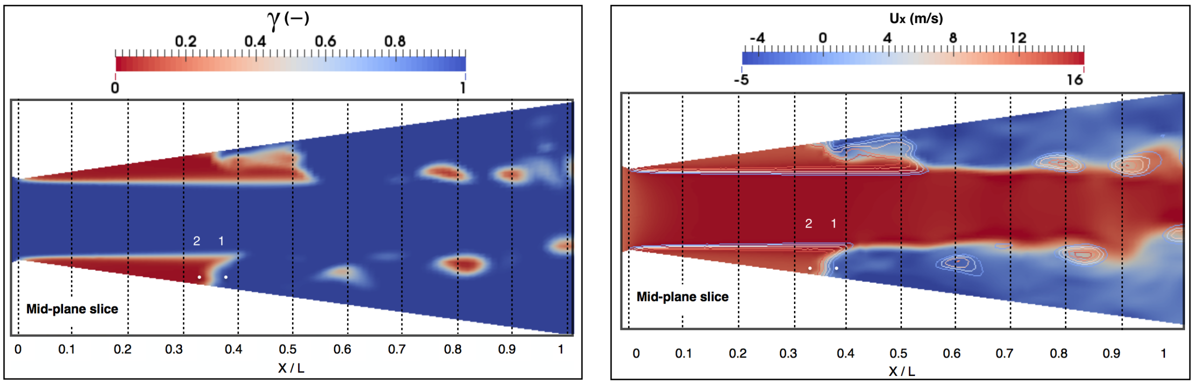

(a) Liquid fraction value.

(b) Horizontal velocity value.

Figure 5.15: Horizontal velocity and liquid fraction values at a discrete time in a mid-span slice of the Venturi

5.6. Shedding frequencies

An important parameter to determine with these computations is the Strouhal number, which indicates the shedding frequency of the system. In order to identify these dominant frequencies and their spatial distribution in the system and to compare them with experimental results, a spectral analysis of signals recorded within the entire divergent nozzle is performed.
As explained in chapter 4, the local axial velocity component u, pressure p and liquid fraction γ were recorded along the bottom wall of the test section by a total of 118 probes, each of this probes representing values averaged in a circle located at a distance of 2 mm from the wall.
The spectra are estimated using Hanning window segments with equal window length in the time domain of 0.25 s and 50 % overlap between subsequent segments, in order to smoothen the broad band distribution in the frequency domain.

The spectral analysis are shown in Figure 5.16. The three plots display the power spectral density PSD of the velocity, pressure and liquid fraction γ, as a function of the streamwise position X/L.
The average sheet cavity extend identified from the X-t diagram presented in Figure 5.6 is indicated by the white dashed lines.

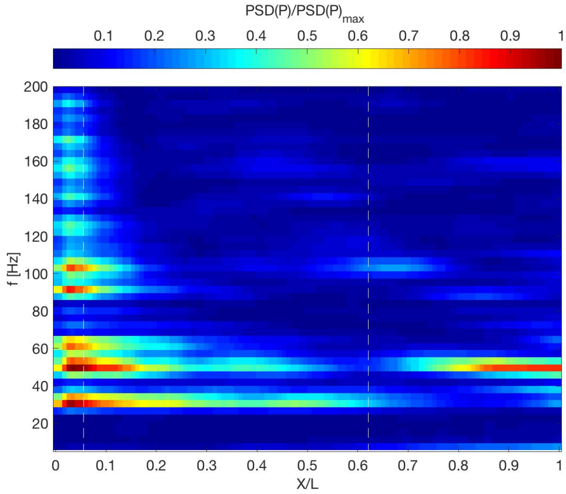

(a) Power spectral density of the pressure p along the diverging nozzle.

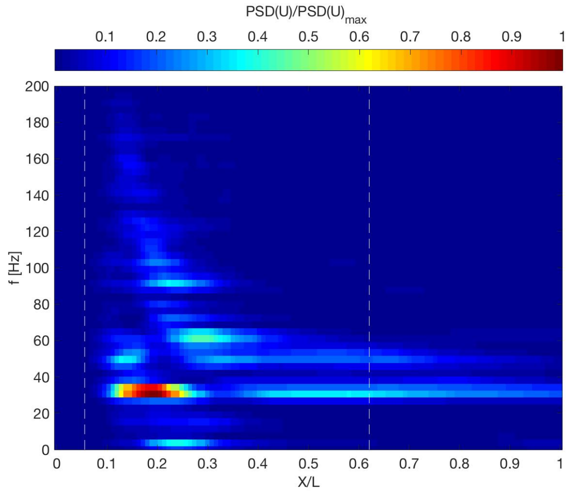

(b) Power spectral density of the velocity u along the diverging nozzle.

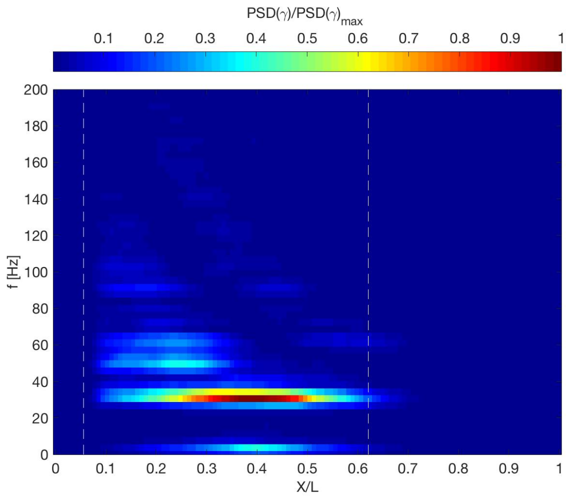

(c) Power spectral density of the liquid fraction γ along the diverging nozzle.

Figure 5.16: Spectral analysis along the diverging nozzle using average values of u,p and γ.

The spectrum for the liquid fraction γ shows a dominant peak well contained between the two dashed lines. The associated frequency is $f = 30.92Hz$. The same value is also found for the pressure p and velocity u. The spectral analysis performed for the pressure is less clear than the two others, as multiple peaks are present at different place of the Venturi nozzle. This is probably due to the fact that the occurrence of peak pressures is a more local effect . The spectrum further shows the existence of harmonics of the shedding frequency. The power spectral density band where is the frequency $f = 30.92Hz$ is located near the Throat of the Venturi, where pressure peak artifacts appear after the shedding process, as it was shown before.
In conclusion, a frequency of f = 30.92Hz was found. The shedding process can be characterised by the Strouhal number which was defined in Chapter 2. In agreement with Hogendoorn [15], this non dimensional number is computed as $St = f d_t / u_0$ with u_0 the velocity at the throat and d_t being the throat diameter. Thus, a value of $St = 0.0373$ is obtained, where the experimentally reported value is $St = 0.0559$.

5.7. Grid and time step refinement study

A grid and time step refinement is performed, following the method presented in Chapter 4.

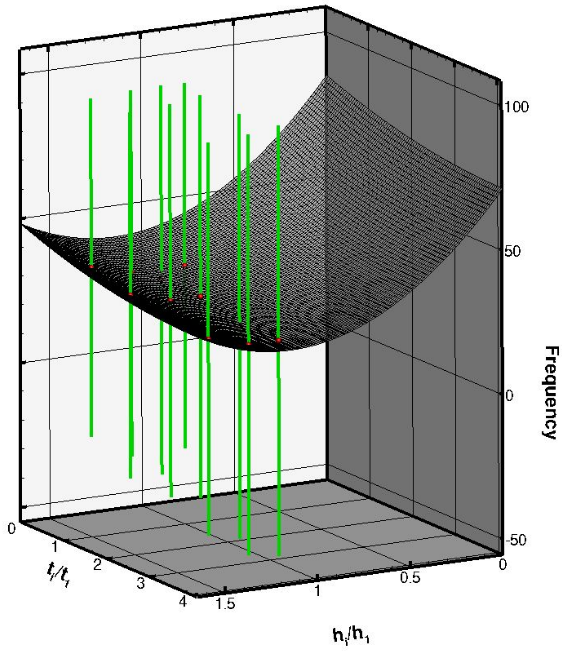

Figure 5.17: Surface fit of the calculated shedding frequency based on the computations presented in Table 5.2. The size of the green segments indicate the uncertainty of each data point (red dot).

The results are implemented in Figure 5.17. The gray surface represents the surface fit of the calculated shedding frequencies. It appears that this surface doesn't show any convergence behaviour towards a constant value when h_i/h and t_i/t decreases. This may be due to the insufficient number of computations performed on different grids at different time step size. The uncertainty of the determination of the shedding frequency may also be too high. Indeed, the broadband of the frequencies presented in Figure 5.16 is too large (around 4 Hz) compared to the difference between the results obtained for different mesh and time step size. Thus, for this test case, the final shedding frequency used for the comparison with experimental results is the one obtained for the computation on the finest grid, for $h_i/h = 1$ and at the finest time step $\Delta t = 1 \cdot 10^{-6} s$. This corresponds to $f = 34.33$Hz.

5.8. Conclusion

In this test case, CFD computations were performed in order to visualise the bubbly shock mechanism, which appears at low cavitation number. After verifying the statistical convergence and the equation of state implemented, the instantaneous flow topology was first studied. The bubbly shock was clearly visualised, causing the formation of a discontinuity named shock front. The shedding process was effectively caused by this phenomenon.

Then the temporal evolution of the shedding process was shown, with the construction of the X-t diagram, which displays the time evolution of the shedding process over a certain period of time and along the diverging nozzle. The typical triangular shapes were found, and the velocities of the growing cavity and of the shock front was found. The Hugoniot-Rankine jump condition [4] was also verified, and the cause of apparition of the shock front was investigated. A pressure shock could be observed right after the shedding process, but it was concluded that it was probably a pressure peak artefact that was already observed in previous study.

Finally in order to compare the experimental results and the CFD computations, the shedding frequency was determined by a spectral analysis in the diverging nozzle area. This results in the computation of a Strouhal number which is compared to the one obtained experimentally at the same flow conditions. This is displayed in Figure 8.3.

It can be concluded that the computation matches with the experiments, as the results are similar.

Thus it appears that an inviscid model is sufficient enough to visualise a bubbly shock phenomenon. The under estimation of the Strouhal number can be explained by the slight overpressure estimation at the inlet of the Venturi, which causes the pressure loss in the nozzle to be more important.
Finally, Figure 5.18 shows a X-t diagram over a period of 0.83 s.

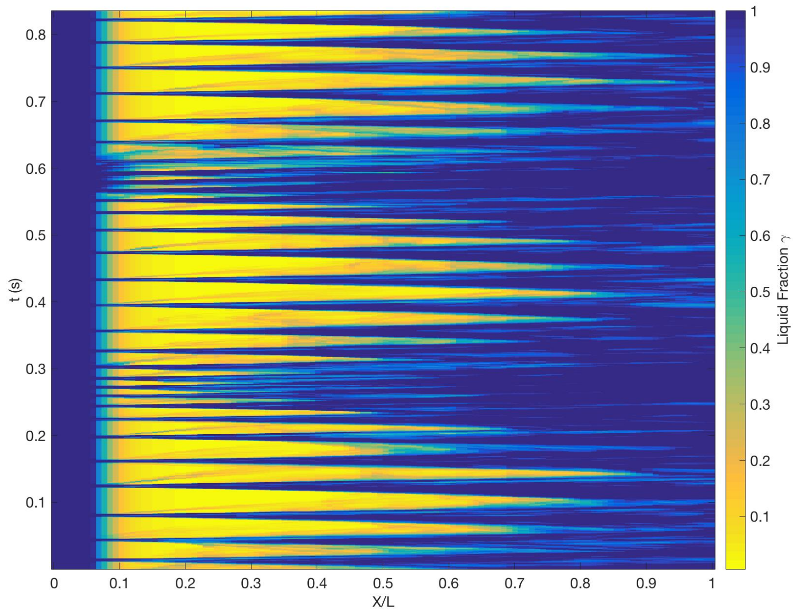

Figure 5.18: Time evolution of the shedding process over a period of 0.83 s; numerical prediction on the lvl_2 grid. Spanwise-averaged quantities are extracted from a parallel plane at a normal distance of n = 2 mm and plotted along the diverging nozzle. Further is σ = 0.40 (u_0 = 13.7 m/s and $p_{outlet,d}$ = 40 kPa). Sampling frequency $F_s = 1000kHz$).

Finally, a X-t diagram is plotted for a longer period of time of t = 0.83. Results are shown in Figure 5.18. A modulation of the shedding frequency can be clearly observed. Indeed, at the beginning of the X-t diagram, the triangular shapes exhibits large lengths and large shedding frequency, but it gradually decreases until a minimal length and shedding frequency is obtained around 0.25 s. Then the triangular shapes start to grow again until they decrease around 0.55 s. This observation was already made by Hogendoorn, but it was seen as an effect of the pump.
This periodical behaviour of the shedding frequency can also be visualised by plotting the average liquid fraction value $\overline{\gamma}$ in the diverging nozzle over time. Results are shown in Figure 5.19 $\overline{\gamma}$ decreases in short interval of times, between 0.2 s and 0.4 s and between 0.5 and 0.7s,. This corresponds to the time in Figure 5.18 of short cavity length and increased frequency of shedding This behavior can be approximated by a sinusoid of frequency 3.7 Hz.

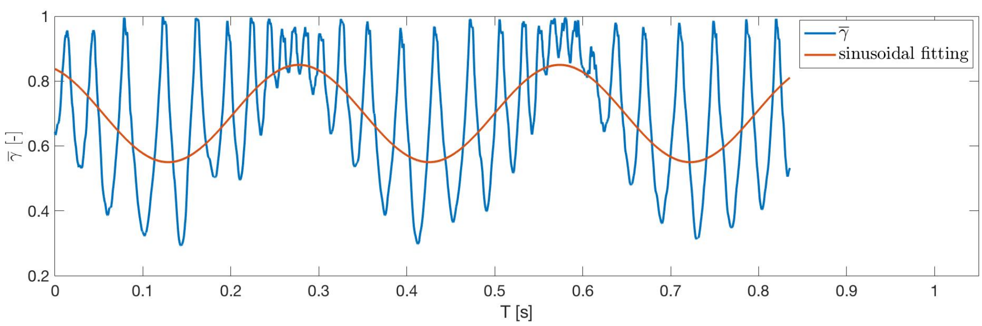

Figure 5.19: Liquid fraction value in the diverging nozzle $\overline{\gamma}$ over time (blue plot) and sinusoidal fitting of the signal (orange plot).

6

Re-entrant jet mechanism

This chapter further examines the results of the CFD computations implemented to visualize the re-entrant jet mechanism and predict the three dimensional characteristics of the unsteady cavitation dynamics. On the contrary of the previous test case, the shedding mechanism is pressure driven instead of shock wave driven. Thus different flow conditions are reproduced in the numerical setup which are once again taken from Hogendoorns' experiments [15]. After verifying the statistical convergence of the computations, results are presented. First the instantaneous flow topology is obtained and the new behaviour of the partial cavities is discussed and compared to the previous test case. The X-t diagram is then presented and the temporal evolution of the shedding process is explained. Its main features are explained, and several parameters like the cavity length and velocity of the re entrant liquid jet is computed. Finally, a comparison between experimental results and results from CFD computations is done, based on the shedding frequency.

6.1. Simulation setup

6.1.1. Boundary conditions

The re-entrant jet mechanism is obtained for a high cavitation number whereas the bubbly shock mechanism was obtained for a low cavitation number of $\sigma = 0.40$. This means that new boundary conditions have to be implemented, such as the velocity at the inlet and pressure at the outlet. The cavitation intensity and thus the average liquid fraction value $\overline{\gamma}$ over the Venturi is expected to decrease.
Figure 4.13 shows the Strouhal - Cavitation number presented in Chapter 2 and the reference point for the implementation of the CFD computations. For this simulation, a high cavitation number is implemented and is totally opposed to the first test case as shown on the graphic. A Strouhal number $St_d = 0.3740$ higher than the one obtained for the bubbly shock test case which was equal to $St_d = 0.0559$. Table 6.1 presents the main parameters of the numerical investigation performed for this study case showed in Figure 4.13.

Table 6.1: Boundary conditions and flow properties for the re-entrant jet mechanism simulation.

Parameters	Value
Fluid	Water
Temperature T $[°C]$	14.5
Outlet Pressure P_{outlet} $[kPa]$	90
Inlet Velocity U $[m.s^{-1}]$	1.48
Liquid Density ρ_l $[kg.m^3]$	999.18
Vapour Density ρ_v $[kg.m^3]$	0.0124
Saturation pressure $[Pa]$	1650
Cavitation number σ $[-]$	1

In order to reproduce the experimental operation point in our computations, both velocity and pressure were taken equal to the values measured during the experiments so they match with the experimental values. In the experiments and simulation, the static outlet pressure at the outlet plane is fixed to a value $p_{outlet,d}$ = 90 kPa. At the inlet plane of the upstream feeding line, a homogeneous inflow velocity 1.48 m/s is specified in order to have a velocity of u_0 = 14.5 m/s at the throat of the Venturi. In total, these changes of boundary conditions give a cavitation number of $\sigma = (p_{outlet,d} - p_{vap}/(\rho u_0^2/2) = 1$, higher than the cavitation number $\sigma = 0.40$ implemented for the bubbly shock test case.

6.1.2. The simulations conducted

Table 6.2 summarizes the simulations conducted, showing the time step, interval used for statistical sampling and the total physical time.

Table 6.2: Overview of simulations conducted for the re-entrant jet test case.

Grid level	Time step Δt (s)	Sampling interval (s)	Physical run time (s)
lvl_0	1×10^{-6}	1×10^{-6}	0.5
lvl_1	1×10^{-6}	1×10^{-6}	0.5
lvl_2	1×10^{-6}	1×10^{-6}	0.5
	2×10^{-6}	2×10^{-6}	0.5
	3×10^{-6}	3×10^{-6}	0.5
	4×10^{-6}	4×10^{-6}	0.5
lvl_3	1×10^{-6}	1×10^{-6}	0.5
	2×10^{-6}	2×10^{-6}	0.5
	3×10^{-6}	3×10^{-6}	0.5
	4×10^{-6}	4×10^{-6}	0.5
lvl_4	1×10^{-6}	1×10^{-6}	0.5
	4×10^{-6}	4×10^{-6}	0.5

Four different grids, denoted as lvl_0, lvl_1, lvl_2 lvl_4, presented in Chapter 4 are used for this computation. For every case, the sampling interval of velocity, density, pressure and liquid fraction is equal to the time step Δt.

6.2. Verification

6.2.1. Statistical convergence

The convergence of our computations are verified using the TST introduced in Chapter 4. For this test case, the same signals than Chapter 5 are chosen : the average liquid fraction value in the divergence nozzle $\overline{\gamma}$ and the liquid fraction value γ_i taken at a discrete location.

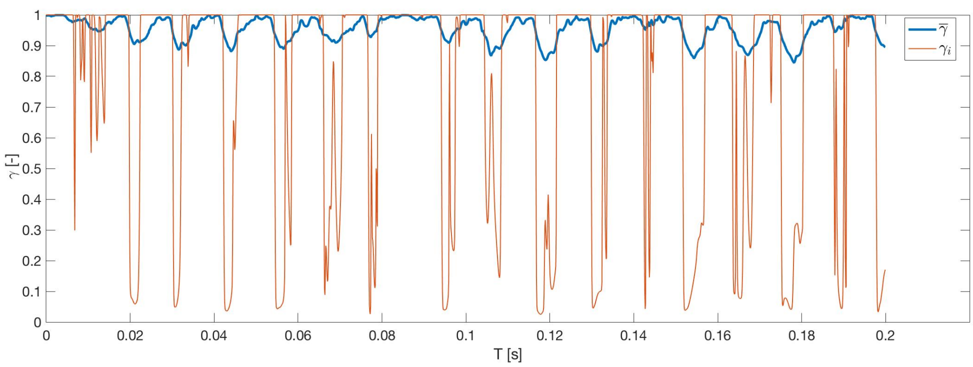

Figure 6.1: Time series of two different signals $\overline{\gamma}$ (blue) and γ_i (orange). Computations performed on the lvl_4 grid at time step $\Delta t = 1 \cdot 10^{-6} s$

Figure 6.1 shows the time series of these two values. Compared to the bubbly shock test case, $\overline{\gamma}$ has higher values and never go below $\overline{\gamma} = 0.9$ which is expected based on the experiments [15].
TST-B is computed for both signals and results are shown in Figure 6.2.

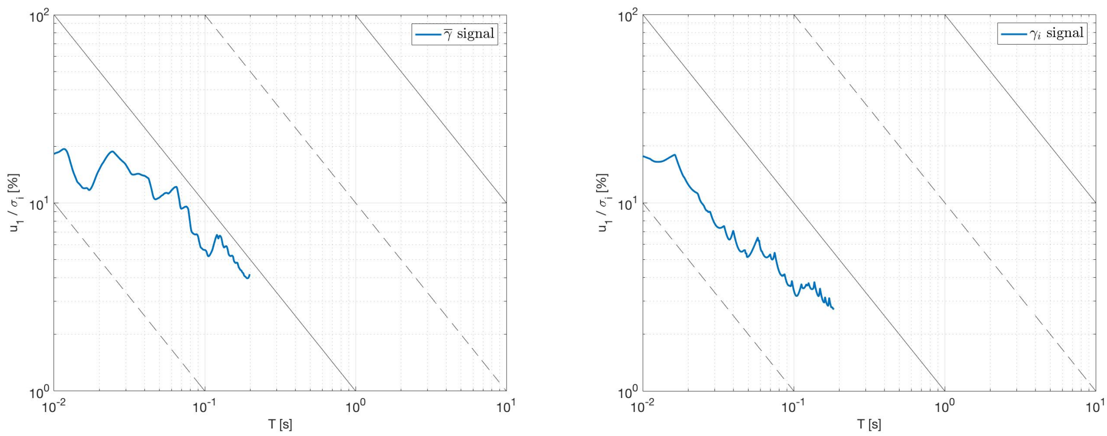

(a) TST-B for $\overline{\gamma}$ signal.

(b) TST-B for γ_i signal.

Figure 6.2: TST-B results for both signals of Figure 7.1, revealing a start up effect for $\overline{\gamma}$ signal. Computations performed lvl_2 grid for a time step of $\Delta t = 1 \cdot 10^{-6}$ s.

Both TST results indicate a stationary region for $0.1s < T < 0.2s$. However, the first TSB-B presented in Figure 6.2a shows a hockey stick indicating a start-up effect is present in the data. Even if it is now very pronounced as the hockey stick appears at $T = 0.195$ s and the increase is not important.
Nonetheless, the hockey stick is removed by erasing 0.05 s more from the beginning, which is approximately its width. Recalculating the TSTs with $t_{begin} = 0.05s$ gives Figure 6.3.

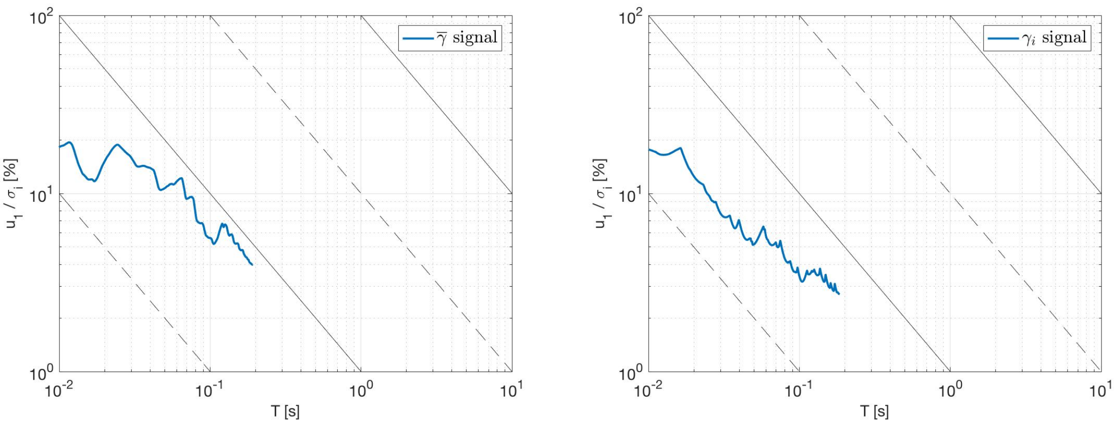

(a) TST-B modified for $\overline{\gamma}$ signal.

(b) TST-B modified for γ_i signal.

Figure 6.3: TST-B results based on the selection after an additional section has been removed at the beginning.

It appears that the hockey stick in Figure 6.3a has been removed from the TST-B plot (as expected) without changing the TST-B plot in Figure 6.3b. Both signals follow a 1/T trend and the stationary region remains the same. The uncertainty is higher for $\overline{\gamma}$ signal as it equal to 4% at the end of the computation, compared to the uncertainty of γ_i signal which is equal to 1.8%.
The final stationary selection is shown in Figure 6.4.

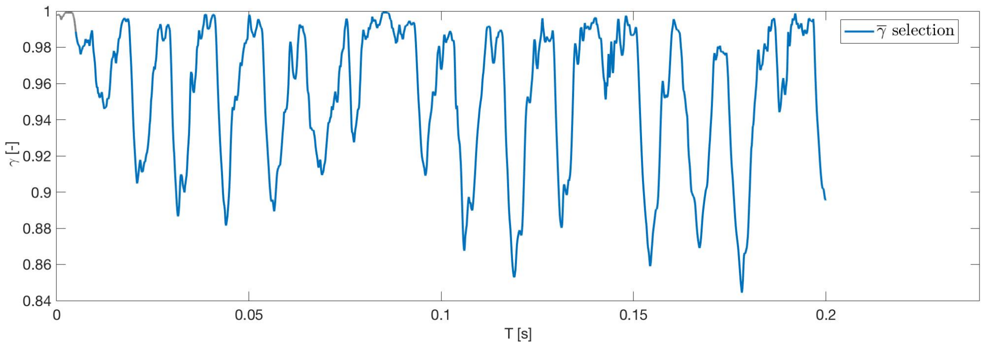

Figure 6.4: Time series of two different signals $\overline{\gamma}$ (blue) and γ_i (orange). Computations performed on the lvl_4 grid at time step $\Delta t = 1 \cdot 10^{-6} s$

Only the $\overline{\gamma}$ signal is shown as there was no start up effect for the γ_i signal. The selection according to the TST selection is really close to the raw signal as only 2% of the signal is cut off.
The TST analysis is done for every computations presented in Table 6.2 and shows the same behaviour.

6.2.2. Flow properties and pressure loss

Simulations presented in Table 6.2 are carried out and the pressure loss at the venturi is computed. Table 6.3 presents the pressure computed and sampled at the inlet and outlet of the venturi and the experimental reference.

Table 6.3: Flow properties up and downstream of the venturi ; Comparison between numerical results on grid ,$lvl_2$and the experimental reference

$P_{inlet,exp}$ (Pa)	$P_{inlet,sim}$ (Pa)	$P_{outlet,exp}$ (Pa)	$P_{outlet,sim}$ (Pa)	K_{exp} (-)	K_{sim} (-)
100278	139109	80580	88522	0.223	0.572

The pressure loss K obtained numerically can also be observed in Figure 8.1 in Chapter 8. Just like the bubbly shock test case, an overestimation of the pressure loss is predicted by the simulation compared to the experiments. The main difference is the error gap. Indeed, for test case 1, the pressure loss was overpredicted by 11%, whereas the estimation for test case 2 is biased by around 63%. The main reason is the overestimation of the pressure at the inlet, with a difference of nearly 30 %. This overestimation remains constant when the mesh and time step, meaning it can not be avoided. Figure 8.1 shows that the difference between the experiments and the computation is important. Indeed, for the experiments, a pressure loss of $K = 0.572$ corresponds more to flow conditions giving $\sigma = 0.75$. The consequences of this overestimation is presented in the next sections where values such as cavity lengths and shedding frequency are computed.

6.3. Instantaneous flow topology

To compare the behavior of the partial cavities in the experiments and in the computations, instantaneous snapshots of the simulations are first presented and compared to the results of Hogendoorn [15]. Figure 6.6 presents several pictures from the inside of the diverging nozzle during the simulations computed for the lvl_2 grid. Cavitation is represented by several isosurfaces of different opacities for different values of γ. The same setting presented in Table 5.4 of Chapter 5 are implemented for this test case.
Fourteen representative time instants were selected in Figure 6.6 (a)-(l), exhibiting the growth and progressive shedding of the cavity caused by the re-entrant jet mechanism for a total time of 6.6 ms.
Figure 6.6(a) presents the beginning of the formation of the cavity inside the diverging nozzle, which appears the throat of the Venturi. Compared to the bubbly shock test case presented in chapter 5, not a lot of cavitation inside the diverging nozzle can be observed. This matches the time series of $\overline{\gamma}$ presented in Figure 6.1. This is due to the high cavitation number $\sigma = 0.98$ implemented for this computation. Small cavitating structures can be found being advected by the flow at the beginning in Figure 6.6(a)-(b). The cavity can be seen at $t = t_0$ partially detached.
From figure $t = t_0$ to $t = t_0 + 3$ms, the cavity continues to grow along the Venturi. It is in Figure 6.6(d) that a

re-entrant jet starts to develop. This development proceeds from $t = t_0 + 3.3$ms to $t = t_0 + 3.9$ms, where the re-entrant jet moves in the opposite direction of the Venturi. The propagation of the jet can be seen by the chaotic interface.
The detachment of the cavity occurs in Figure 6.6(g) where it is pinched off from the wall.
Finally, the detached cavities shown in Figure 6.6(k)-(l) are advected by the flow and travel through the diverging nozzle. Vortical structures can be observed, due to the condition of the flow and the pinch off which caused the detachment of the cavity.

The shedding process can also be visualised by taking a mid plane slice. For this purpose, figure 6.7 shows a series of six consecutive time instants in the form of the instantaneous liquid fraction γ, horizontal velocity U_x and pressure p in the diverging nozzle. All these values were taken in a mid-plane slice. In order to relate the fields of velocity and pressure to the occurrence of cavitation, isocontours of γ were included in (b) and (c). Figure 6.7 starts with a grown cavity at $t = t_0$. There is a partial detachment of the cavity which is already observed in figure 6.6. It appears this partial detachment is caused by a pre-re entrant liquid jet which travels below the cavity during its growth. Indeed, a slight negative velocity of around 1 m/s is observed at $t = t_0$ below the cavity and reached the end of the partial detached cavity. This pre-re entrant jet is not strong enough to cause the pinch off of the cavity. A strong pressure gradient can be observed in Figure 6.7-(c), with the cavity being at the vapor pressure of $p_{vap} = 1650Pa$ and the rest of the diverging nozzle at a pressure which is more than $p = 80$ kPa.
Then, the re-entrant jet can be first observed at $t = t_0 + 6$ms. A strong decrease of the velocity from $u = -1$m/s to $u = -6$m/s is observed at the stagnation point at the end of the partial cavity, causing the apparition of a counter flow which starts to travel below the partial cavity. From $t = t_0 + 6$ms to $t = t_0 + 1.8$ms, the jet front moves upstream with the propagation of the negative velocity. The pressure gradient stays the same and the partial cavity stops growing, with its length remaining constant. Moreover, the cavity interface can be seen deformed by a a traveling wave style deformation, matching the experimental observation made by Stanley et al (2014) [37]
At $t = t_0 + 2,4ms$, the liquid re-entrant jet has reached the beginning of the partial detached cavity and pinch it off, causing its detachment. The backside of the cavity (upstream) sticks to the Venturi throat and is progressively detached by the re-entrant jet liquid. This complete detachment occurs at $t = t_0 + 3.6$ms. For the bubbly shock test case presented in chapter 5, the shedding mechanism was slower in time, taking approximately 22 ms from the beginning of the shedding to the complete detachment of the cavity. Here, it only takes 3.6 ms. This explains the higher values obtained for the Strouhal number when dealing with the re entrant jet mechanism.
Moreover, just after the detachment of the cavity, cavitating vortices structures are observed, due to the difference of velocity below and above those structures. This is shown on Figure 6.6 at $t = t_0 + 3.6$ms with the black arrow indicating the negative velocity due to the re entrant liquid jet and the white arrow due to the velocity of the flow in the diverging nozzle.
This difference of velocity at the boundary of the cloud cavity cause its progressive rotation from $t = t_0$+3.6 ms to $t_0 + 5.1$ms. These structures are also advected by the flow and progress further along the geometry. These vorticities were also observed during the experimentations of the re-entrant jet by Hogendoorn [15]. They are visible in Figure 6.5. This so-called generation of a horseshoe vortex is associated with the collapse of the the cavity and is a very frequent phenomenon in cavitating flows and is found in other numerical simulations (e;g in a simulation towards cavitation on the twisted Delft hydrofoil by Ji et al).

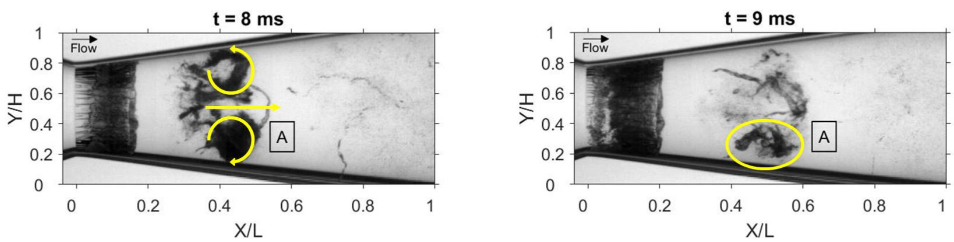

Figure 6.5: Video frames of a cavity growth event in the venturi. Cavitating vortices can be observed being advected by the flow. Experimental results taken from Hogendoorn [15] for a cavitation number $\sigma = 1$.

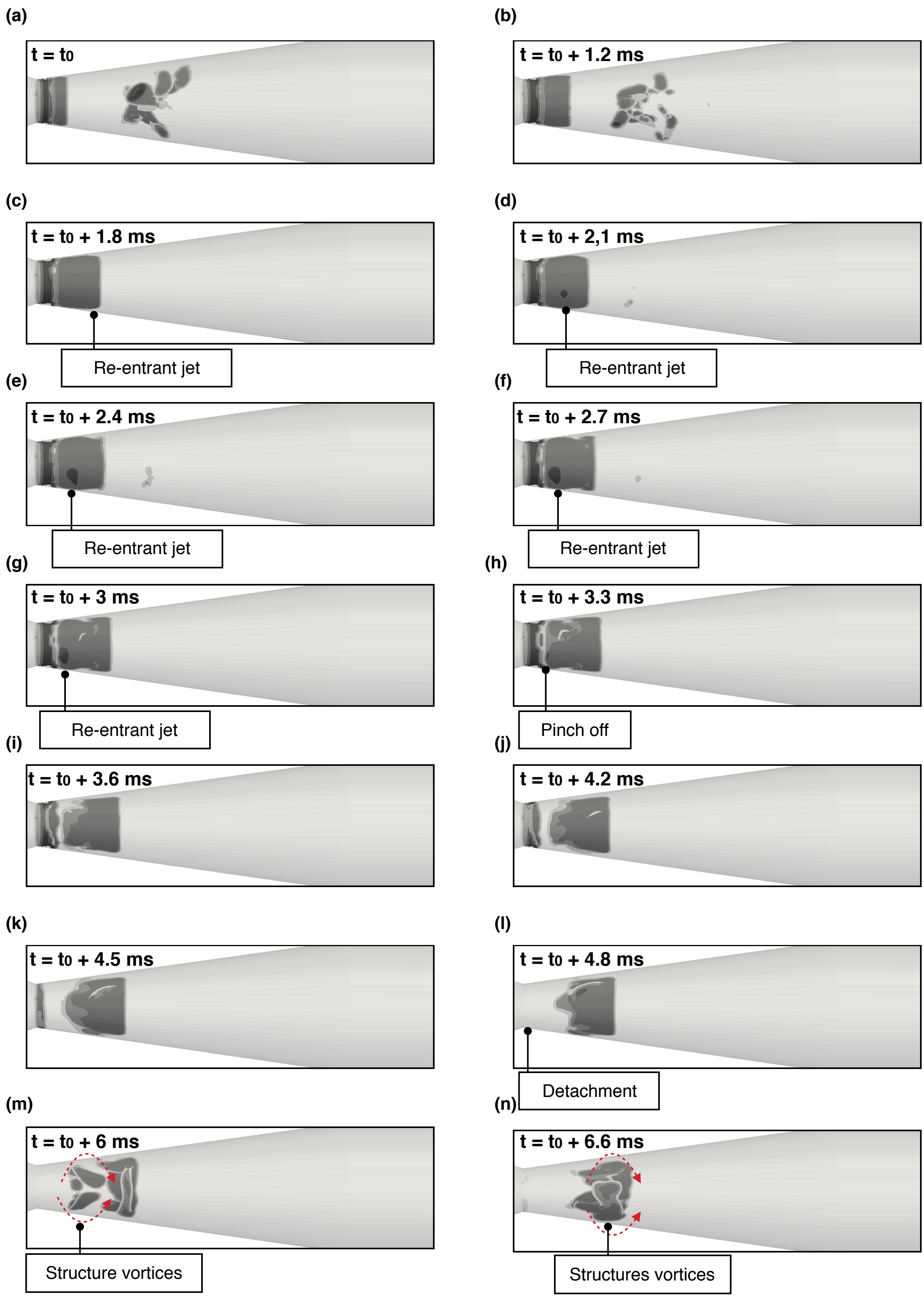

Figure 6.6: Illustration of a typical shedding cycle dominated by the re-entrant jet mechanism (side view). Numerical results show vapor structures with different isosurfaces for different opacity. Simulation performed on the lvl_2 grid for $\Delta t = 1 \cdot 10^{-6} s$.

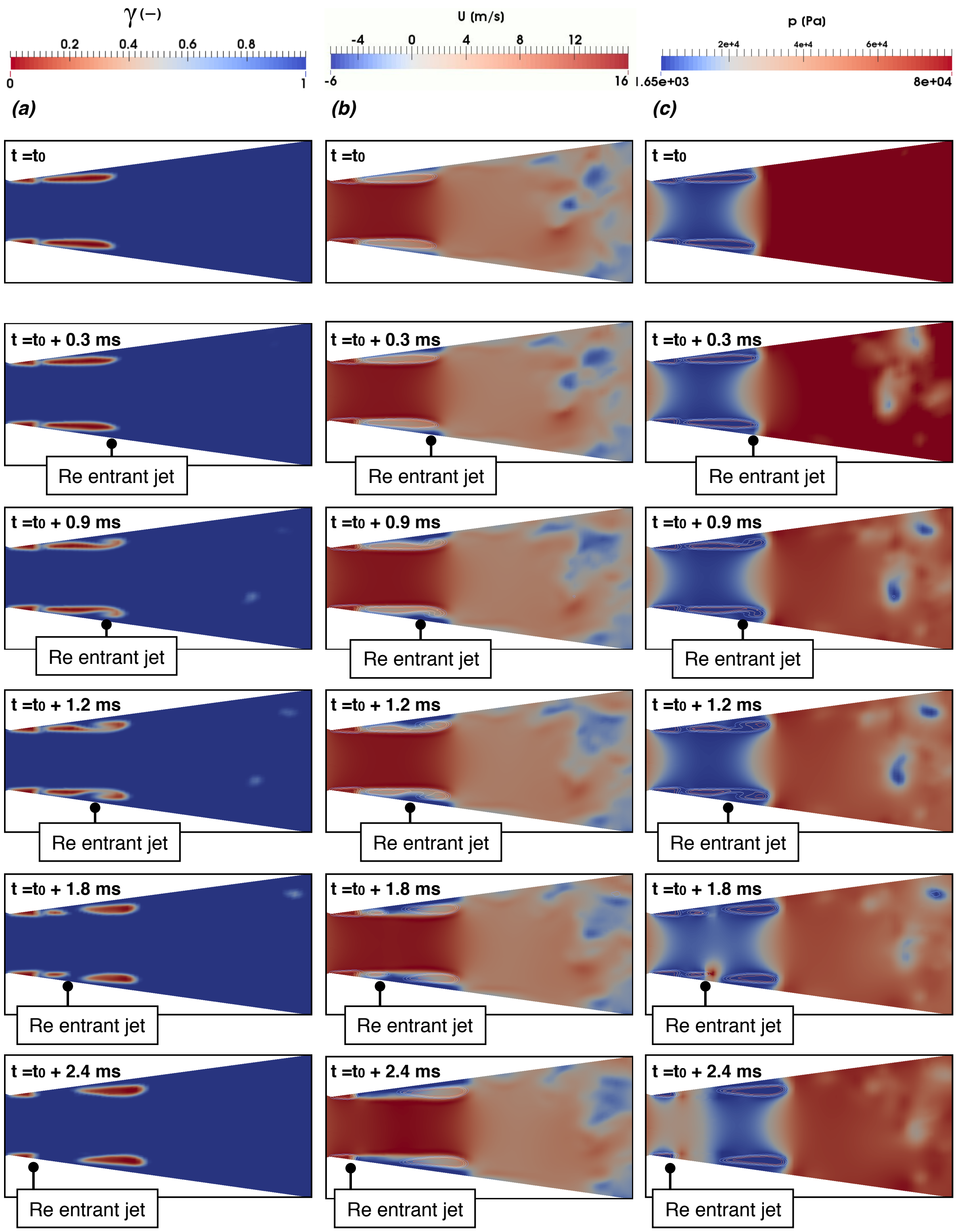
γ (–)
0.2 0.4 0.6 0.8
0 1
U (m/s)
-4 0 4 8 12
-6 16
p (Pa)
2e+4 4e+4 6e+4
1.65e+03 8e+04
(a)
(b)
(c)
t =t0
t =t0 + 0.3 ms
t =t0 + 0.9 ms
t =t0 + 1.2 ms
t =t0 + 1.8 ms
t =t0 + 2.4 ms
Re entrant jet

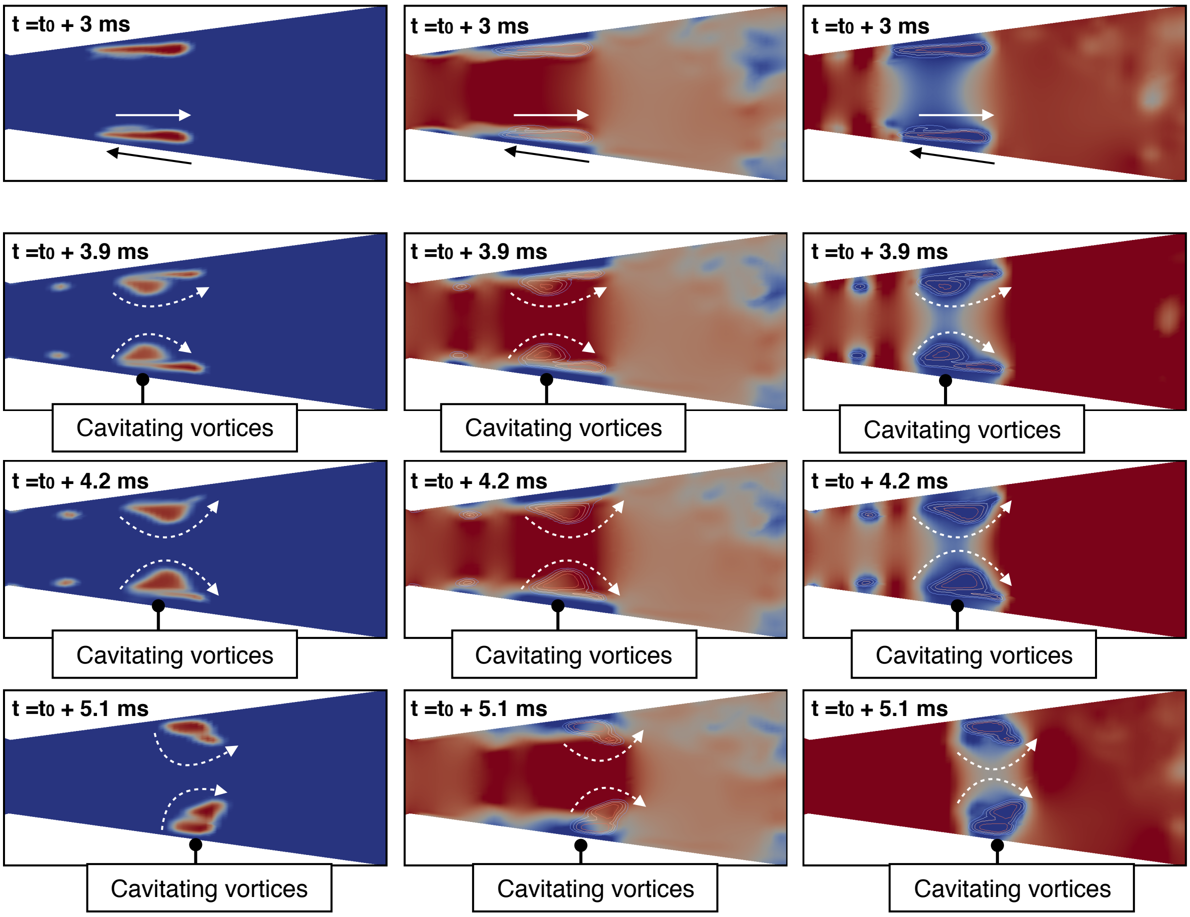

Figure 6.7: Instantaneous flow field captured in a mid-plane slice during a re-entrant dominated shedding cycle for ten consecutive time instants. Numerical prediction on the grid. Comparison between (a) liquid fraction γ, (b)streamwise velocity U, and (c) pressure p.

The instantaneous flow topology seem to match the experiments. Indeed, the same shedding mechanism is obtained for similar setups, with the presence of a re-entrant liquid flow below the cavity responsible of the pinch off of the cavity. The presence of vorticing structures is also found, and differences with the bubbly shock test case in terms of cavity length, and shedding time is observed.

Now, in order to compare more accurately the computations and the experiments, the temporal evolution of the shedding process is studied, thanks to X-t diagrams.

6.4. Temporal evolution of the shedding process

6.4.1. X-T diagram

The shedding process across multiple cycles can be further analysed by constructing the X-t diagram for this test case. The same probing plane at n_p = 2 mm from the wall used in the first test case is introduced for this study. A total time of t = 0.2 ms is chosen. Indeed, as it can be observed with the instantaneous flow topology, the shedding frequency is much more important for the re-entrant jet mechanism test case. Results are shown in Figure 6.8.

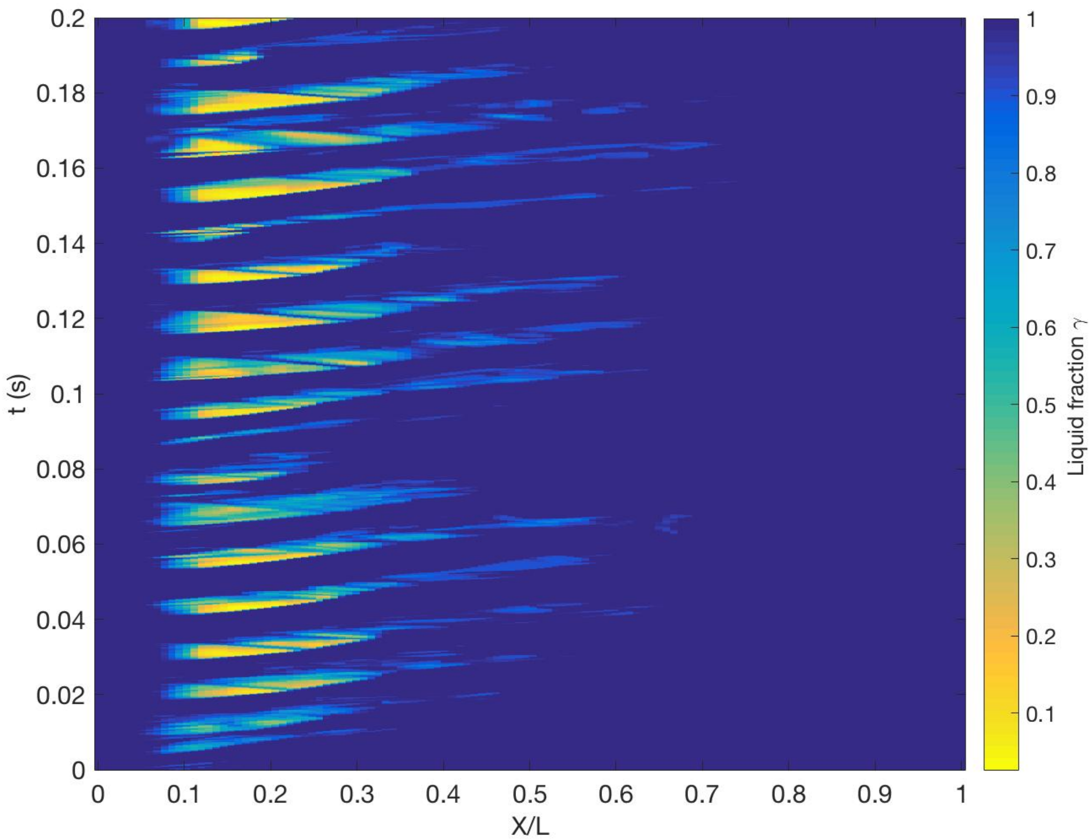

Figure 6.8: Time evolution of the shedding process over a period of 0.2 s; numerical prediction on the lvl_4 grid. Spanwise-averaged quantities are extracted from a parallel plane at a normal distance of n = 2 mm and plotted along the diverging nozzle. Further is σ = 1 (u_0 = 14.5m/s and $p_{outlet,d}$ = 90 kPa). Sampling frequency F_s = 1000kHz) .

Compared to the results obtained for the first test case and visible in Figure 5.6, the X-t diagram for the test case 2 is quite different. First, no more triangular shapes are visible, replaced by a more typical stick-slip shape shape, which was already observed by Hogendoorn [15] and is related to the re-entrant jet induced shedding. The length of the shapes are smaller compared to the triangular shapes obtained for the bubbly shock. It appears that if some shapes are distinct and recognisable of a re entrant jet mechanism, for example between t = 0.02 s and t = 0.06s, soma appear blurry, as it can be observed around t = 0.1s. This can be due to the too large distance used for the probing of the data. By using a plane situated between 0.05 mm and 0.1 mm, the re-entrant jet thickness would have been more visualised. Nonetheless, it was decided to keep this distance constant for all case studies in order to compute the results, for example the shedding frequency, with the same methods. A total of 18 shapes are obtained with this diagram.

The shapes are more visible when using the pressure, because inside the partial cavities, the pressure is equal to the vapor pressure whereas the rest of the flow has a more important pressure. Some instant pressure shock can be observed during the shedding process, maybe due to the collapse of some bubbles, or because of numerical artifacts, as it was the case for the bubbly shock mechanism.

Figure 6.9 is plotted in order to visualize more the stick-slip shape :

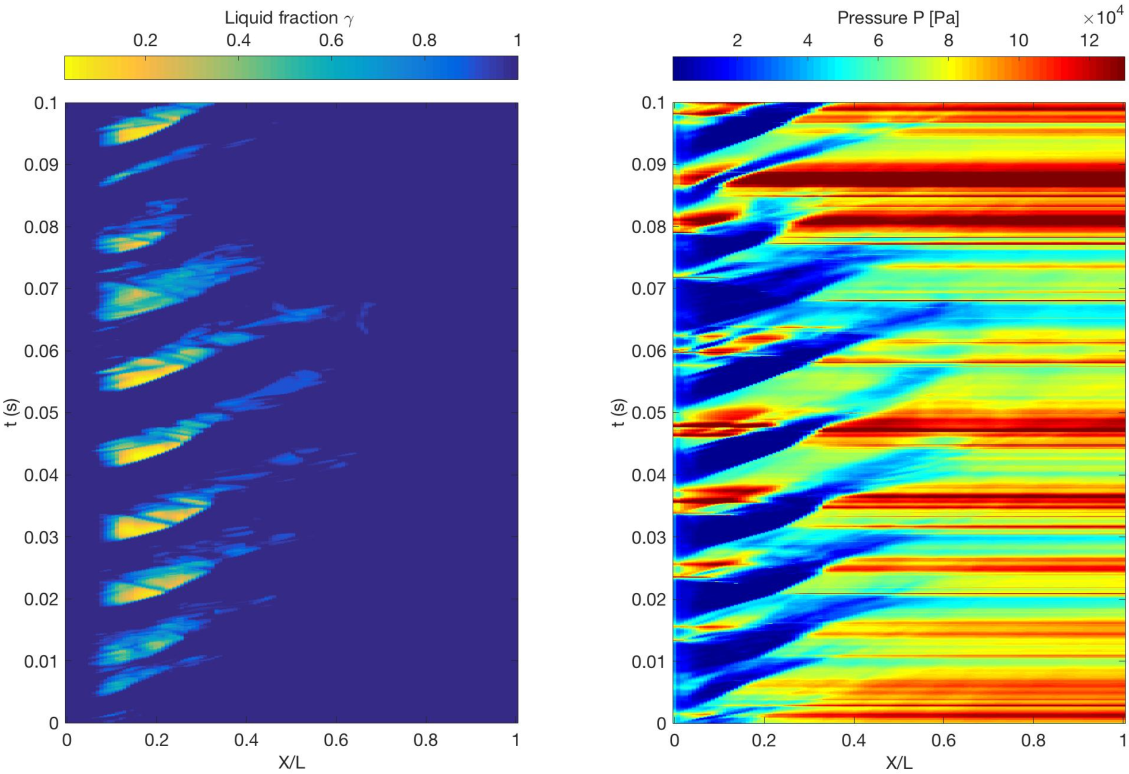

(a) X-t diagram using liquid fraction γ.

(b) X-t diagram using pressure p.

Figure 6.9: Time evolution of the shedding process over a period of 0.2 s; numerical prediction on the lvl_4 grid, based on the liquid fraction γ (left) and pressure p (right). Further is $\sigma = 1$ (u_0 = 14.5 m/s and $p_{outlet,d}$ = 90 kPa). Sampling frequency $F_s = 1000kHz$).

Due to the strong pressure gradient present in the flow, the shapes in X-t diagram of the pressure along the diverging nozzle are clearer, and the shedding of the cavities can be visualised, which is not the case for the X-t diagram based on the liquid fraction.

The diagram obtained for these simulations and the one obtained during the experiments [15] are presented in Figure 6.10. For Figure 6.10a, the pressure is chosen because of the more distinct shapes observable. In Figure 6.10b, the light gray regions indicate the presence of liquid. A typical shedding cycle is captured with a rectangular bow and enlarged on the right side of both diagrams. In Figure 6.10b the cavity starts to grow at $t = 20ms$ and at $t = 0.36ms$ for Figure 6.10a. For both diagrams, the growth is clear until a certain point, where the slope becomes steeper, which indicates that the cavity front growth rate decreases. During this front velocity decrease, cavity detachment can be observed at $t = 24ms$ for Figure 6.10b, and at $t = 0.42ms$ for Figure 6.10a. Back side of the cavity moves near instantaneously from $X/L = 0$ to $X/L = 0.04$. This detachment is caused by the pressure gradient introduced during the study of the instantaneous flow topology. The vapor cloud can be observed being advected with a positive velocity. This cavity front velocity increases to a constant velocity, visible with the constant slope. This is why this behavior is called a " stick slip" behavior, which is typical for the examined regime. As explained above, the instantaneous pressure peak observed all along the Venturi which occurs during the advection of these partial cavities can be explained by the collapse of the vortices structures introduced in Figure 6.5.
For a stick slip behavior, the backside or upstream part of the cavity sticks to the Venturi throat and suddenly detaches at a certain point, associated with slip.

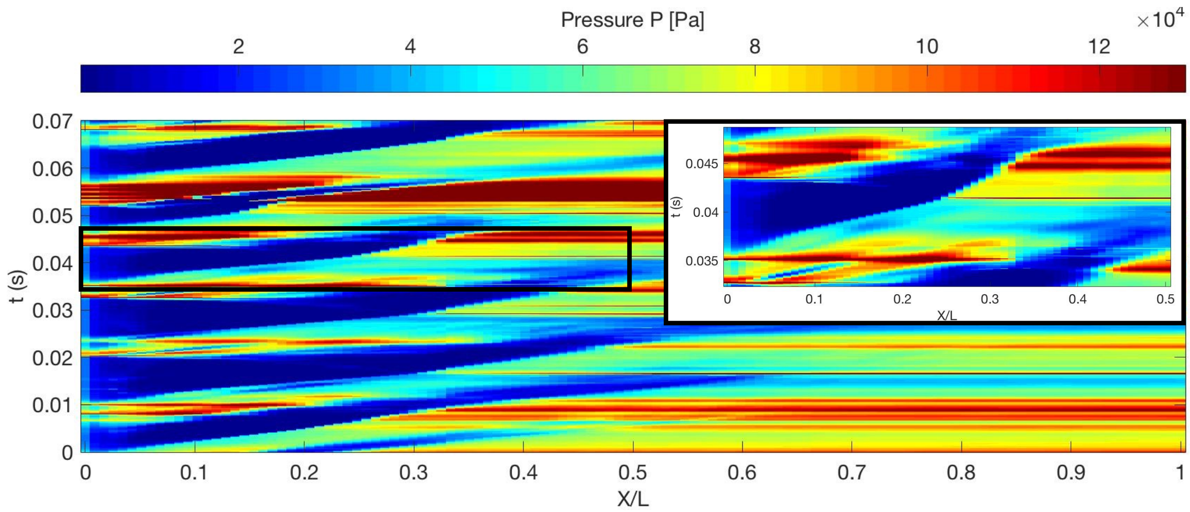

(a) X-t Diagram using liquid fraction γ.

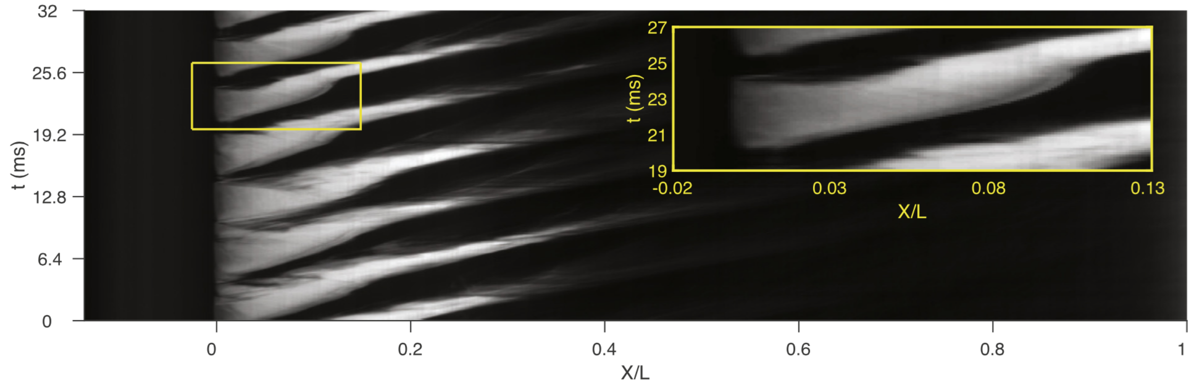

(b) X-t Diagram using pressure p.

Figure 6.10: Time evolution of the shedding process over a period of 0.2 s; numerical prediction on the lvl_2 grid. Spanwise-averaged quantities are extracted from a parallel plane at a normal distance of n = 2 mm and plotted along the diverging nozzle. Further is $\sigma = 0.98$ ($u_0 = 14.5$m/s and $p_{outlet,d} = 90$ kPa). Sampling frequency $F_s = 1000kHz$).

Cavity length The shedding of the vapor cavity can be observed using the X-t diagram for the pressure, as it is shown in Figure 6.10 and 6.9. Thus, the maximum cavity length can be computed and compared to the experimental results.
The length is obtained for every stick-slip shapes and averaged in order to obtain a mean length value of $\bar{l} = 35$mm . For the same flow conditions Hogendoorn obtained a cavity length of $l = 16.0$mm [15]. Results are plotted in Figure 8.2 and can be visible in Chapter 8. This overestimation can directly be linked to the overestimation of the pressure introduced earlier in Figure 8.1.

Velocity of the cavity and of the re-entrant liquid jet Figure 6.11 can also be plotted to visualise more in detail the re-entrant jet velocity.
For the more visible stick-slip shape, an negative velocity of the order of the velocity reaching the throat can be observed. It corresponds to the re-entrant jet velocity which travels from downstream to upstream. It is roughly constant over time.

For the less visible re-entrant jet shedding process between $t = 0.07$s and $t = 0.1$ s, no negative velocities are observed. This is also due to the fact that the probing plane must be too far from the re-entrant jet area to capture the velocity of the re-entrant front or because the grid for this test case is not refined enough.
Typical velocity of 1 - 3 m/s are found based on Figure 6.11 for a mean flow velocity of 14.5 m/s at the venturi throat. This matches perfectly with the experimental results of Hogendoorn [15], where velocities of 1.1 - 3.4 m/s were found for mean flow velocities of 14.4-14.8 m/s. This means the overestimation of the pressure doesn't have any effect on the re-entrant jet velocity.

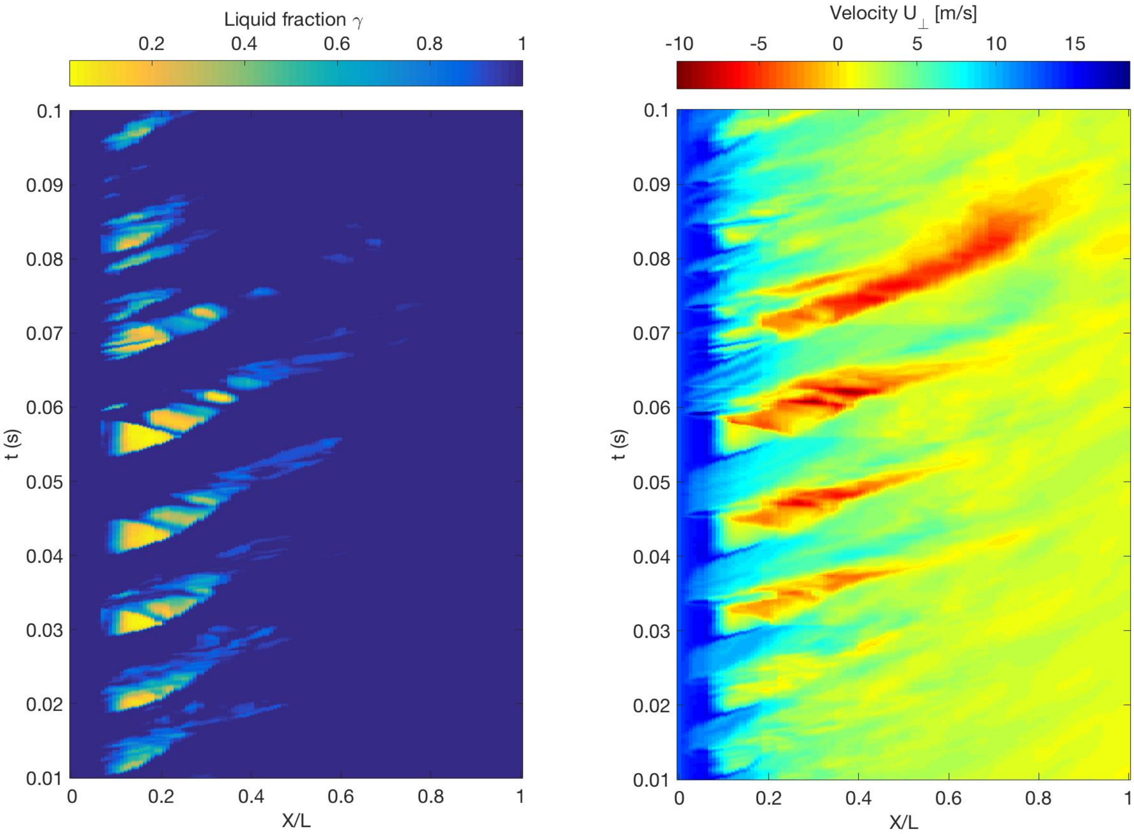

(a) X-t Diagram using liquid fraction γ.

(b) X-t Diagram using velocity u.

Figure 6.11: Time Evolution of the shedding process over a period of 0.2 s; numerical prediction on the lvl_2 grid. Spanwise-averaged quantities are extracted from a parallel plane at a normal distance of n = 2 mm and plotted along the Diverging nozzle. Further is $\sigma = 1$ ($u_0 = 14.5 m/s$ and $p_{outlet,d} = 90$ kPa). Sampling frequency $F_s = 1000 kHz$).

6.5. Shedding frequencies

The same spectral analysis done of Chapter 5 is done for this test case.

The spectral analysis are shown in Figure 6.12. The three plots display the power spectral density PSD of the velocity u, pressure p and liquid fraction γ as a function of the streamwise position X/L.

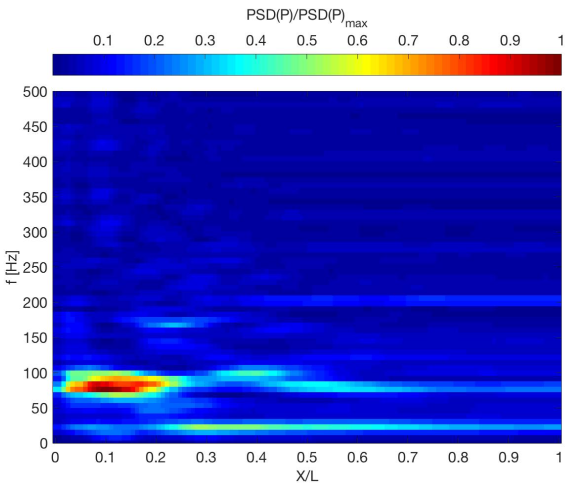

(a) Power spectral density of the pressure p along the diverging nozzle.

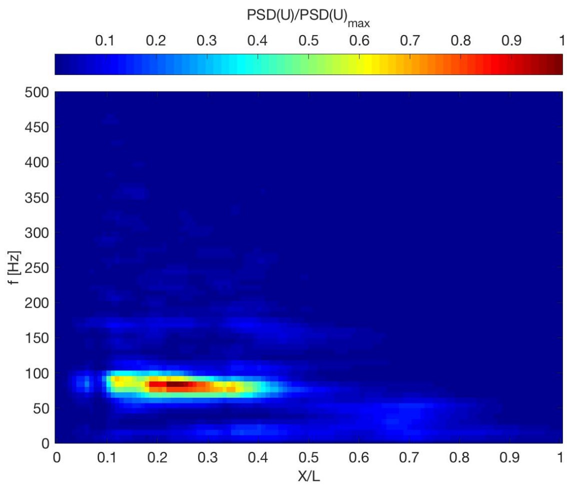

(b) Power spectral density of the velocity u along the diverging nozzle.

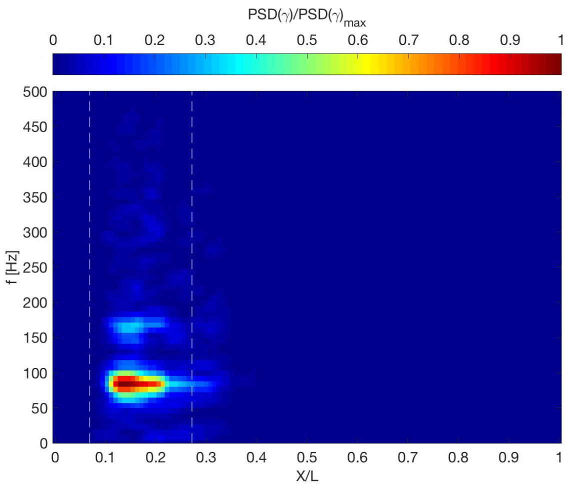

(c) Power spectral density of the liquid fraction γ along the diverging nozzle.

Figure 6.12: Spectral analysis along the diverging nozzle using average values of u,p and γ for the re-entrant jet test case.

Compared to the test case 1, the power spectral density plots exposed in Figure 6.12 all exhibit the same behaviour. The peaks are found near the beginning of the diverging nozzle due to the small cavity length of the partial cavities. A shedding frequency of $f = 83.92 Hz$ is found.
In agreement with Hogendoorn [15], this non dimensional number is computed as $St = f d_t / u_0$ with u_0 the velocity at the throat and d_t being the throat diameter. Thus, a value of $St = 0.1051$ is obtained, where the experimentally reported value is $St = 0.3696$. If the Strouhal number found for this study case is larger than the one obtained for the bubbly shock test case, the difference between the experiments and the computations is very important.

6.6. Grid and time convergence study

A grid and time step refinement study is performed for the re-entrant jet test case, based on the shedding frequency obtained for each computations referenced in Table 6.2. Results are shown in Figure 6.13.

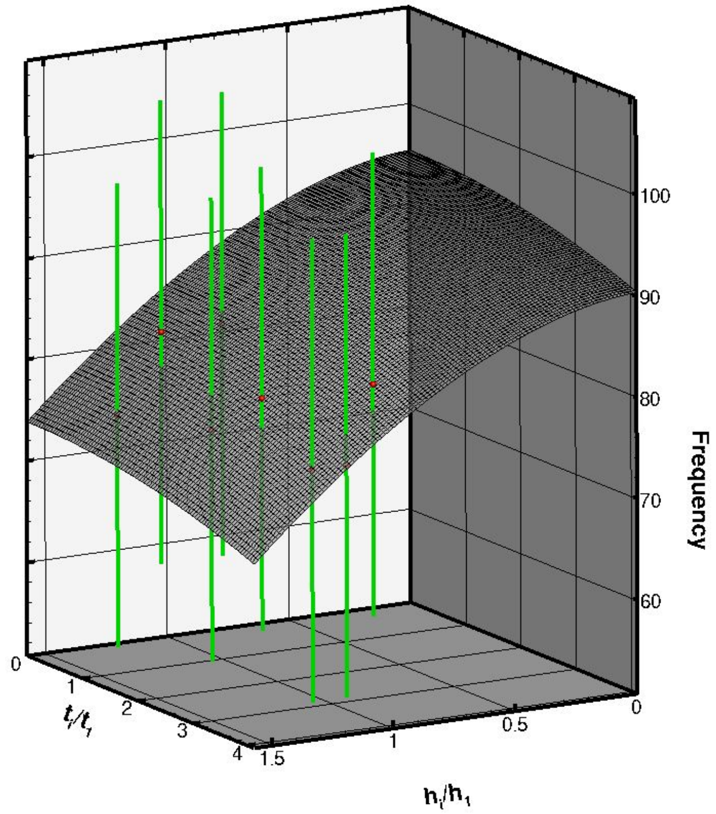

Figure 6.13: Surface fit of the calculated shedding frequency based on the computations presented in Table 6.2. The size of the green segments indicate the uncertainty of each data point (red dot).

It appears that, on the contrary of the bubbly shock case, the re-entrant jet test case converges around a value of 95 Hz. The uncertainties for each data point is pretty high due to the insufficient number of computations performed. More simulations were tested for coarser grid like lvl_0 and lvl_1 grid, but due to the sensibility of the re-entrant jet mechanism, the computations diverged.

6.7. Modified test case

The results obtained by the numerical test case matches with the experimental results when comparing the behaviour and instantaneous topology of the partial cavities. The only major difference lies in the shedding frequency, which is not well estimated on the computations. It appears the difference between shedding frequency is not because of a lower re-entrant jet velocity of another shedding mechanism, but because of the overestimation of the pressure loss. Indeed, it appears that the drastic increase in the inlet pressure modifies the advected flow and move the stagnation point responsible of the re-entrant jet velocity up the diverging nozzle. This leads to a larger cavity length as observed in Figure 8.2, which takes larger time to shed and thus lowering the shedding frequency.
Another assumption made is that due to the steepness of the strouhal-cavitation number plot for the re-entrant jet regime, a slight change in the flow conditions drastically modify the shedding frequency value. Thus, another test case is implemented. The parameters of this computation is presented in Table 6.4.

The only difference between this test case and the original re-entrant jet test case is the increase of 10 kPa of the outlet pressure specified at the and of the diffuser. This is done in order to increase the cavitation number from $\sigma = 1$ to $\sigma = 1.1$ which according to the experimental results [15] should lead to a drastic increase of the shedding frequency.

Table 6.4: Boundary conditions,flow properties and results obtained for the modified re-entrant jet test case.

Parameters	Value
Temperature T [$^{\circ}C$]	14.5
Outlet Pressure P_{outlet} [kPa]	100
Inlet Velocity U [$m.s^{-1}$]	1.48
Cavitation number σ [$-$]	1.11
Pressure Loss [-]	0.5385
Shedding frequency f [Hz]	91.5

This change of condition lead to a slight decrease of the pressure loss compared to the original re-entrant jet test case.

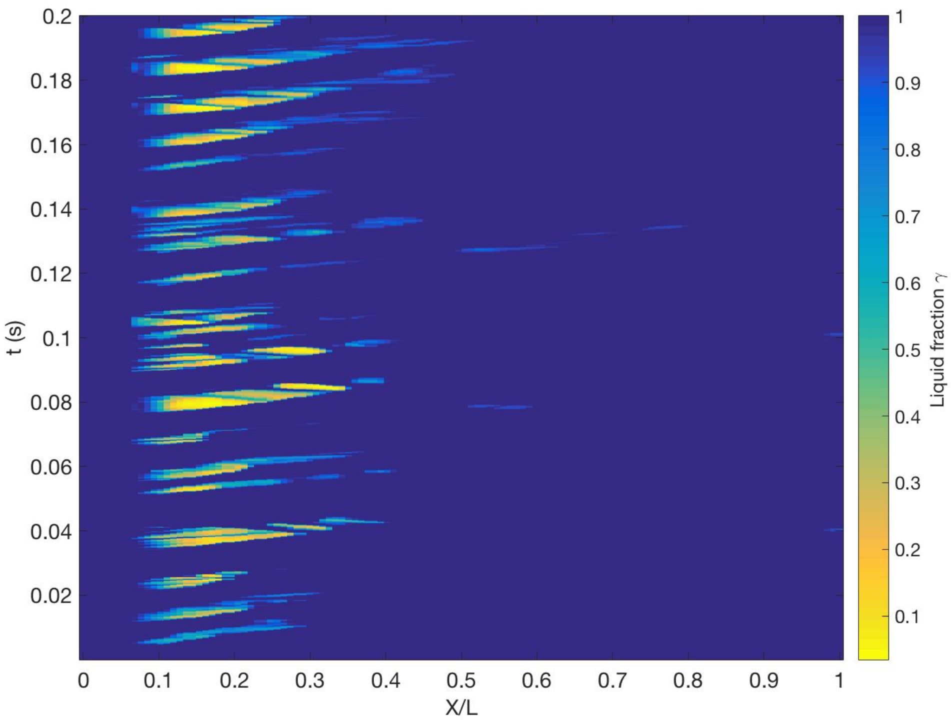

Figure 6.14: Time Evolution of the shedding process over a period of 0.2 s; numerical prediction on the lvl_2 grid. Spanwise-averaged quantities are extracted from a parallel plane at a normal distance of n = 2 mm and plotted along the diverging nozzle. Further is σ = 1.11 (u_0 = 14.5m/s and $p_{outlet,d}$ = 100 kPa). Sampling frequency F_s = 1000kHz).

The X-t diagram of the modified test case is presented in Figure 6.14. The stick-slip shapes are found again and their number is similar to those obtained in Figure 6.8.
The shedding frequency obtained for this test case is 91.5 Hz, which is more important compared to the 83.92 Hz found for the normal re-entrant jet test case. Nonetheless, the frequency is still too small compared to the experimental shedding frequency of 298 Hz obtained experimentally [15].

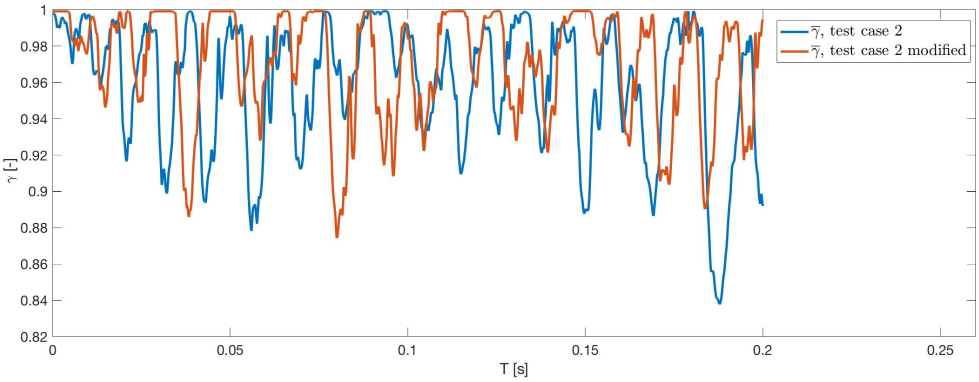

Figure 6.15: Liquid fraction average $\overline{\gamma}$ for the re-entrant jet test case (blue line) and the modified re-entrant jet test case (orange line). Both values are computed from the lvl_2 grid at time step $\Delta t = 1.10^{-6}$s.

The average liquid fraction $\overline{\gamma}$ is plotted in Figure 6.15 to compare both test cases. Both signals exhibit the same sinusoidal behaviour with little change concerning the frequency of oscillation.

6.8. Conclusion

In this test case, CFD computations were performed in order to visualise the re entrant jet mechanism, which occurs at high cavitation number and for moderate flow conditions. After verifying the statistical convergence, the instantaneous flow topology was first studied. The re-entrant jet was clearly visualised as the shedding mechanism. Compared to the bubbly shock test case, the length of the cavities are less important, and the cavitation intensity is less pronounced, due to the high cavitation number implemented. Cavitating vortices structures could be clearly identified, due to the pinch off process which triggered a rotational movement.

Then the temporal evolution of the shedding process was shown, with the construction of the X-t diagram, which displays the time evolution of the shedding process over a certain period of time and along the diverging nozzle. The typical stick slip shapes that are found with the re-entrant jet mechanism were found, even if not every shapes was well captured. The negative velocities of the re-entrant jet, in the order of magnitude of the flow velocity were found.

Finally in order to compare the experimental results and the CFD computations, the shedding frequency was determined by a spectral analysis in the diverging nozzle area. This results in the computation of a Strouhal number which is compared to the one obtained experimentally at the same flow conditions. This is displayed in Figure 8.3.

The Strouhal number obtained numerically is very different from the one obtained experimentally. A modified test case was created to assess whether this difference was caused by the overestimation of the pressure at the inlet of the venturi or if the steepness of the $St_d - \sigma$ slope was to blame. It appears that increasing the cavitation number leads to an increase of the Strouhal number, but not sufficient enough to be comparable to the experimental results.

This means that the pressure loss is responsible for the bad estimation of shedding frequency.

7

Transition regime

This chapter examines the final test case implemented in this study in order to visualize and study the transition regime. This particular state is obtained for cavitation numbers below 0.95 and superior to 0.40, allowing both shedding mechanisms studied in the previous chapter to co-exist. First, the simulation setup and boundary conditions for this case are introduced, following the experiments performed at TU Delft [15]. The instantaneous flow topologies are then presented, where the two shedding mechanisms are introduced. Then, the results are presented, first by visualizing the instantaneous flow topology and then by presenting the X-t diagram.

7.1. Simulation setup

7.1.1. Boundary conditions

Figure 4.13 shows the Strouhal - Cavitation number presented in Chapter 2 and the points which will be used as the reference for the computations. When the bubbly shock test case is for low cavitation number, present at the extreme left of figure 4.13, and the re entrant jet mechanism is for high cavitation number, at the extreme right in Figure 4.13 , the transition regime is situated in between these two test cases.
This means that in order to investigate the transition regime, boundary conditions for both previous test cases must be implemented. Table 7.1 present the parameters of the experiments performed to study the case showed in figure 4.13. In the experiments, a pressure outlet at the end of the diffuser of $p_{outlet,d} = 90kPa$ is taken, following the conditions from the re-entrant jet mechanism. But an inlet velocity of $u = 1.52m/s$ is taken, which lead to a velocity at the throat of $u_0 = 13.7$ m/s. This gives a cavitation number of $\sigma = (p_{outlet,d} - p_{vap}/(\rho u_0^2/2) = 0.89$.

Table 7.1: Boundary conditions and flow properties for the Re-Entrant Jet mechanism simulation.

Parameters	Value
Fluid	Water
Temperature T [$°C$]	15.81
Outlet Pressure p_{outlet} [kPa]	90
Inlet Velocity u [$m.s^{-1}$]	1.52
Liquid Density ρ_l [$kg.m^3$]	999.
Vapor Density ρ_v [$kg.m^3$]	0.0135
Saturation pressure p_v [Pa]	1795
Cavitation number σ []	0.89

7.1.2. The simulations conducted

Table 7.2 summarises all the simulations conducted for the test case, showing the time step, interval used for statistical sampling and the total physical time.

Table 7.2: Overview of simulations conducted for the transition regime test case.

Grid Level	Time Step (s)	Sampling interval	Physical run time (s)
lvl_0	1×10^{-6}	1×10^{-6}	0.5
	2×10^{-6}	2×10^{-6}	0.5
	4×10^{-6}	4×10^{-6}	0.5
lvl_1	1×10^{-6}	1×10^{-6}	0.5
	4×10^{-6}	4×10^{-6}	0.5
lvl_2	1×10^{-6}	1×10^{-6}	0.5
	2×10^{-6}	2×10^{-6}	0.5
	4×10^{-6}	4×10^{-6}	0.5

A total of eight simulations are performed on three different grids, lvl_0, lvl_1 and lvl_2 grid for three different time steps.

7.2. Verification

7.2.1. Statistical convergence

The statistical convergence is checked for every test case. Only the computation of the TST-B plot are done in order to verify the presence or not of start up effect. The same signals are sampled over time : The average liquid fraction value in the venturi $\overline{\gamma}$ and the liquid fraction value at a discrete location γ_i.

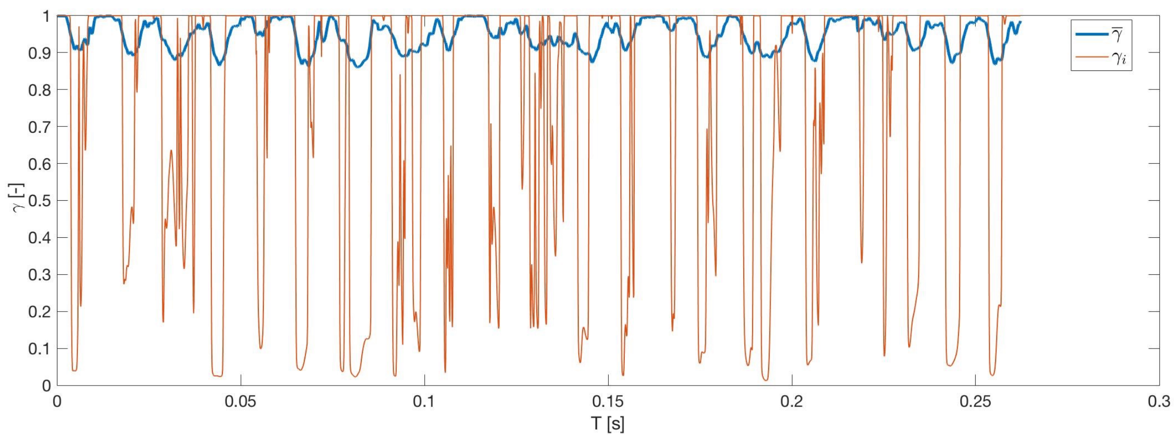

Figure 7.1: Time series of two different signals $\overline{\gamma}$ (blue) and γ_i (orange). Computations performed on the lvl_2 grid at time step $\Delta t = 1 \cdot 10^{-6} s$.

Figure 7.1 presents the two signals probed for the TST-B. The average liquid fraction value in the venturi $\overline{\gamma}$ has very high values and is more close to the $\overline{\gamma}$ computed for the re-entrant test case than the bubbly shock test case, and rarely go below 0.9.

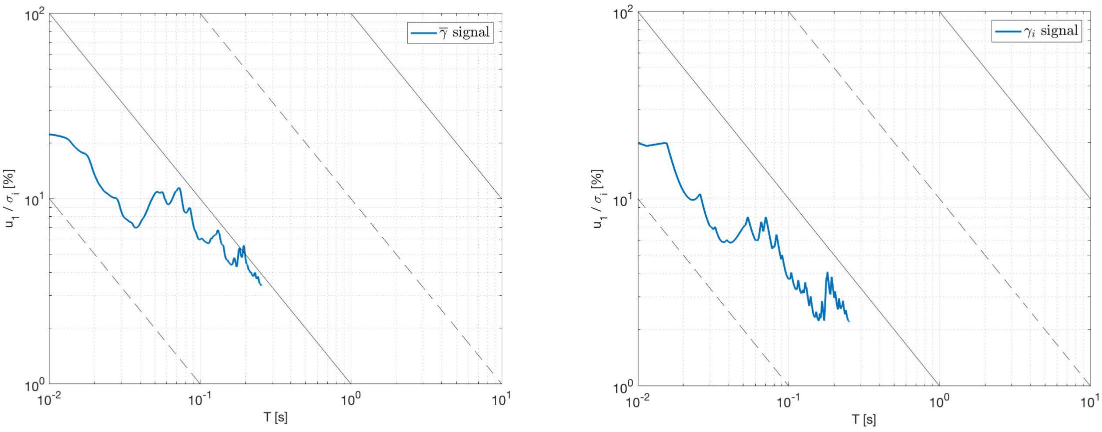

(a) TST-B for $\overline{\gamma}$ signal.

(b) TST-B for γ_i signal.

Figure 7.2: TST-B results for both signals of Figure 7.1, revealing no start up effect. Computations performed lvl_2 grid for a time step of $\Delta t = 1 \cdot 10^{-6} s$.

No hockey stick can be observed in both Figure 7.2a and 7.2b, meaning that no start up effect are present in this computation. The uncertainty is around 4% for $\overline{\gamma}$.

7.2.2. Flow properties and pressure loss

Simulations presented in Table 7.2 are carried out and the pressure loss at the venturi is computed. Table 7.3 presents the pressure computed and sampled at the inlet and outlet of the venturi and the experimental reference.

Table 7.3: Flow properties up and downstream of the venturi ; Comparison between numerical results on grid ,$lvl_2$and the experimental reference.

$P_{inlet,exp}$ (Pa)	$P_{inlet,sim}$ (Pa)	$P_{outlet,exp}$ (Pa)	$P_{outlet,sim}$ (Pa)	K_{exp} (-)	K_{sim} (-)
120470	155493	80050	89967	0.4018	0.6514

The overestimation of the pressure at the inlet is still present, leading to increased value of the pressure loss K. Results are displayed in Figure 8.1 in Chapter 8.
The difference between numerical and experimental pressure loss for this test case is less pronounced that the difference observed for the re-entrant jet test case in Chapter 6, but more important that the one computed for the bubbly shock test case in Chapter 5. It could be expected, as the transition regime is situated in an intermediate region between the bubbly shock and re-entrant jet region.

7.3. Instantaneous flow topology

The transition regime has the particularity of having both bubbly shock and re-entrant jet as shedding mechanisms. With the conditions implemented for this test case, both flow topologies are found and studied at different times of the simulations.

7.3.1. Re entrant jet mechanism

Figure 7.3 presents instantaneous simulation results. The same isosurfaces with the same opacity introduced in chapter 5 in Table 5.4 are used for the study of this test case.
Fourteen representative time instants were selected in Figure 7.3 (a)-(l), exhibiting the growth and progressive shedding of the cavity caused by the re-entrant jet mechanism.
The same behaviour obtained for the second test case is observed. Cavity starts to grow at $t = t_0$ and develop from $t = t_0$ to $t = t_0 + 3.5ms$. A pre detachment of the cavity can be observed in Figure 7.3 (b) at $t = t_0 + 1$ms and cavitating vortices structures are advected by the flow. The re-entrant jet appears in Figure 7.3(f) and travels back under the cavity at a constant velocity from $t = t_0 + 4.5$ms to $t = t_0 + 7$ ms until the beginning of the pre detached cavity is reached. The pinch off occurs in Figure 7.3 at $t = t_0 + 6.5$ms causing the full detachment of of the partial cavity.
The re-entrant jet continues to travel back and reaches the apex of the diverging nozzle, causing the shedding of the rest of the partial cavity attached to the wall. The detached cavity in Figure 7.3 (k) doesn't seem to be advected by the flow and remains in the same place until the rest of the partial cavity sticked a the wall of the apex is detached. The shedding time seems more important compared to the re-entrant jet observed for the test case case 2 on figure .

Then shedding process is then visualised using a mid-plane slice. Figure 7.4 shows a series of six consecutive time instants in the form of the instantaneous liquid fraction γ, horizontal velocity U_x and pressure p in the diverging nozzle. All these values were taken in a mid-plane slice. In order to relate the fields of velocity and pressure to the occurrence of cavitation, isocontours of γ were included in (b) and (c). The same behaviour present in chapter 6 can be observed. A pre-detachment of the partial cavity is observed at $t = t_0$ due to a re-entrant liquid jet visible in Figure 7.4(b) with a negative velocity. The pressure gradient is still present, with a stagnation approximately at the same geometrical place compared to the re-entrant jet test case. The re-entrant jet develops and propagates from $t = t_0 + 1$ ms to $t = t_0 + 2.5$ ms with a decrease in the velocity and the same wave disturbance pattern already observed in Chapter 6. The pre-detached cavity is pinched off at $t = t_0 + 2.5$ ms and the cavity stick to the apex of the venturi throat is shed at $t = t_0 + 3.5$ ms. No particular differences are observed compared to chapter 6.

7.3.2. Bubbly shock mechanism

Fourteen others representative time instants are selected and presented in Figure 7.5. This time, it shows a shedding cycle dominated by the bubbly shock mechanism although a re-entrant jet mechanism was described above. Figure 7.5 (a) presents the beginning of the growth of the cavity. It is followed by a cavity residual from the previous one. From $t = t_1$ to $t = t_1 + 3ms$, the cavity continues to grow and the cavity residual is compressed. The cavitation cloud which was advected by the flow is condensed from$t = t_0$ to $t = t_0 + 3.5ms$ collapses in Figure 7.5, causing the apparition of a shock front. The compressed cavity residual is left unchanged while the shock front travels back towards the apex of the diverging nozzle, causing the shedding of the cavity. This can be observed in Figure 7.5 (f)-(m) from $t = t_1 + 3.5$ms to $t = t_1 + 8$ms. The cavity is definitively separated from the wall in Figure 7.5 at $t = t_1 + 8.5$ms. The difference observed with the bubbly shock test case presented in Chapter 5 is the cavity residuals traveling with the cavity and the length of the partial cavity which is less important in this case. This can be explained by the lower pressure loss.
The bubbly shock shedding mechanism is also observed using a mid plane slice and results are presented in Figure 7.6. In this shedding cycle, a preliminary re-entrant jet can be observed at $t = t_1$ with a negative velocity below the grown partial cavity, inducing a liquid jet propagating towards the throat of the diverging nozzle and causing a pre-detachment of the cavity. But here, it is a bubbly shock which develops and cause the shedding of the cavity. The shock front is well observed from a $t = t_1 + 3$ms to $t = t_1 + 5.5$ms in Figure 7.6 (a) and (b), with the shock front being modeled by a negative velocity front encountering the partial caty with a velocity equal to the velocity of the flow. The only differences between this bubbly shock mechanism and the one observed in Chapter 5 is the preliminary re-entrant jet and the less important length of the cavity.

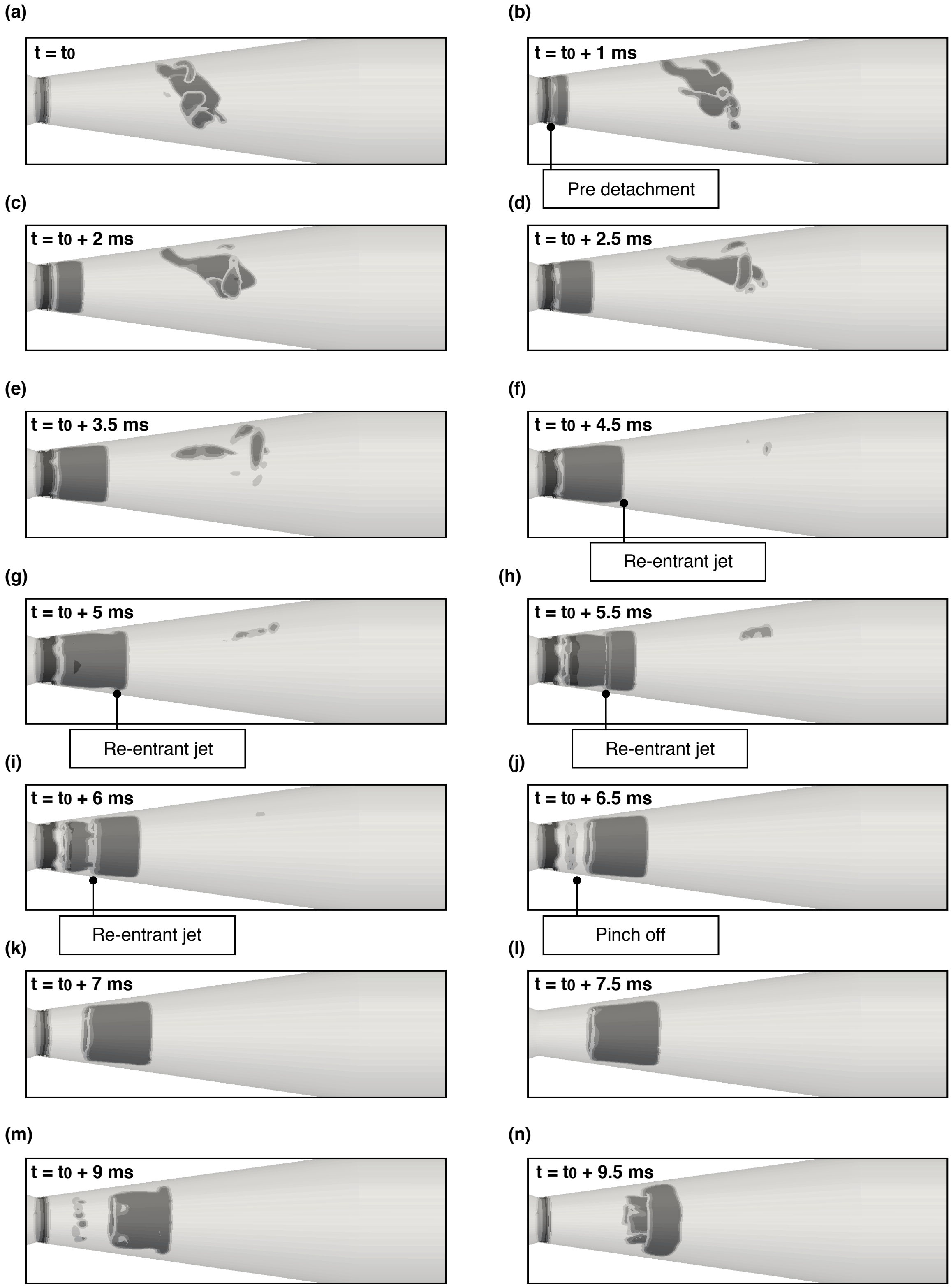

Figure 7.3: Shedding cycle dominated by the re-entrant mechanism during the transition regime. Numerical results show vapour structures with different isosurfaces at different opacity. Simulation performed on the lvl_2 grid for $\Delta t = 1 \cdot 10^{-6} s$.

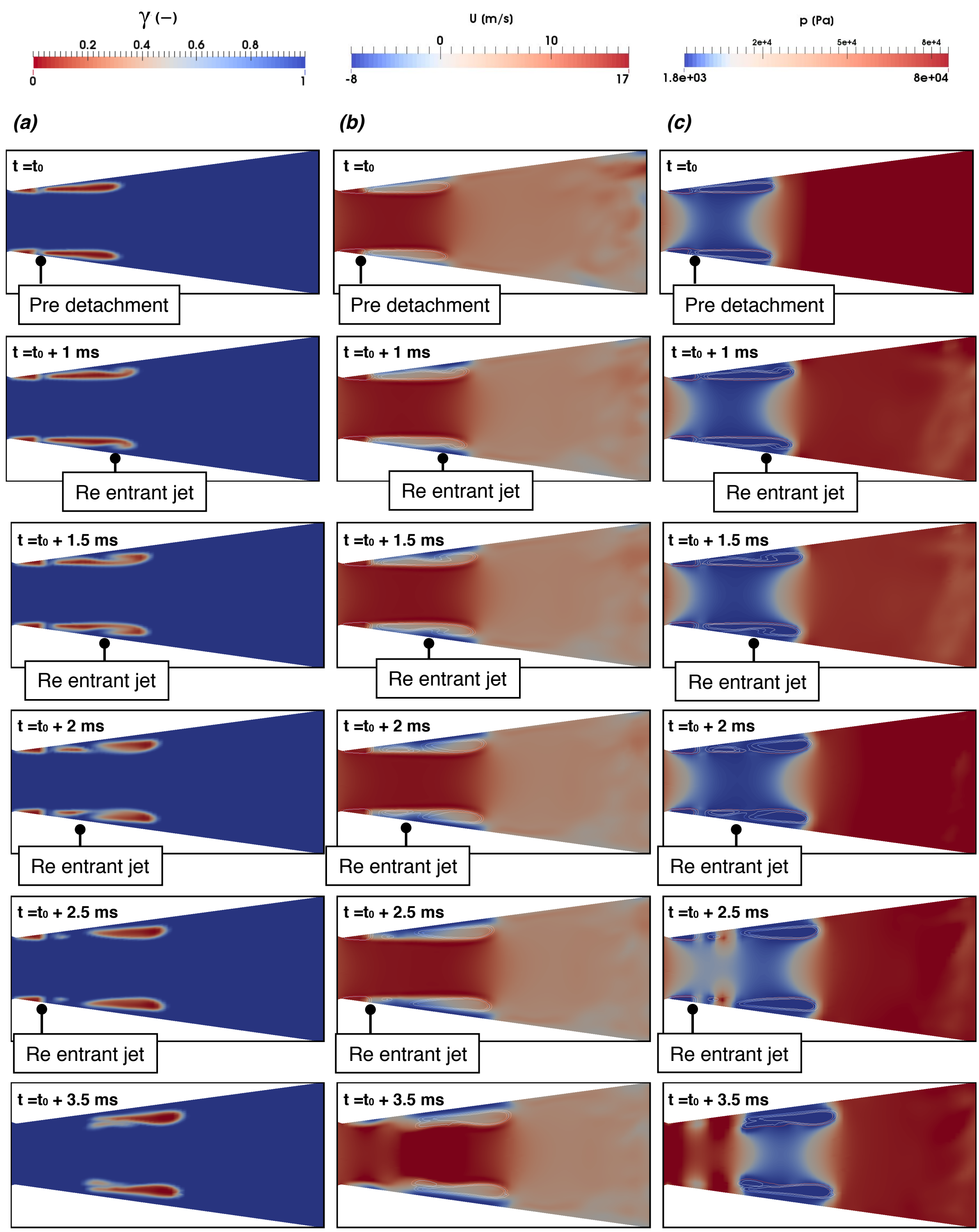

Figure 7.4: Instantaneous flow field captured in a mid-plane slice during a re-entrant jet dominated shedding cycle for six consecutive time instants. Comparison between (a) liquid fraction γ, (b) streamwise velocity U, and (c) pressure p. Simulation performed on the lvl_2 grid for $\Delta t = 1 \cdot 10^{-6}\,s$.

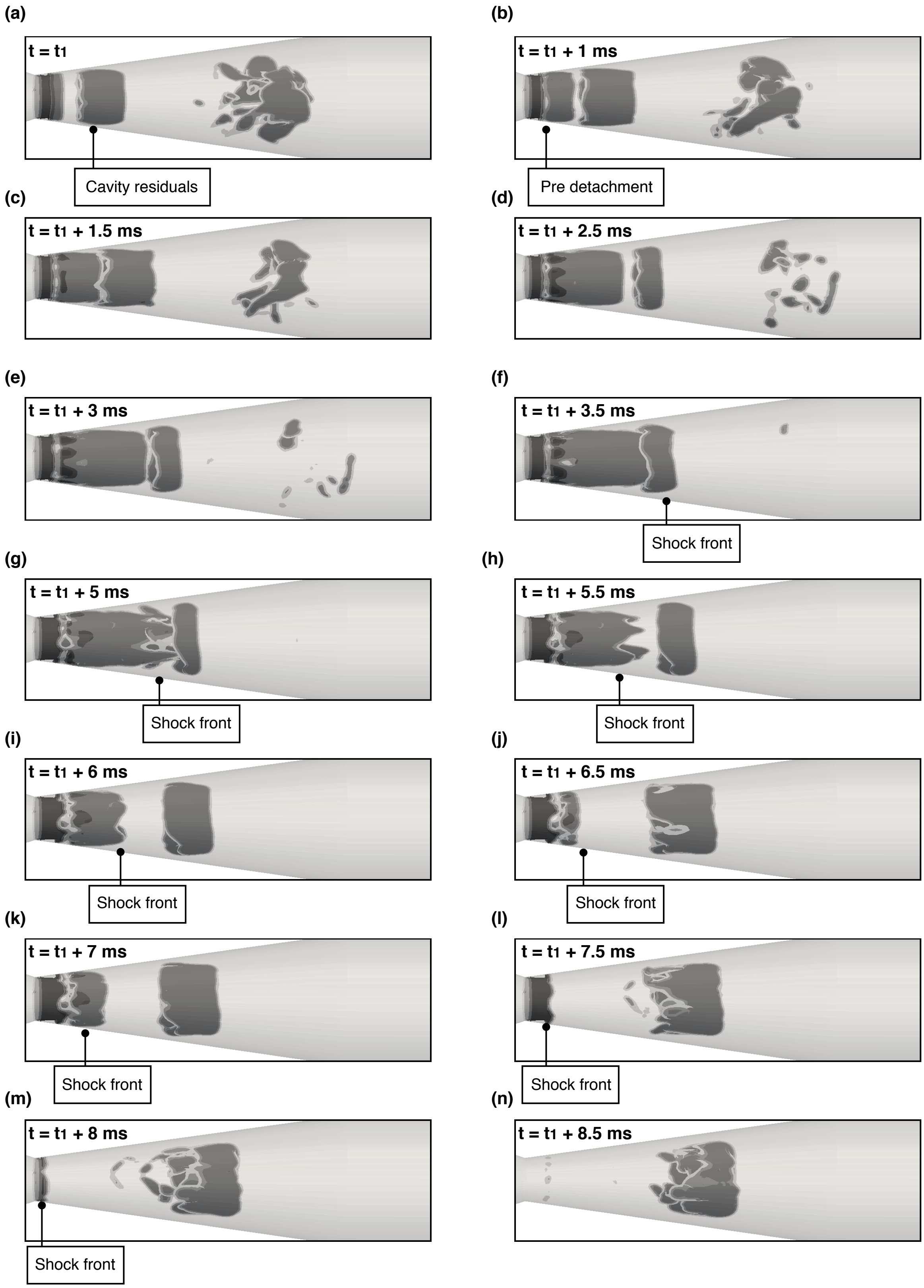

Figure 7.5: Shedding cycle dominated by the bubbly shock mechanism during the transition regime. Numerical results show vapor structures with different isosurfaces at different opacity. Simulation on the lvl_2 grid for $\Delta t = 1 \cdot 10^{-6} s$.

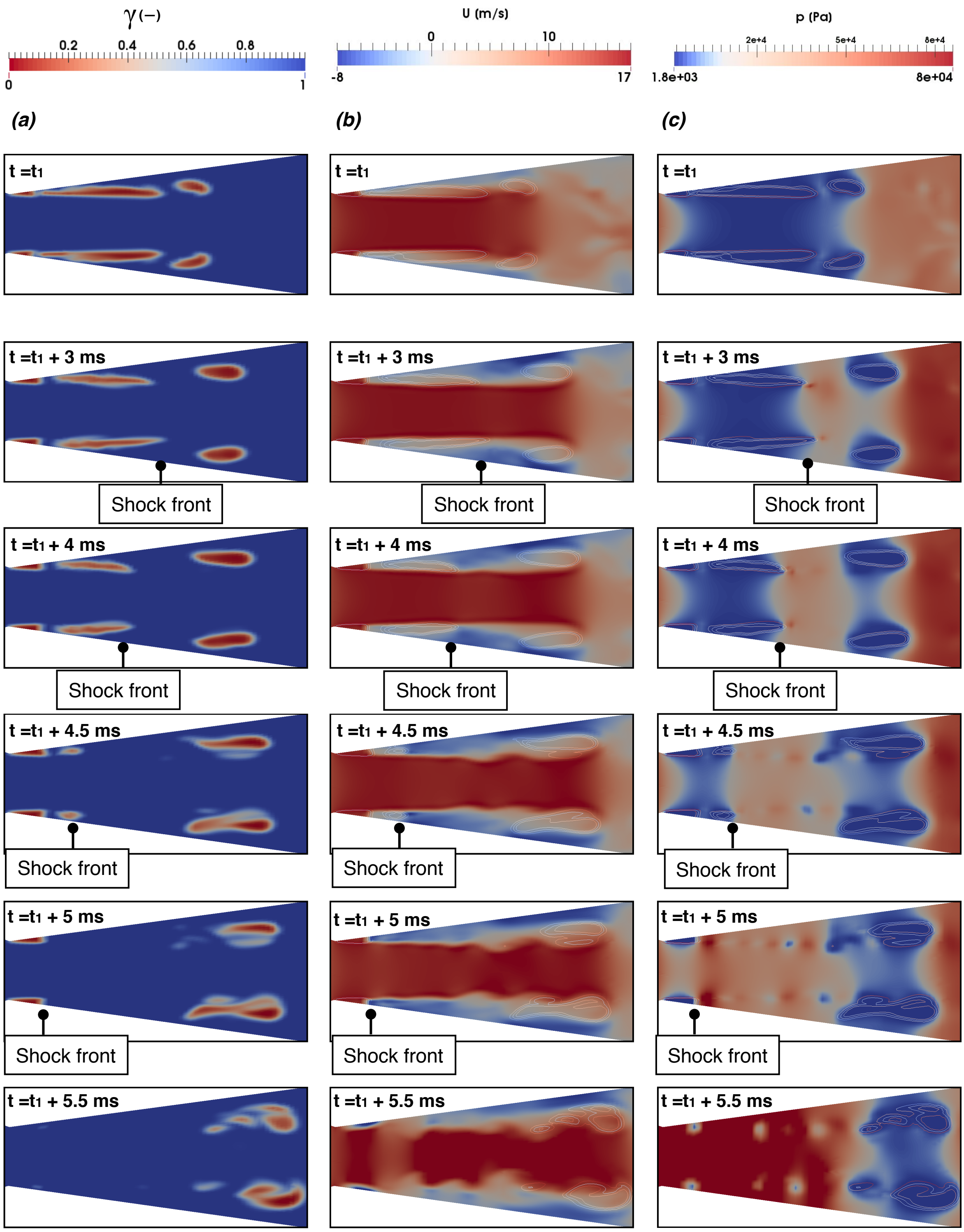

Figure 7.6: Instantaneous flow field captured in a mid-plane slice during a shock dominated shedding cycle for six consecutive time instants. Comparison between (a) liquid fraction γ, (b) streamwise velocity U, and (c) pressure p. Simulation performed on the lvl_2 grid for $\Delta t = 1 \cdot 10^{-6}\,s$.

7.4. Temporal evolution of the shedding process

It appears that both shedding mechanisms are present in this test case. In the intermediate region depicted by Hogendoorn [15], neither the re-entrant jet mechanism nor the bubbly shock mechanism is found to be dominant. Thus, the temporal evolution of the shedding process for this test case is studied in order to determine .

7.4.1. X-T diagram

The shedding process across multiple cycles can be further analysed by plotting the X-t diagram, following the same procedure presented and applied in Chapter 5 and 6. Figure 7.7 shows the obtained variation in time for the liquid fraction γ, plotted along the X direction for a total time of 0.5 s.

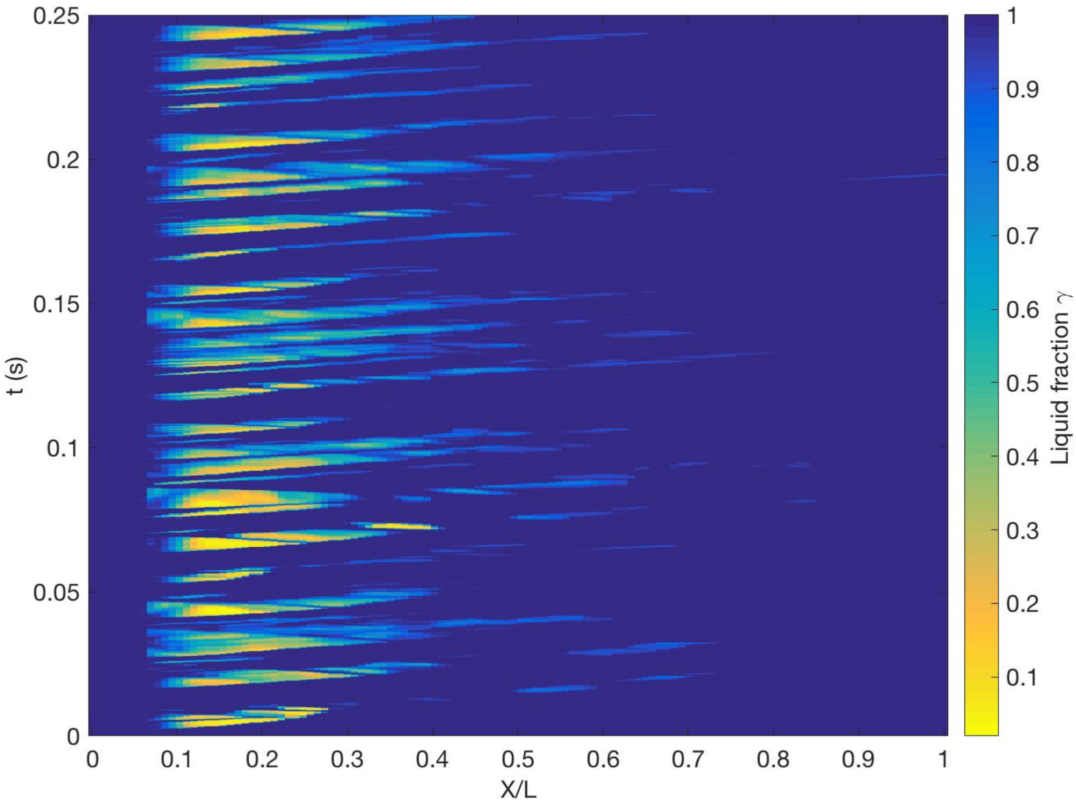

Figure 7.7: Time evolution of the shedding process over a period of 0.25 s; numerical prediction on the lvl_2 grid. Spanwise-averaged quantities are extracted from a parallel plane at a normal distance of n = 2 mm and plotted along the diverging nozzle. Further is σ = 0.89 (u_0 = 13.7m/s and $p_{outlet,d}$ = 90 kPa). Sampling frequency F_s = 1000kHz).

Both triangular and stick slip shapes can be found in Figure 7.7 but they are hardly distinguishable. A stick slip shape is for example visible t = 0.6 ms, followed by triangular shape at t = 0.7 ms.

It appears that the shape are modulated. Indeed, in Figure 7.7, the different shapes are grouped in five blocks, separated by an interval of time where no shedding seems to occur. Figure 7.8 shows a total of three shedding interval for a total time of 0.14 s. Each of these intervals are separated by a time t = 0.02 s. This modulation was also observed in the transition regime during the experiments [15].

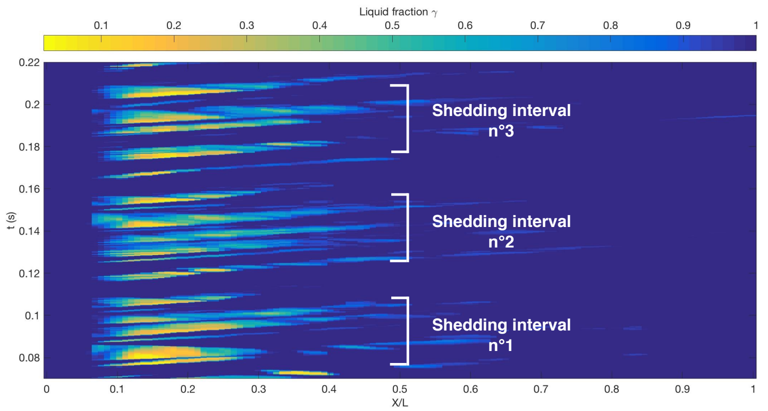

Figure 7.8: Zoom of the X-t diagram presented in Figure 7.7 and observation of shedding interval.

Cavity length The pressure X-t diagram is computed in order to better visualise the shapes present in this test case. Results are shown in Figure 7.9

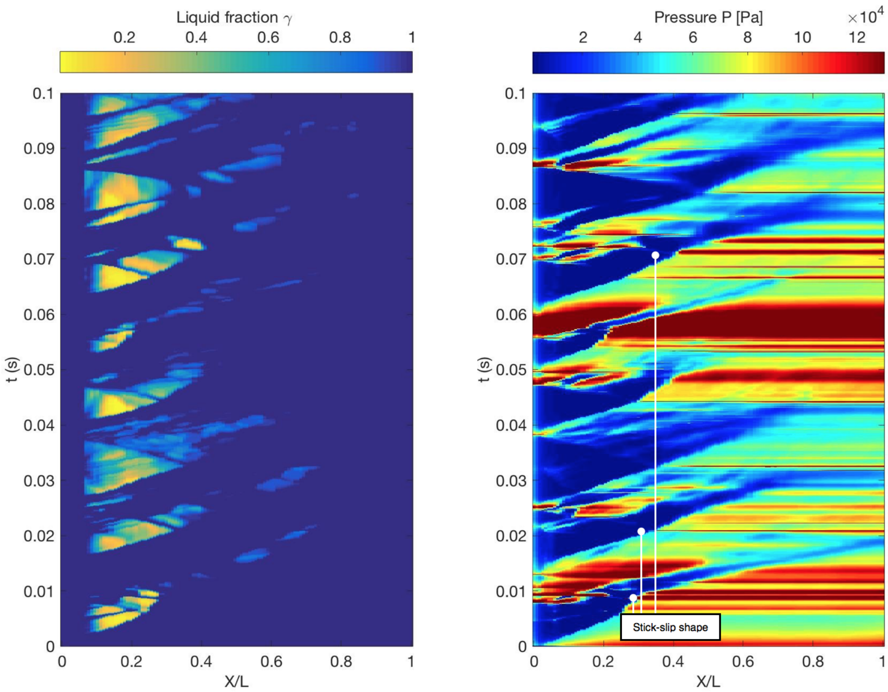

Figure 7.9: Time evolution of the shedding process over a period of 0.25 s; numerical prediction on the lvl_2 grid. Spanwise-averaged quantities are extracted from a parallel plane at a normal distance of n = 2 mm and plotted along the diverging nozzle. (a) is the liquid fraction γ and (b) is the pressure p. Further is $\sigma = 0.89$ ($u_0 = 13.7 m/s$ and $p_{outlet,d}$ = 90 kPa). Sampling frequency $F_s = 1000 kHz$) .

Both stick slip shapes and triangular shapes can be found. The stick slip shapes are clearly visible on the pressure X-t diagram, for example around 0.02 and 0.065 s and present the same behaviour that the ones presented during the re-entrant jet test case. The triangular shapes proving the existence of a bubbly shock mechanism are also visible both in Figure 7.9(a) and 7.9(b). With this figure, the average length of the cavity can be computed. Results are displayed in Figure 8.2.

A value of $l/d = 2.48$ is found for the numerical simulation, whereas a adimensional number $l/d = 1.42$ was found experimentally. As usual, it seem the overestimation of pressure leads to larger cavity length, but the difference is less important compared to the re-entrant jet case.

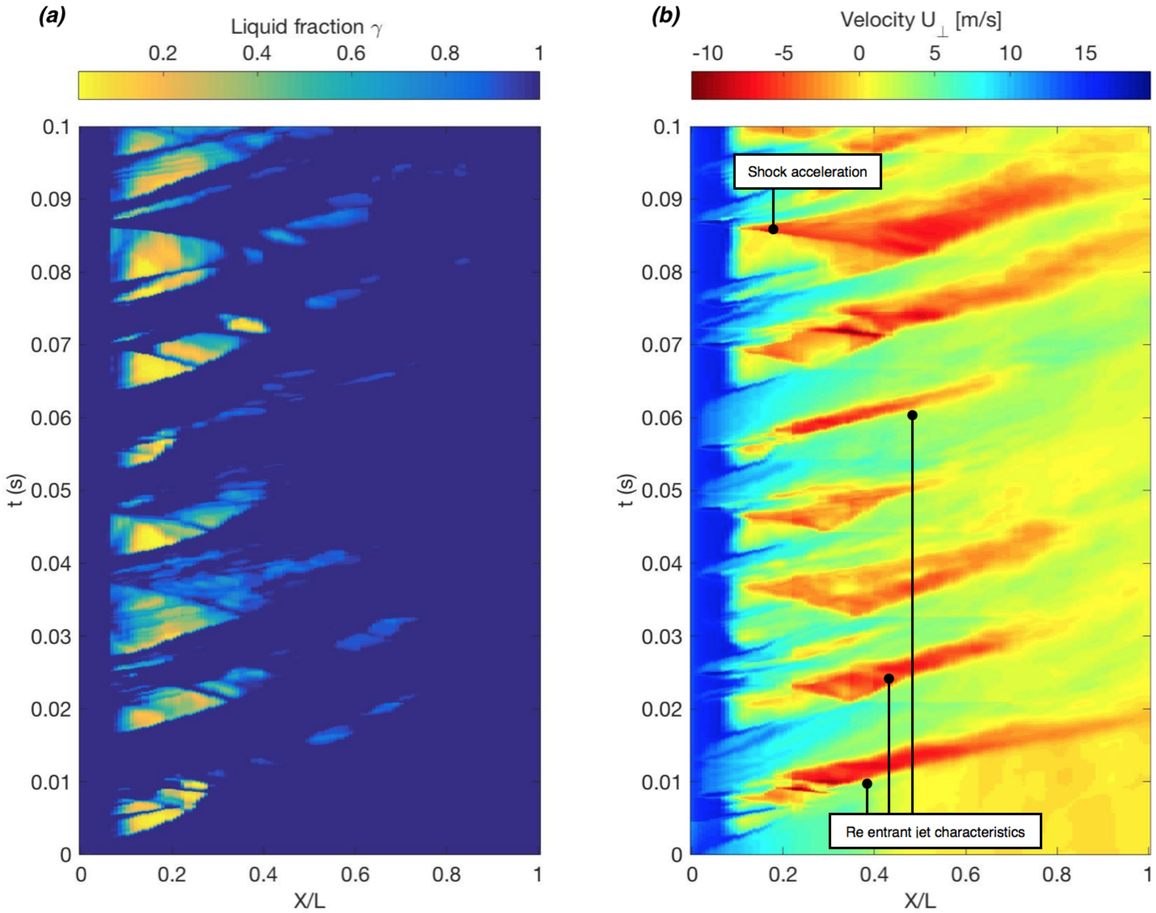

Figure 7.10: Time evolution of the shedding process over a period of 0.25 s; numerical prediction on the lvl_2 grid. Spanwise-averaged quantities are extracted from a parallel plane at a normal distance of n = 2 mm and plotted along the diverging nozzle. (a) is the liquid fraction γ and (b) is the velocity v. Further is $\sigma = 0.89$ ($u_0 = 13.7 m/s$ and $p_{outlet,d}$ = 90 kPa). Sampling frequency $F_s = 1000 kHz$)

Finally, Figure 7.10 presents X-t diagrams based on the liquid fraction γ and velocity u. The acceleration of flow due to the presence of a shock front is visible at $t = 0.9$s, which proves the presence of a bubbly shock mechanism. Other shapes which show the presence of the re-entrant liquid jet negative velocities are present at different time of the computation.

7.5. Shedding Frequencies

The shedding frequency of the transition regime is computed with the same method presented in Chapter 5. The power spectral density of velocity u, pressure p and liquid fraction γ is computed along the venturi nozzle. Results are presented in Figure 7.11.

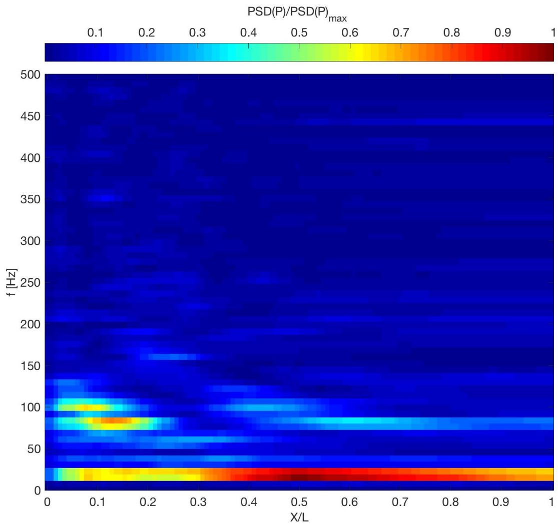

(a) Power spectral density of the pressure p along the diverging nozzle.

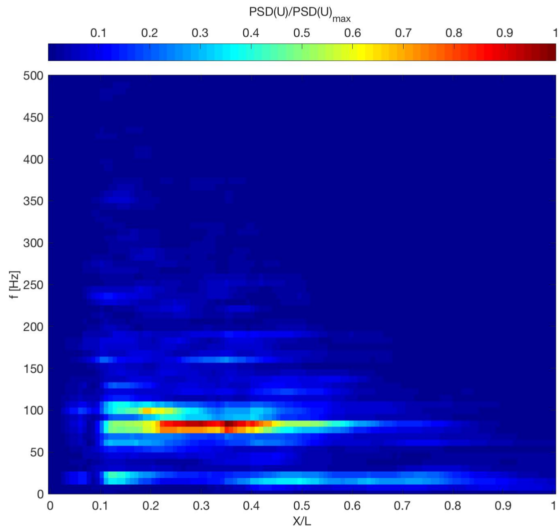

(b) Power spectral density of the velocity u along the diverging nozzle.

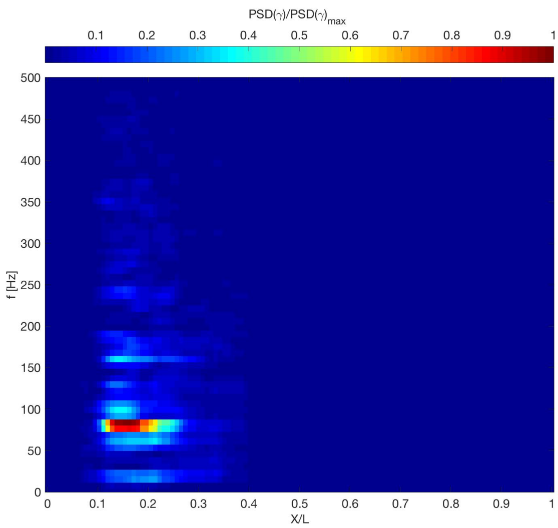

(c) Power spectral density of the liquid fraction γ along the diverging nozzle.

Figure 7.11: Spectral analysis along the diverging nozzle using average values of u,p and γ ; values taken for the computation performed at the lvl_2 grid for a time step $\Delta_t = 1.10^{-6}$ s.

The results computed for the power spectral density of velocity u in Figure 7.11c and liquid fraction in Figure 7.11b exhibit the same features observed in Chapter 5 and 6. Indeed, a single dominant frequency is found for both these plots. This dominant frequency is found between X/L = 0.1 and X/L = 0.25 which correspond to approximately the mean length of the cavity in this test case.
The results is different for Figure 7.11a, where several dominant frequencies are found. The first one is obtained for the same values found in Figure 7.11c and 7.11b, but the most important one is found at around 10 Hz and is present in all the diverging nozzle.

The study of the temporal evolution of the shedding process showed that neither the re-entrant jet mechanism, nor the bubbly shock mechanism was found to be dominant in the transition region. This low-frequency component is caused by switching between both the modes i.e. from the re-entrant jet mechanism to the bubbly shock mechanism and vice versa. This was already observed in Hogendoorn [15].
For this computation, the shedding frequency obtained is $f = 83.92$ Hz, which corresponds to a Strouhal number of $St_d = 0.09851$. For the same flow conditions, the shedding frequency obtained in the experiments was $St_{d,exp} = 0.1187$. A relative error of 17 % is obtained, which is better than the bubbly shock test case where the relative error was 25.4 %.

7.6. Grid and time convergence study

A grid and time convergence study is performed with the results of the computations presented in Table 7.2.

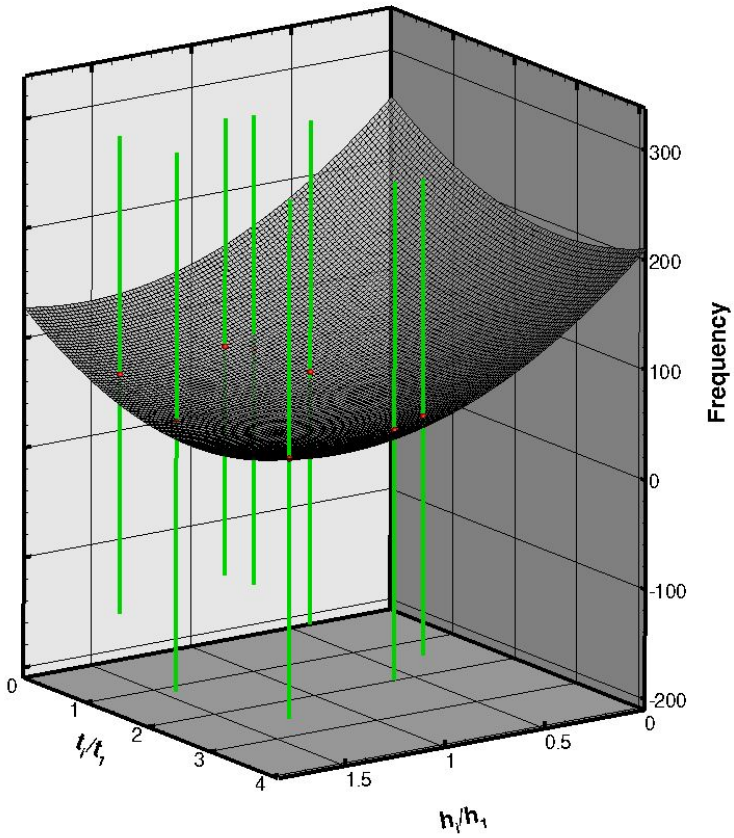

Figure 7.12: Surface fit of the calculated shedding frequency based on the computations presented in Table 7.2. The size of the green segments indicate the uncertainty of each data point (red dot).

The results are implemented in Figure 7.12. It appears that the surface fit of the calculated shedding frequencies doesn't show any convergence behaviour towards a constant value when h_i/h and t_i/t decreases. Like the bubbly shock test case, this may be due to the insufficient number of computations performed on different grids at different time step size. The uncertainty of the determination of the shedding frequency may also be too high.
Thus, for this test case, the final shedding frequency used for the comparison with experimental results is the one obtained for the computation on the finest grid, for $h_i/h = 1.26$ and at the finest time step $\Delta t = 1 \cdot 10^{-6} s$. This corresponds to $f_T = 83.92$Hz obtained in Figure 7.11.

7.7. Conclusion

In this final test case, CFD computations were performed in the transition region, which is set up by implementing an intermediate cavitation number. In this regime, both bubbly shock and re-entrant jet mechanisms are responsible for the shedding of the cavities, and neither of the two are dominant.
After verifying the statistical convergence of our computations, the instantaneous flow topology was first studied. It showed that both shedding mechanisms were present and exhibited the same characteristics presented in Chapter 5 and 6.
Then, in order to verify that no mechanisms was predominant, the temporal evolution of the shedding process was studied, with the construction of the X-t diagram for the liquid fraction γ, the velocity u and the pressure$p$. The typical triangular stick slip shapes were observed and the mean length of the cavity could be computed. Finally in order to compare the experimental results and the CFD computations, the shedding frequency was determined by a spectral analysis in the diverging nozzle area. This results in the computation of a Strouhal number equal to $St_d = 0.0985$, which is closed from the one obtained experimentally $St_d = 0.1187$.

It can be concluded that the computation matches with the experiments, as the results are similar. The low shedding frequency obtained numerically compared to the one obtained experimentally can still be explained by the overestimation of the pressure, resulting in longer cavity length.

8
Conclusion

Partial cavities forming in wedges, hydrofoils or nozzles can exhibit a particular behavior. They form and develop along the wall and can have a certain stability at certain flow conditions. However, with a change in flow conditions, these stable cavities experience auto-oscillation of cavity length and a shedding of the vapor clouds appear.
Experiments performed by Hogendoorn [15] at TU Delft facilities in a diverging-converging nozzle showed the existence of two distinct shedding process. The most known is the re-entrant jet, pressure driven mechanism which appears at high cavitation number under the form of a re-entrant liquid jet starting at a stagnation point. But the other one, called the bubbly shock behavior, has a total different behavior. THis time, a propagating void fraction discontinuity was discovered, causing the partial cavities to retract before being totally shed when the shock wave was located at the apex.
Following these results, the accompanying question is :

Can we reproduce with a robust and validated numerical method the main cavitation dynamics present in a venturi nozzle, especially a shock wave with a incompressible model ?

After a bibliographic review of the different shedding mechanisms and the different methods to compute them, a geometry was reproduced on Ansys CFX, and several grids were created.
Then, three case studies were performed using a mass transfer model for an inviscid flow.

8.1. Test cases

8.1.1. Bubbly shock mechanism

The bubbly shock mechanism is the hardest study case, since it is a shock wave driven phenomenon appearing at low cavitation number and that is modeled in this study by a incompressible solved. The instantaneous flow topology showed a clear visualisation of the bubbly shock with the formation of shock front responsible of the shedding of the large partial cavities present in the venturi. Then, the temporal evolution of the shedding process was demonstrated using the X-t diagrams. The typical triangular shapes found in these diagrams proved the existence of shock fronts. The velocity of the growing cavity and of the propagating shock front were investigated and compared to the experiments performed under the same flow conditions. The Hugoniot-Rankine jump condition [4] of the shock front was studied and verified for several cases.
Finally, in order to determine the Strouhal number and to compare it with the experimental results, a spectral analysis was performed. Results exhibited similarities with the experimentation. The bubbly shock was in conclusion well reproduced with our CFD model, because of the similar results obtained compared to the experimentations.

8.1.2. Re-entrant jet mechanism

The re-entrant jet is the most common shedding process to occur and has been already extensively studied. Since it a pressure driven and not a shock wave driven phenomenon, this study case is easier to compute. The instantaneous flow topology exhibited the typical behavior of a re-entrant jet process, with small partial cavities which where shedded by a re-entrant liquid jet. The temporal evolution of the shedding process using a X-t diagram showed typical stick slip shapes of a re-entrant jet mechanism, even if every shedding processes were not entirely shown due to the plane taken for the probing of the data. The Strouhal number computed with a spectral analysis was found to be not similar to the one obtained during the experimental results. This also could be due to the overestimation of the inlet pressure causing a very important pressure loss. However, clear differences between this case and the bubbly shock case were demonstrated and both regimes were distinguished.
A modified re-entrant jet test case was implemented by increasing the cavitation number in order to study the evolution of the shedding frequency. If an increase of St_d was observed, it was not significant enough, meaning the pressure loss is the most probable cause of error.

8.1.3. Transition regime

The test case for the transition regime is still not entirely finished, as some of the computations are still not done. They will be finished next week. But using the X-t diagram, the presence of both re-entrant jet and bubbly shock mechanism can be visualised, and the Strouhal number obtained with the shedding frequency computed with a spectral analysis is close to the one obtained experimentally.

In conclusion, the Strouhal-cavitation number diagram, cavity length-cavitation number diagram and pressure loss-cavitation number diagram constructed by Hogendoorn [15] can be completed by our results for the three study cases.

First, the $K-\sigma$ diagram is constructed :

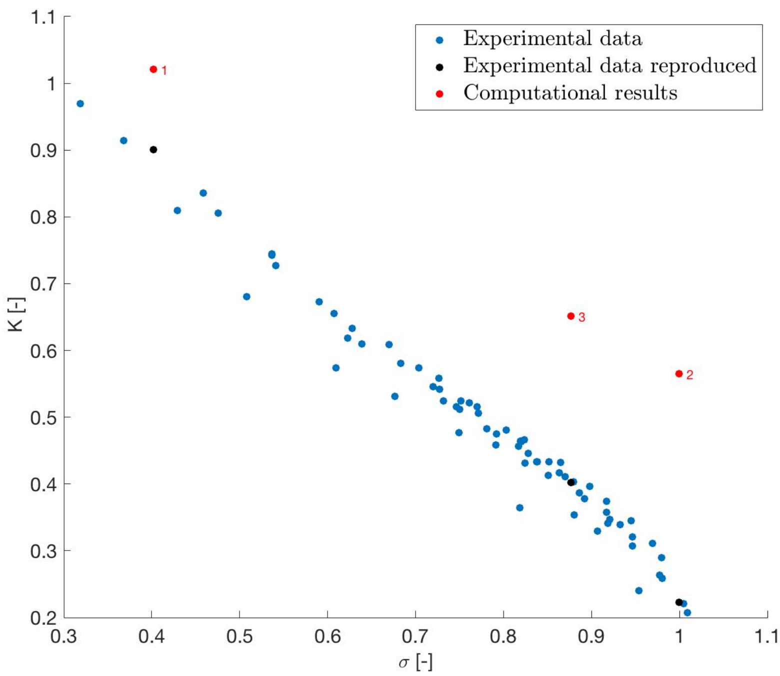

Figure 8.1: Pressure loss coefficient K as function as the cavitation number σ. Comparison between the experimental results [15] (black dot) and the three test cases performed in this study (red dot).

For every test case, the inlet pressure p_{inlet} and thus the pressure loss is overestimated, especially for the re-entrant jet test case. This induces longer cavity length as shown in Figure 8.2

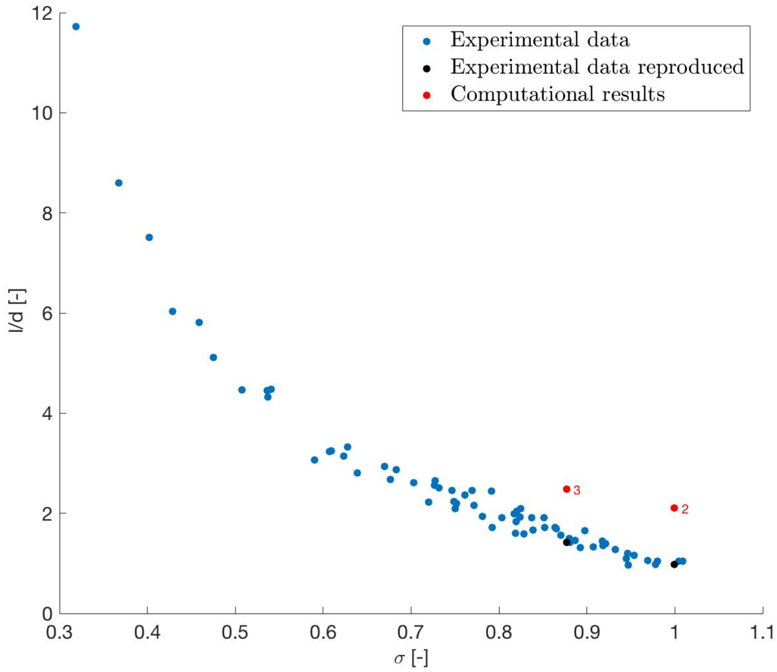

Figure 8.2: Average length of the cavity at the time of detachment (scaled with the throat diameter of the Venturi) as a function of the cavitation number; Data obtained by Hogendoorn [15]. Comparison between the experimental results [15] (black dot) and the three test cases performed in this study (red dot).

Finally, the $St_d - \sigma$ diagram is presented in Figure 8.3

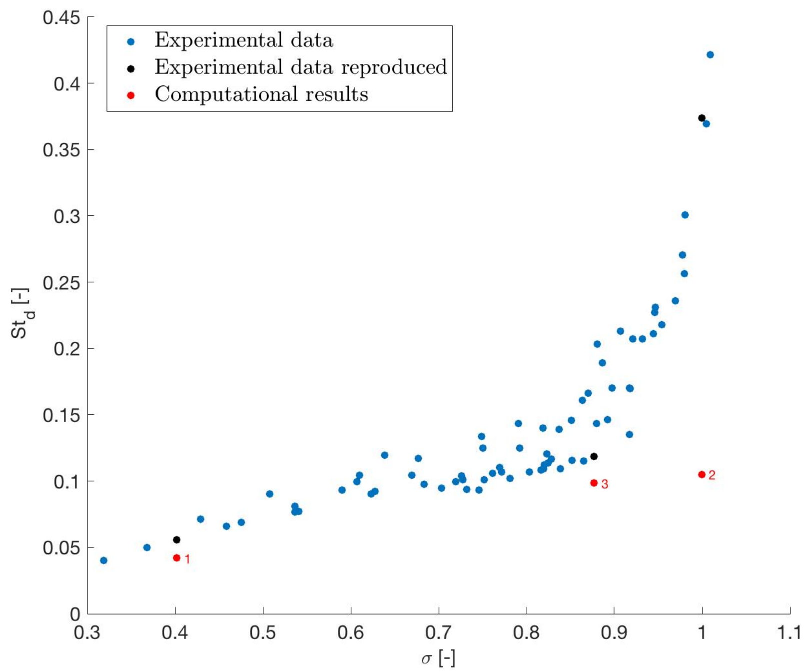

Figure 8.3: Strouhal - cavitation number diagram. Comparison between the experimental results [15] (black dot) and the three test cases performed in this study (red dot).

The transition regime and the bubbly shock mechanism fit very well the curve obtained experimentally, on the contrary of the re-entrant jet mechanism. However, for the test case 1 and 2, different shedding processes and behavior were found, which is satisfactory.

Our CFD model seems to work well enough as both re entrant jet and bubbly shock mechanisms were found for different flow conditions and match the experimental results on those same flow conditions. Turbulence model doesn't seem necessary to reproduce the different mechanisms, but the influence of turbulence should be investigated in order to verify this assumption.

The relative error for the pressure loss ϵ_K, for the Strouhal number ϵ_{St_d} and for the cavity length ϵ_l can be computed for every test cases.
Results are shown in Table 8.1

Table 8.1: Relative error for the Strouhal number, cavity length and pressure loss

Absolute relative error	Bubbly shock regime	Re entrant jet regime	Transition regime
ϵ_K [%]	13.3	147.8	62.1
ϵ_{St_d} [%]	25.4	71.9	17
ϵ_l [%]		114	74.44

8.2. Future prospects

Future research recommendations are presented. The first four points are recommendations for further analysis of the CFD model implemented. The point after that discuss the validity of the CFD model implemented. Finally, the last point is presented for the industrial use of this solver.

- Perform other test cases at different conditions to complete the Strouhal - Cavitation number diagram and verify is they match the experimental conditions.
- Study the cause of overestimation of the pressure, especially at high cavitation numbers.
- Perform computations at a more refined grid to verify the convergence of the study cases.
- Perform longer computations to study the periodical behavior of the cavity length and shedding frequency observed in Chapter 5.
- Investigate the influence of turbulence by performing RANS or LES computation for particular study cases to check the quality of the inviscid solver.
- Investigate the vortical structures that typically occur in both regimes, by what are they caused by. This is of a particular importance, because these vortical structures can cause severe erosion damages when they collapse.

Appendices

A

RANS modeling

A.0.1. RANS equations

Cavitation regimes are highly complex. They involve a large variety of physical phenomena : Bubble Dynamics, non equilibrium thermodynamics, multi phase turbulence and multi phase wave and shock dynamics. For the simulation of cavitating flow and turbulence modeling, three different methods exist:

- **Direct Numerical Simulation (DNS)** where the Navier-Stokes equations are directly solver, meaning all scales are resolved and no modeling is required. This method has the most direct approach and the highest accuracy but is very coastly in terms of computational resources, especially in cavitating flow where the DNS approach resolves all scales for each fluid phase and interface.
- **Large Eddy Simulation (LES)** where only the large scales of turbulent motion are resolved and the small scales are modeled. If the LES is not as computationally expensive as DNS since only a certain scale is directly solved, it still requires a certain cost and can introduce more problems in modeling due to the introduction of sub grid scales terms, which increases the complexity of the model.
- **Reynolds Averaged Navier Stokes Equation (RANS)** where the mean flow is resolved and a model is implemented to study the turbulence.

For the derivation of RANS equations, , every variable can be replaced by the sum of mean value and fluctuating component : $u(t) = \overline{u} + u'$. This method is known as Reynolds decomposition.
By implementing this decomposition, the Navier-Stokes equation become :

$$\rho(\frac{\partial \overline{u_i}}{\partial t} + \frac{\partial \overline{u_i u_j}}{\partial x_j}) = -\frac{\partial \overline{p}}{\partial x_i} + \frac{\partial}{\partial x_j}(\mu \frac{\partial \overline{u_i}}{\partial x_j}) + \frac{\partial}{\partial x_i}(-\rho \overline{u_i' u_j'}) \tag{A.1}$$

By averaging the equation, the Reynolds stress term $\frac{\partial}{\partial x_i}(-\rho \overline{u_i' u_j'})$ arises. It consists of six unknowns components and thus requires closure; This closure is obtained with the use of additional equations and the turbulence models are classified according to the number of additional equations that they use.

A.0.2. Turbulence models

In this study, focus is put on standard $k-\epsilon$ model, $k-\epsilon$ model with a Reboud correction, Wilcox's $k-\omega$ model and $k-\omega$ SST method.

$k-\epsilon$ model In this model,, two additional transport equations for the turbulent kinetic energy k and the energy dissipation rate ϵ are solved. These quantities re chosen because of the energy cascading mechanism. With these quantities, different numbers can be formed: The turbulent length scale $l = \frac{k^{\frac{3}{2}}}{\epsilon}$, time scale $\tau = \frac{k}{\epsilon}$ and adimensional quantity $\mu_t \frac{k^2}{\epsilon}$.

$$k = \frac{\overline{u_1'^2} + \overline{u_2'^2} + \overline{u_3'^2}}{2} \tag{A.2}$$

$$\epsilon = \mu[\overline{\frac{\delta u_i}{\delta x_j} + \frac{\delta u_i}{\delta x_j}}] \tag{A.3}$$

This model is widely validated, simple to implement and guarantee a numerically stable calculation. However, as stated by Davidson, $k-\epsilon$ models have two important weaknesses : The overprediction of the shear stresses in adverse pressure gradient flows, resulting in a poor prediction of flows with streamlines curvatures and the over prediction of of μ_t in cavitating flow, which could be a trouble for the re-entrant jet case, and the need for near-wall modification.

$k-\epsilon$ model and Reboud correction In previous numerical experiments, a poor agreement between numerical results and experiments was observed. It was related to an overprediction of the turbulent viscosity in the rear part of the cavity. The cyclic behavior of the cloud cavitation process is strongly related to the re-entrant jet development from the cavity closure. As a matter of fact, the main problem in the turbulent flow simulations consisted in the premature removal of the reverse flow along the solid wall ; the re-entrant jet was stopped too early and it did not result in any cavity break off. A modified $k-\epsilon$ RNG model was proposed by Reboud and al [29]. In order to improve the turbulence modeling and to simulate more accurately the re-entrant jet behavior and the vapor cloud shedding, the mixture turbulent viscosity, mainly in the void ratio areas was reduced :

$$\mu_t = f(\rho) C_\mu \frac{k^2}{\epsilon}, \tag{A.4}$$

where

$$f(\rho) = \rho_v + (\frac{\rho_v - \rho}{\rho_v - \rho_l})^n (\rho_l - \rho_v), n > 1 \tag{A.5}$$

Indeed, according to the experimental results, the re-entrant jet seems to be mainly composed of liquid ($\alpha = 0$), and thus the reduction of the mixture turbulence viscosity leads to substantial changes in the simulation. A accurate prediction of the unsteady re-entrant jet is now obtained, and the vapor cloud shedding is now well simulated.

$k-\omega$ model The $k-\omega$ model which was first proposed by Wilcox is a two equation model which solve for the turbulent kinetic energy k and the dissipation rate per unit kinetic energy or specific dissipation ω, instead of ϵ .

$$\mu_t = \rho \frac{k}{\omega}, \tag{A.6}$$

The $k-\omega$ model is superior to the $k-\epsilon$ model relatively to the viscous wall treatment and for the accounting of streamwise pressure gradients.

$k-\omega$ SST model The Shear Stress Transport (SST) $k-\omega$ is a two equation model. It combines both $k-\epsilon$ and $k-\omega$ model features and was originally proposed by Wilcox in 1988. Here, the turbulence frequency ω is calculated as ϵ/k with the dimension Hz. The length scale is calculated as $l = \sqrt{k}/\omega$ and eddy viscosity as $\mu_t = \rho k/\omega$.

Comparison between the different models In order to chose the best turbulence models fitted for this study, the following trade off criterias are applied :

- Simplicity of implementation
- Computational effort
- Physical accuracy
- Computational accuracy
- Computational stability

Table A.1: Classification of the different turbulence models according to the trade off criterias

Models	Simplicity	Computational Effort	Physical Accuracy	Computational Accuracy	Computational Stability
$k-\epsilon$	Excellent	Excellent	Poor	Insufficient	Good
$k-\epsilon$, Reboud correction	Excellent	Excellent	Insufficient	Sufficient	Good
$k-\omega$	Excellent	Good	Insufficient	Sufficient	Sufficient
$k-\omega$ SST	Good	Good	Sufficient	Good	Good

Table A.1 classifies the different turbulence models and their behavior regarding the different criterias applied

Thus, $k-\epsilon$ model with Reboud correction is the best turbulence model for the study of cavitation dynamics, despite its poor physical accuracy.

B
Cavitations models

Table B.1: List of cavitating model.

Model	Sour	C	$f_1(\alpha)$	$f_2(\alpha)$
Kunz et al [20]	$\dot{m}^+$	$\frac{C_d \rho_v}{0.5\rho_l U_\infty^2 t_\infty}$	$(1-\alpha)$	$(p_v - p)$
	$\dot{m}^-$	$\frac{C_p \rho_v}{t_\infty}$	$(1-\alpha)^2\alpha$	1
Merkle [23]	$\dot{m}^+$	$\frac{C_d \rho_l}{t_\infty}$	$(1-\alpha)$	$(p_v - p)$
	$\dot{m}^-$	$-\frac{C_p \rho_v}{t_\infty}$	α	$(p - p_v)$
Inanc and Shy [34]	$\dot{m}^+$	$\frac{\rho_l^2}{\rho_v t_\infty (V_{v,n} - V_l)^2 (\rho_l - \rho_v)}$	$(1-\alpha)$	$(p_v - p)$
	$\dot{m}^-$	$\frac{\rho_l^2}{t_\infty (V_{v,n} - V_l)^2 (\rho_l - \rho_v)}$	α	$(p - p_v)$
Singhal [36]	$\dot{m}^+$	$C_e \frac{\rho_l \rho_v}{\rho} \frac{\sqrt{k}}{\sigma}$	$(1-\alpha-\alpha_g)$	$\sqrt{\frac{2}{3}\frac{p_v - p}{\rho_l}}$
	$\dot{m}^-$	$-C_c \frac{\rho_l \rho_v}{\rho} \frac{\sqrt{k}}{\sigma}$	α	$\sqrt{\frac{2}{3}\frac{p - p_v}{\rho_l}}$
Zwart et al. [44]	$\dot{m}^+$	$C_e \frac{3\alpha_{nuc}\rho_v}{R}$	$(1-\alpha)$	$\sqrt{\frac{2}{3}\frac{p_v - p}{\rho_l}}$
	$\dot{m}^-$	$C_c \frac{3\rho_v}{R}$	α	$\sqrt{\frac{2}{3}\frac{p - p_v}{\rho_l}}$
Schnerr and Sauer [32]	$\dot{m}^+$	$3\frac{\rho_l \rho_v}{\rho}\sqrt[3]{\frac{4\pi n}{3}}$	$\alpha^{\frac{2}{3}}(1-\alpha)^{\frac{4}{3}}$	$\sqrt{\frac{2}{3}\frac{p_v - p}{\rho_l}}$
	$\dot{m}^-$	$-3\frac{\rho_l \rho_v}{\rho}\sqrt[3]{\frac{4\pi n}{3}}$	$\alpha^{\frac{2}{3}}(1-\alpha)^{\frac{4}{3}}$	$\sqrt{\frac{2}{3}\frac{p - p_v}{\rho_l}}$

C

Probing of the datas

This python script creates a range of points used for the probing of the datas inside the Venturi nozzle. Here, the input are the number of points probed for each circle ($nPoints_Circle$), the number of circles created in the Venturi ($nPoints_line$) and the distance between the first and last circles.

```
#!/usr/bin/env python

import os
import shutil
import sys
import math
import numpy
import re

args = sys.argv
nPoints_Circle = 10;
# default values
probeLineDictName = 'probeLineDict'
probesDict = 'probesDict'


filename = './system/' + probeLineDictName
#filename = probeLineDictName
myfile = open(filename,'r')
probeLineDict = myfile.readlines()
myfile.close()

filenameW = './system/' + probesDict
#filenameW = probesDict
mywfile = open(filenameW,'w')

entryFields = '\n'
entryOutput = '\n'

doTheFields = False

for line in probeLineDict:
        # fields
        if line.startswith('fields'):
                doTheFields = True
```

```
        if doTheFields:
                entryFields += line

        if doTheFields & line.startswith(');'):
                doTheFields = False

        # outputControl
        if line.startswith('outputControl'):
                entryOutput += line
                entryOutput += '\n'

        # outputInterval
        if line.startswith('outputInterval'):
                entryOutput += line
                entryOutput += '\n'

        # points
        if line.startswith('start'):
                startCoordsF = map(float,re.findall(r"[-+]?\d*\.\d+|\d+",line))
                startCoords = numpy.array(startCoordsF)
        if line.startswith('end'):
                endCoordsF = map(float,re.findall(r"[-+]?\d*\.\d+|\d+",line))
                endCoords = numpy.array(endCoordsF)
        if line.startswith('nPoints_Line'):
                nPoints_Line = map(int,re.findall("\d+",line))[0]

# end for


# generate points
probeLocationsData = '\n'
incrVec = (endCoords - startCoords)/(nPoints_Line-1)

for i in range(0,nPoints_Line):
    tmpPoint = startCoords + i*incrVec
    for j in range(0,nPoints_Circle):
     a = tmpPoint[1]*math.cos(2*math.pi*j/(nPoints_Circle))
     b =tmpPoint[1]*math.sin(2*math.pi*j/(nPoints_Circle))

     print b


     probeLocationsData += '\t( ' + tmpPoint[0].astype('|S20') + ' '
     probeLocationsData += (a).astype('|S20') + ' '
     probeLocationsData += (b).astype('|S20') + ' )\n'




# end for





# strings
```

```
headerOF   = '/*---------------------------------*- C++ -*-----------------------------------*\\\n'
headerOF += '| =========                 |
|\n'
headerOF += '| \\      /  F ield         | OpenFOAM: The Open Source CFD Toolbox
|\n'
headerOF += '|  \\    /   O peration     | Version:  2.3.x
|\n'
headerOF += '|   \\  /    A nd           | Web:      www.OpenFOAM.org
|\n'
headerOF += '|    \\/     M anipulation  |
|\n'
headerOF += '\*---------------------------------------------------------------------------*/\n'
headerOF += 'FoamFile\n'
headerOF += '{\n'
headerOF += '\tversion\t\t2.0;\n'
headerOF += '\tformat\t\tascii;\n'
headerOF += '\tclass\t\tdictionary;\n'
headerOF += '\tobject\t\tprobesDict;\n'
headerOF += '}\n'
headerOF += '// * * * * * * * * * * * * * * * * * * * * * * * * * * * * * * * * * * * * * //\n'
headerOF += '\n\n'

probeLocationsStart  = '\n// Locations to be probed.\n'
probeLocationsStart += 'probeLocations\n'
probeLocationsStart += '(\n'

probeLocationsEnd = ');\n'

finish = '\n// * * * * * * * * * * * * * * * * * * * * * * * * * * * * * * * * * * * * * //\n'


# write probesDict

mywfile.write(headerOF)

mywfile.write(entryFields)

mywfile.write(entryOutput)

mywfile.write(probeLocationsStart)

mywfile.write(probeLocationsData)

mywfile.write(probeLocationsEnd)

mywfile.write(finish)

mywfile.close()
```

D

Front propagation velocity demonstration

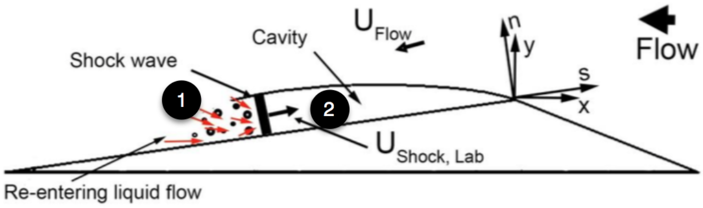

Figure D.1: Shedding cycle in the presence of an obstacle, bubbly shock effect

1 is situated **upstream** of the shock and is defined by :

- Pressure p_1
- Velocity u_1
- Liquid fraction γ_1
- Density ρ_1

2 is situated **downstream** of the shock and is defined by :

- Pressure p_2
- Velocity u_2
- Liquid fraction γ_2
- Density ρ_2

With $p_1 > p_2, \rho_1 > \rho_2, \gamma_1 > \gamma_2$
Mass continuity equation :

$$\rho_1 u_1 = \rho_2 u_2 \tag{D.1}$$

Momentum equation

$$\rho_1 u_1^2 + p_1 = \rho_2 u_2^2 + p_2 \tag{D.2}$$

Introducing equation in the equation, we obtain :

$$u_1^2 = \frac{\rho_2}{\rho_1(\rho_1 - \rho_2}(p_1 - p_2) \tag{D.3}$$

With

$$\rho_1 = \gamma_1 \rho_l + (1-\gamma_1)\rho_v \rho_2 = \gamma_2 \rho_l + (1-\gamma_2)\rho_v \tag{D.4}$$

$$\frac{\rho_1}{\rho_2} = \frac{\gamma_2 + \frac{\rho_v}{\rho_l - \rho_v}}{\rho_1 + \frac{\rho_v}{\rho_l - \rho_v}} \tag{D.5}$$

Bibliography

[1] Rickard E Bensow and Goran Bark. Simulating cavitating flows with les in openfoam. In *V European conference on computational fluid dynamics*, pages 14–17, 2010.

[2] J Brouwer, J Tukker, and M Van Rijsbergen. Uncertainty analysis of finite length measurement signals. In *The 3rd International Conference on Advanced Model Measurement Technology for the EU Maritime Industry (AMT?13), Gdansk, Poland*, pages 260–274, 2013.

[3] J Brouwer, J Tukker, and M van Rijsbergen. Uncertainty analysis and stationarity test of finite length time series signals. In *The 4th International Conference on Advanced Model Measurement Technology for the Maritime Industry (AMT?15), Istanbul, Turkey*, 2015.

[4] Bernd Budich, SJ Schmidt, and NA Adams. Numerical simulation and analysis of condensation shocks in cavitating flow. *Journal of Fluid Mechanics*, 838:759–813, 2018.

[5] Mathieu Callenaere, Jean-Pierre Franc, Jean-Marie Michel, and Michel Riondet. The cavitation instability induced by the development of a re-entrant jet. *Journal of Fluid Mechanics*, 444:223–256, 2001.

[6] De Bruin G. J. De Lange D. F. Sheet cavitation and cloud cavitation, re-entrant jet and three-dimensionality. *Applied Scientific Research*, (58(4):191–114, 1997.

[7] Manish Deshpande, Jinzhang Feng, and Charles L Merkle. Numerical modeling of the thermodynamic effects of cavitation. *Journal of fluids engineering*, 119(2):420–427, 1997.

[8] Luis Eça and Martin Hoekstra. A procedure for the estimation of the numerical uncertainty of cfd calculations based on grid refinement studies. *Journal of Computational Physics*, 262:104–130, 2014.

[9] Jean-Pierre Franc. The rayleigh-plesset equation: a simple and powerful tool to understand various aspects of cavitation. In *Fluid Dynamics of Cavitation and Cavitating Turbopumps*, pages 1–41. Springer, 2007.

[10] Jean-Pierre Franc and Jean-Marie Michel. Attached cavitation and the boundary layer: experimental investigation and numerical treatment. *Journal of Fluid Mechanics*, 154:63–90, 1985.

[11] Jean-Pierre Franc and Jean-Marie Michel. *Fundamentals of cavitation*, volume 76. Springer Science & Business Media, 2006.

[12] Harish Ganesh. Bubbly shock propagation as a cause of sheet to cloud transition of partial cavitation and stationary cavitation bubbles forming on a delta wing vortex. 2015.

[13] Harish Ganesh, Simo A Mäkiharju, and Steven L Ceccio. Bubbly shock propagation as a mechanism of shedding in separated cavitating flows. *Journal of Hydrodynamics, Ser. B*, 29(6):907–916, 2017.

[14] Jie Geng, Dong Li, Guang-sheng Du, et al. Simulation of cavitation induced by water hammer. *Journal of Hydrodynamics, Ser. B*, 29(6):972–978, 2017.

[15] William Hogendoorn. Experimental investigation of cavitation regimes in a converging-diverging nozzle. 2017.

[16] Furness S. P. Hutton S. P. Experimental and theoretical studies of two-dimensional fixed-type cavities. *Journal of Fluids Engineering*, 97.

[17] Saad Jahangir, Willian Hogendoorn, and Christian Poelma. Dynamics of partial cavitation in an axisymmetric converging-diverging nozzle. *International Journal of Multiphase Flow*, 106:34–45, 2018.

[18] Bin Ji, Yun Long, Xin-ping Long, Zhong-dong Qian, and Jia-jian Zhou. Large eddy simulation of turbulent attached cavitating flow with special emphasis on large scale structures of the hydrofoil wake and turbulence-cavitation interactions. *Journal of Hydrodynamics, Ser. B*, 29(1):27–39, 2017.

[19] Dowling Kundu, Cohen. Fluid mechanics, sixth edition.

[20] Robert F Kunz, David A Boger, David R Stinebring, Thomas S Chyczewski, Jules W Lindau, Howard J Gibeling, Sankaran Venkateswaran, and TR Govindan. A preconditioned navier–stokes method for two-phase flows with application to cavitation prediction. *Computers & Fluids*, 29(8):849–875, 2000.

[21] ZR Li. Assessment of cavitation erosion with a multiphase reynolds-averaged navier-stokes method. page 8, 2012.

[22] Skipp S. R. Lush P. A. High speed cine observations of cavitating flow in a duct. *International Journal of Heat and Fluid Flow*, 7(4):283–290, 1986.

[23] Charles L Merkle. Computational modelling of the dynamics of sheet cavitation. In *Proc. of the 3rd Int. Symp. on Cavitation, Grenoble, France, 1998*, 1998.

[24] Vijayanand S Moholkar and Aniruddha B Pandit. Bubble behavior in hydrodynamic cavitation: effect of turbulence. *AIChE Journal*, 43(6):1641–1648, 1997.

[25] KA Mørch. On the collapse of cavity clusters in flow cavitation. In *Cavitation and Inhomogeneities in Underwater Acoustics*, pages 95–100. Springer, 1980.

[26] KA Morch. Cavity cluster dynamics and cavitation erosion. In *Cavitation Polyphase Flow Forum 1981*, pages 1–10, 1981.

[27] F Moukalled, L Mangani, M Darwish, et al. The finite volume method in computational fluid dynamics. 2016.

[28] F Örley, T Trummler, S Hickel, MS Mihatsch, SJ Schmidt, and NA Adams. Large-eddy simulation of cavitating nozzle flow and primary jet break-up. *Physics of Fluids*, 27(8):086101, 2015.

[29] Jean-Luc Reboud, Benoit Stutz, and Olivier Coutier. Two phase flow structure of cavitation: experiment and modeling of unsteady effects. In *3rd International Symposium on Cavitation CAV1998, Grenoble, France*, volume 26, 1998.

[30] Guilherme F Rosetti, Guilherme Vaz, and André LC Fujarra. Urans calculations for smooth circular cylinder flow in a wide range of reynolds numbers: solution verification and validation. *Journal of Fluids Engineering*, 134(12):121103, 2012.

[31] Sören Schenke and Tom JC van Terwisga. Simulating compressibility in cavitating flows with an incompressible mass transfer flow solver. In *Proceedings of the 5th International Symposium on Marine Propulsors, Finland*, 2017.

[32] Günter H Schnerr and Jürgen Sauer. Physical and numerical modeling of unsteady cavitation dynamics. In *Fourth international conference on multiphase flow, New Orleans, USA*, volume 1, 2001.

[33] Inanc Senocak and Wei Shyy. A pressure-based method for turbulent cavitating flow computations. *Journal of Computational Physics*, 176(2):363–383, 2002.

[34] Inanc Senocak and Wei Shyy. Interfacial dynamics-based modelling of turbulent cavitating flows, part-1: Model development and steady-state computations. *International journal for numerical methods in fluids*, 44(9):975–995, 2004.

[35] Ismail Hakki Sezal. *compressible dynamics of cavitating 3-D multi-phase flows*. PhD thesis, Technische Universität München, 2009.

[36] Ashok K Singhal, Mahesh M Athavale, Huiying Li, and Yu Jiang. Mathematical basis and validation of the full cavitation model. *Journal of fluids engineering*, 124(3):617–624, 2002.

[37] C Stanley, T Barber, and G Rosengarten. Re-entrant jet mechanism for periodic cavitation shedding in a cylindrical orifice. *International Journal of Heat and Fluid Flow*, 50:169–176, 2014.

[38] Petar Tomov, Kilian Croci, Sofiane Khelladi, Florent Ravelet, Amélie Danlos, Farid Bakir, and Christophe Sarraf. Experimental and numerical investigation of two physical mechanisms influencing the cloud cavitation shedding dynamics. 2016.

[39] L Van Wijngaarden. On the collective collapse of a large number of gas bubbles in water. In *Applied Mechanics*, pages 854–861. Springer, 1966.

[40] Ben-Long Wang and Li Ya-yun, Liu. On the numerical simulations of vortical cavitating flows around various hydrofoils. *Journal of Hydrodynamics, Ser. B*, 29(6):926–938, 2017.

[41] Frank M White. Fluid mechanics, mcgraw-hill series in mechanical engineering, 1998.

[42] Sergey Yakubov, Thierry Maquil, and Thomas Rung. Experience using pressure-based cfd methods for euler–euler simulations of cavitating flows. *Computers & Fluids*, 111:91–104, 2015.

[43] H Zhang, B Han, XG Yu, and DY Ju. Numerical and experimental studies of cavitation behavior in water-jet cavitation peening processing. *Shock and Vibration*, 20(5):895–905, 2013.

[44] Philip J Zwart, Andrew G Gerber, and Thabet Belamri. A two-phase flow model for predicting cavitation dynamics. In *Fifth international conference on multiphase flow, Yokohama, Japan*, volume 152, 2004.